Anharmonic contributions to *ab initio* computed thermodynamic material properties

Dissertation
zur Erlangung des akademischen Grades
Doktor der Naturwissenschaften (Dr. rer. nat.)
vorgelegt dem
Department Physik der Fakultät für Naturwissenschaften
an der Universität Paderborn

Albert Glensk

Promotionskommission
Vorsitzender   Prof. Dr. Dirk Reuter
Gutachter   Prof. Dr. rer. nat. Wolf Gero Schmidt
Gutachter   Prof. Dr. rer. nat. Jörg Neugebauer
Gutachter   Prof. Dr. Michael Finnis

Tag der Einreichung: 19. Oktober, 2015

Acknowledgments

Abstract

Computer simulations are the heart of modern materials design. The state-of-the-art methodology is density functional theory (DFT) which takes into account the quantum mechanical nature of the interacting atoms and electrons to high accuracy. DFT however has been originally designed to predict only ground-state properties at $T=0\,\mathrm{K}$ whereas finite temperature effects — indispensable for practical materials design — are generally neglected due to significant numerical requirements. The key challenge for the prediction of novel materials by DFT is therefore its extension to finite temperatures.

While for nonmagnetic systems electronic finite temperature excitations are nowadays considered standard in DFT, the accurate and full treatment of lattice vibrations turns out to be a daunting task. The usual approach is to describe the vibrating atoms in harmonic approximation while anharmonic contributions due to phonon-phonon interactions have been calculated so far only for a few selected test systems on a fully *ab initio* level [1, 2]. The corresponding investigations did however show that the full vibrational spectrum — including anharmonicity — is key for a quantitatively correct description of material properties at elevated temperatures: Phase stabilities and phase transition temperatures for instance can easily be changed by anharmonic contributions by several hundreds of Kelvin [3]. Thermal expansions, heat capacities, scattering of neutrons and the thermal conductivity of materials are all strongly influenced or even fully controlled by anharmonic phonon-phonon interactions [1, 2, 4]. A fully *ab initio* guided materials design at elevated temperatures is currently hindered by two main facts: (i) routine calculations of anharmonic phonon-phonon interactions are out of reach for first principles methods due to huge computational requirements and (ii) the magnitude of anharmonic contributions at elevated temperatures is generally unknown and therefore usually omitted.

In this work I have addressed both points: (a) To assess the physical relevance of phonon-phonon interactions, full *ab initio* calculations including anharmonic contributions have been carried out for a variety of material systems. In particular a wide range study on unary bulk elements was performed and consequences of phonon-phonon interactions have been also assessed for binary and defect systems. (b) To address the challenge of the significant computational demands of anharmonic calculations the novel and highly efficient *Local Anharmonic* (LA) approximation has been developed which vastly accelerates the calculation of anharmonic contributions by about two orders of magnitude without any loss of accuracy. It is found that anharmonic contributions for bulk systems are of the same order as the generally considered quasiharmonic contributions and cannot be neglected for thermodynamic assessments. Based on the performed calculations for defects, the *Local Grüneisen theory* (LGT) has been developed which is for the first time able to reconcile all experimentally measured vacancy formation energies of Al and Cu with fully *ab initio* computed results over the whole temperature range up to the melting point. Applying the LGT to experimentally measured vacancy data it is shown that vacancy formation enthalpies — as compiled, e.g., in the Landoldt-Börnstein series — must be revisited. Consequences of LGT for novel surface corrected xc functionals such as AM05 are discussed.

Contents

Chapter 1

Introduction: *Ab initio* thermodynamics

New materials can be described and even predicted based on known concepts of solid state theory. By doing so it often turns out that limitations in our understanding of the basic physical mechanisms are in the end the limiting factor which determine the performance of devices and their sustainability.

The modern route to the design of advanced materials is ultimately based on quantum theory. The gyromagnetic ratio of the electron is one example for the outstanding accuracy of quantum theory which is in agreement with the experimental measurement to within the experimental accuracy, 10 decimal places [5]. Beyond the high accuracy, a further aspect turns out to be equally important for practical applications: Quantum theory is parameter free and does not depend on experimental input. It is based on fundamental physical constants as the nuclei and electron mass, the electric constant, Planck's constant, the speed of light etc. Techniques which are only based on fundamental physical constants are often termed *ab initio* — Latin for 'from the beginning' — or 'first principles' methods. These kind of approaches can be applied also in situations which are unaccessible to experiment or where actual measurements would be too expensive or time consuming. Physical questions as well as chemical and biological phenomena alike have been correctly described by quantum theory and there is a justified belief that a deeper understanding of material properties can be gained by continuing to apply these methods.

Currently, a world-wide trend is observed toward smaller devices and resolving materials phenomena on the atomic or even electronic scale. Many of the used concepts to describe structural materials originate however from macroscopic observations and can consequently be refined by the inclusion of atomistic considerations. The access to highly accurate quantum mechanical ab initio methods provides a major opportunity to investigate the underlying assumptions of established theories. Refining those increases their predictive power and is a prerequisite for the creation of advanced materials and devices. One of the well established first principles methods which was derived in the last decades and which is the current work-horse for practical materials predictions is density functional theory (DFT). Current implementations can treat hundreds of atoms and allow to compare theoretical first principles predictions of bulk and defect properties directly to macroscopic experimental measurements.

A practical question that arises when considering highly accurate theoretical calculations is which experimental measurements can serve as a sensitive benchmark for *ab initio* predictions. Most of the experimental data on semiconductor band gaps for instance are afflicted with an uncertainty of a few tenth of an eV. Thermodynamic equilibrium properties on the other hand

have been evaluated experimentally to a higher accuracy. Changes in the free energy of a few meV are known to effect phase transition temperatures by several hundred Kelvin. One prominent example being the fcc to bcc phase transition in bulk iron which is the result of an ~ 1 meV/atom free energy difference between the corresponding phases at temperatures above 1200 Kelvin [3]. The Calphad database [6] collects free energies of all unary elements in the periodic table and changing those only by a few meV would result in phase diagrams which do not agree with experimental observations. Free energies — and their derived quantities as volume expansion and heat capacities — are therefore one of the most sensitive experimental measures for assessing the accuracy of quantum mechanically derived first principles calculations.

Experimental measurements of defect formation energies turn out to be even more sensitive. At elevated temperatures they can nowadays be resolved to better than 10 meV/defect using accurate experimental techniques. In order to study point defects theoretically, about 100 atoms are necessary to converge the considered defect formation energy. This corresponds to an accuracy of 0.1 meV per atom in a typical supercell containing 100 atoms. It has been found that — for bulk free energies and in particular for defect formation energies — this level of accuracy cannot be met by semi empirical methods as the embedded atom model (EAM) [2, 3, 7, 8] and the current parameterizations fail at elevated temperatures to yield satisfactory thermodynamic predictions. The question is therefore whether and to which extent parameter free DFT methods can be used to obtain accurate and quantitatively correct predictions in particular at realistic temperatures which are a challenge for DFT implementations which were originally developed for $T=0\,\mathrm{K}$.

Originally, DFT has been designed as a ground state theory and most first principles calculations are still performed solely at $T=0\,\mathrm{K}$. In practice however, materials operate at elevated or even high temperatures. Calphad [6] free energies are parametrized starting at room temperature and can therefore not be compared directly to $T=0\,\mathrm{K}$ *ab initio* calculations. Vacancy formation energies, which are most sensitive to free energy changes, are accessible to experimental measurements only above $\approx 60\%$ of the elements melting temperature. The mentioned examples pose a major problem for parameter free calculations due to the apparent temperature gap between finite temperature experimental measurements and $T=0\,\mathrm{K}$ first principles evaluations: A meaningful comparison to experiment is only possible once all relevant finite temperature effects are taken accurately into account. While the theoretical treatment of electronic excitations is considered standard for *ab initio* DFT methods, atomic vibrations are treated usually in an approximative manner and the full vibrational spectrum, which is decisive at elevated temperatures, is not rigorously captured by current implementations.

The state-of-the-art first principles approach for the treatment of atomic vibrations in solids is the quasiharmonic approximation. The full vibrational spectrum beyond quasiharmonic contributions — namely anharmonic contributions which are governed by phonon-phonon interactions — has been considered only for a few selected systems due to prohibitive computational demands. Although some empirical estimates for anharmonic contributions exist, a rigorous and fully *ab initio* study for a wide range of materials has not been performed. Aluminum is one of the example elements where the full spectrum of atomic vibrations has been calculated by first principles including phonon-phonon interactions [2, 9]. For this system, a decisive improvement of the thermodynamic properties as e.g. the heat capacity and volume expansion has been found with respect to experimental measurements [2] by including anharmonic contributions. It was also shown that the entropy of vacancy formation in Al is significantly affected by anharmonic effects. It is therefore crucial to ask if these findings were an exception or whether the usually neglected anharmonic effects play an important role for a wide range of materials. The main goal of this thesis is to evaluate the relevance of anharmonic effects for various material systems on a fully *ab initio* basis.

The usual first principles approach to assess finite temperature material properties is to include the computationally feasible quasiharmonic and electronic contributions while anharmonic contributions are generally neglected. The main reason for this is the numerical effort for the calculation of phonon-phonon interactions. Recent theoretical approaches aiming at tackling the computation of anharmonic contributions will be examined as part of this thesis. The development of strategies which promote the calculation of anharmonic contributions to a routine task is one of the critical challenges for *ab initio* methods and one of the main concerns of this study. To gain a physically intuitive understanding of anharmonic effects corresponding calculations will be performed for bulk and defect systems.

This thesis is organized as follows: Chap. 2 introduces the state-of-the-art theoretical concepts necessary for the calculation of thermodynamic material properties and in particular atomic vibrations. Chap. 3 focuses on the developed methods during this PhD work: Sec. 3.1 presents the *local anharmonic* (LA) approximation which extends the well established quasiharmonic approximation and allows to obtain fully converged anharmonic free energies from a few $T=0\,\mathrm{K}$ calculations. The second part of the methodology chapter, Sec. 3.2, derives a further novel approach, the *Local Grüneisen theory* (LGT) which goes beyond the usually applied linear Arrhenius ansatz for defect formation by considering anharmonic effects.

Selected parts of the results obtained during this PhD work are presented in Chap. 4 which investigates the consequences of *ab initio* derived anharmonic contribution on selected material systems. Sec. 4.1 explores anharmonicity for a wide range of fcc elements and investigates corresponding contributions to thermodynamic material properties. Sec. 4.2 goes beyond standard DFT functionals and includes non-local many body effects for three selected systems up to the melting temperature. Sec. 4.3 probes anharmonic effects in a binary alloy system, Mg_2Si, and evaluates the empirically derived Neumann-Kopp rule for the prediction of multinary heat capacity data. Sec. 4.4 studies in detail the mono- and divacancy formation energy in Al and Cu and compares the effects of the full vibrational spectrum — including anharmonic contributions — to the current experimental picture on defect formation.

Chapter 2

Theory

The main motivation for this thesis is an efficient first principles determination of material properties at finite temperatures. The key quantity which governs all thermodynamic properties of solids at $T > 0\text{K}$, and which therefore is central in this work, is the Helmholtz free energy $F(V,T)$ as a function of the external volume V and temperature T

$$F(V,T) = U(V,T) - TS(V,T). \tag{2.1}$$

Here, $U(V,T)$ is the internal energy and $S(V,T)$ the entropy of the system. Performing a Legendre transformation, the Gibbs free energy $G(P,T)$ as a function of pressure and temperature can be obtained from $F(V,T)$. Practical approaches for the calculation of the internal energy $U(V,T)$ and the entropy $S(V,T)$ on a fully *ab initio* level will be covered in the following sections. Since all material properties in equilibrium can be directly derived from $G(P,T)$ or $F(V,T)$, these thermodynamic potentials are of fundamental and practical importance for our understanding of matter. The entropy $S(V,T)$ as well as the pressure $P(V,T)$ can be directly obtained from the free energy by

$$S(V,T) = -\left(\frac{\partial F(V,T)}{\partial T}\right)_V \quad \text{and} \quad P(V,T) = -\left(\frac{\partial F(V,T)}{\partial V}\right)_T, \tag{2.2}$$

where the subscript, V and T, indicate that the corresponding derivative has been performed at fixed volume or temperature, respectively. It is important to realize that all thermodynamic experimental observables are directly related to simple derivatives of $G(P,T)$ or $F(V,T)$. Therefore, physical properties as the volume expansion, the adiabatic and isothermal bulk modulus and heat capacity, the isothermal compressibility of the system are all directly accessible once the thermodynamic potentials are known. The isobaric and isochoric heat capacities, $C_P(T)$ and $C_V(T)$, for example become

$$C_P(T) = T\left(\frac{\partial S(V,T)}{\partial T}\right)_P = -T\left(\frac{\partial^2 F(V,T)}{\partial T^2}\right)_{V,P}, \tag{2.3}$$

$$C_V(T) = T\left(\frac{\partial S(V,T)}{\partial T}\right)_V = \left(\frac{\partial U(V,T)}{\partial T}\right)_V \tag{2.4}$$

and the adiabatic bulk modulus $B_S(T)$

$$B_S(T) = -V\left(\frac{\partial P(V,T)}{\partial V}\right)_S = V\left(\frac{\partial^2 F(V,T)}{\partial V^2}\right)_{T,S}. \tag{2.5}$$

Ultimately, the free energy $F(V,T)$ defined in Eq.2.1 needs to be determined for the system of interacting particles — for the purpose of this thesis these are the atoms and electrons — to gain thermodynamic properties of materials.

The quantity which accordingly enters the constituting $U(V,T)$ and $S(V,T)$ terms is the total energy of the system, E, at a particular temperature and volume. The computation of the total energy of a solid can nowadays be performed by first principles methods to high accuracy. Corresponding theoretical details will be presented in Sec. 2.2. While, as will be shown in the following section, thermodynamic averages for $U(V,T)$ can straight forwardly be obtained by first principles at arbitrary temperatures and volumes, the calculation of entropic and related quantities poses a significant challenge. The problems which arise with the sampling of entropic quantities usually result in either neglecting finite temperature effects or in treating those approximatively. Overcoming these limitations is the main aim of this work.

The main constituents entering the total entropy of a system containing electrons and nuclei at a fixed volume and temperature are

$$S(V,T) = S^{\text{total}} = S^{\text{conf}} + S^{\text{vib}} + S^{\text{el}} + S^{\text{mag}}, \tag{2.6}$$

were S^{conf} denotes the configurational entropy due to all possible arrangements of different atomic species in a solid, S^{vib} is the entropy due to atomic vibrations and S^{el} and S^{mag} the entropy due to electronic and magnetic contributions. Further terms not included in Eq. 2.6 are coupling terms between the different entropic contribution as, e.g., electron-phonon coupling or contributions due to vacancies. While the latter is investigated as part of this work, non magnetic coupling terms for the here investigated systems have been previously shown to be negligible [10]. This thesis will deal exclusively with unary elements which contain only a single atomic species and with a (also nonmagnetic) binary compound at fixed stoichiometry. For these systems, S^{conf} and S^{mag} are zero and need therefore not to be considered. The calculation of S^{el} is standard and was performed for all the calculations presented in this thesis following Ref. [11]. To obtain S^{vib} from first principles was until recently only practical in an approximative fashion. Only very few cases are known where the full excitation spectrum of atomic vibrations has been calculated over the whole temperature range [2, 9] on an *ab initio* level of accuracy. The reason for the difficulties as well as methods to overcome those are the subject of Sec. 3.1 of this thesis.

2.1 Entropic quantities and their relation to ensemble averages from molecular dynamics

A fundamental challenge in numerical simulations of solids is the calculation of the entropy of the system $S(V,T)$ and related quantities such as the Helmholtz and the Gibbs free energy, $F(V,T)$ and $G(P,T)$. Statistical mechanics considers any system to be distributed across an ensemble of N (micro) states. Each state has a distinct energy E_i which is associated with a probability of occurrence p_i. The internal energy U is the mean value of the system's total energy, i.e., the sum of all state energies (also called microstates), each weighted by their probability of occurrence p_i:

$$U \equiv \langle E \rangle = \sum_{i=1}^{N} p_i E_i. \tag{2.7}$$

The probability distribution for the microstates is controlled by the considered statistical ensemble (micro-canonical, canonical, grand-canonical, etc.). The exact details of the calculation of E_i for a

particular atomic configuration and electronic state are shown in Sec. 2.2. The probability in the canonical ensemble p_i that the system occupies a state i is given by

$$p_i = \frac{1}{Z} e^{-\beta E_i}. \tag{2.8}$$

where $Z(V,T) = Z$ is the canonical partition function defined by

$$Z = \sum_{i=1}^{N} e^{-\beta E_i}, \tag{2.9}$$

with $\beta = (k_{\mathrm{B}} T)^{-1}$ and k_{B} the Boltzmann constant. According to statistical physics, for a system in thermodynamic equilibrium, the Helmholtz free energy F is also directly related to the partition function Z by

$$F(V,T) = -k_{\mathrm{B}} T \ln Z(V,T) = U(V,T) - TS(V,T). \tag{2.10}$$

The entropy of the system is a measure of accessible states and is defined by

$$S(V,T) = -k_{\mathrm{B}} \sum_{i=1}^{N} p_i \ln p_i = k_{\mathrm{B}} \ln Z(V,T) + \frac{U(V,T)}{T}, \tag{2.11}$$

and therefore depends, as F and U, on the canonical partition function $Z(V,T)$. The internal energy is defined as

$$U(V,T) = k_{\mathrm{B}} T^2 \frac{\partial \ln Z(V,T)}{\partial T} = -\frac{\partial \ln Z(V,T)}{\partial \beta}. \tag{2.12}$$

When a numerical molecular dynamics (MD) run is performed, the phase space of available states is not randomly sampled but — by construction of the MD — according to the corresponding phase space probability p_i. Since the weighting of total energies E_i is implicitly performed, the internal energy U can in principle — and also in practice — be calculated by applying MD. Corresponding thermodynamic averages,

$$U \equiv \langle E \rangle = \frac{1}{N_{\mathrm{MD}}} \sum_{i=1}^{N_{\mathrm{MD}}} E_i^{\mathrm{MD}}, \tag{2.13}$$

can be converged for manageable computational cost to a reasonable accuracy where N_{MD} is the number of performed MD steps and E_i^{MD} the total energy for a single MD configuration. In contrast, performing a similar averaging for the entropy (Eq. 2.11) is computationally not feasible [12] due to the weighting of p_i with the partition function. It is the exponential in Eq. 2.8 which prohibits a practical assessment of the entropy by means of a direct application of MD. The major challenge is the large number of configurations which are necessary to converge the thermodynamic ensemble averages. Simple estimates show that *brute force* sampling approaches require on the order of $10^6 - 10^7$ *ab initio* computed configurations to get the desired accuracy [2] to correctly sample the partition function. An accurate sampling of entropic quantities by numerical methods is therefore a challenging task and state-of-the-art approximate and exact methods to tackle this problem will be presented in the theoretical part of this thesis.

The following part of this chapter is structured as follows: Sec. 2.2 formulates the many-body problem which yields the total energy E for the system of interacting electrons and nuclei. Density functional theory (DFT) is introduced as a method which makes the solution of the many-body

problem numerically feasible. Since, as has been shown above, entropic quantities such as the *free energy* can not be sampled directly by means of MD, Sec. 2.3 introduces approximate methods for the entropy of lattice vibrations. In particular, the Debye, Grüneisen and the harmonic and quasiharmonic approximations are covered. Sec. 2.4.2 introduces the concept of thermodynamic integration which makes it possible to calculate free energies and entropies numerically exactly. The numerical results obtained by thermodynamic integration were an integral part for this PhD work and the basis for the developed methods.

2.2 From the many-body problem to density functional theory

The many-body problem of interacting nuclei and electrons is governed by the solution of the — for the purpose of this thesis time *independent* — Schrödinger equation

$$H_{N,e}\Psi_{N,e}(\mathbf{R}_1, \mathbf{R}_2, \ldots, \mathbf{R}_N, \mathbf{r}_1, \mathbf{r}_2, \ldots, \mathbf{r}_n) = E_{N,e}\Psi_{N,e}(\mathbf{R}_1, \mathbf{R}_2, \ldots, \mathbf{R}_N, \mathbf{r}_1, \mathbf{r}_2, \ldots, \mathbf{r}_n) \quad (2.14)$$

where $E_{N,e}$ is the total energy of the system of interacting particles, $\mathbf{R}_i$ are the coordinates of the N nuclei and $\mathbf{r}_i$ those of the n electrons. $\Psi_{N,e}$ is the many-body wave function and the Hamiltonian $H_{N,e}$ is given by the following equation:

$$H_{N,e} = -\sum_{I}^{N} \frac{\hbar^2}{2M_I}\nabla_I^2 - \sum_{i}^{n} \frac{\hbar^2}{2m_e}\nabla_i^2 + \frac{1}{2}\sum_{i \neq j} \frac{e^2}{|\mathbf{r}_i - \mathbf{r}_j|} - \sum_{I,i} \frac{e^2 Z_I}{|\mathbf{R}_i - \mathbf{r}_i|} + \frac{1}{2}\sum_{I \neq J} \frac{e^2 Z_I Z_J}{|\mathbf{R}_I - \mathbf{R}_J|} \quad (2.15)$$

and can also be summarized

$$H_{N,e} = T_N + T_e + U_{e-e} + U_{N-e} + U_{N-N}. \quad (2.16)$$

Here, the first summand T_N represents the kinetic energy of the nuclei with their mass M_I. The second summand T_e describes the kinetic energy of the electrons with corresponding masses m_e. U_{e-e} is the Coulomb repulsion between the electrons and the last term U_{N-N} the repulsion potential between the nuclei. The remaining summand U_{N-e} describes the Coulomb attraction between electrons and nuclei.

Though the Schrödinger equation (Eq. 2.14) forms the foundation of quantum theory it can only be solved analytically exact for the hydrogen atom and for similar cases involving two particles. Already the hydrogen molecule H_2 can not be solved analytically and numerical approximations are indispensable. At the very heart of every numerical implementation of the many-body Schrödinger equation is therefore the question of how to approximate the interactions defined in Eq. 2.15 to get the best trade-off between accuracy and computational cost. Two of the well-established approximations, the Born-Oppenheimer approximation and DFT are introduced in the following.

2.2.1 Born-Oppenheimer approximation

The Born-Oppenheimer — or adiabatic — approximation [13] decouples the many-body Schrödinger equation (Eq. 2.14) in two independent equations, one for the electronic system and one for the nuclei. This is possible because the mass of the nucleus is much greater than the mass of an electron ($M_I \gg m_e$) although both experience a rather similar Coulomb force. It is therefore reasonable to assume that the electrons will react essentially instantaneously upon motion of the nuclei. Due to the fast electronic relaxation, the electronic system remains in the stationary ground state of the

Hamiltonian and can therefore be efficiently solved at *fixed* atomic positions. The nuclei in turn are governed by the (also external) electrostatic potential caused by all electrons of the considered system. An alternative argumentation which justifies the separation of the electronic and atomic degrees of freedom is that the frequency spectra of atomic vibrations do not overlap with the energies (frequencies) of the electronic system [14]. Energy can therefore not be transfered from 'slowly' moving/vibrating atomic system to the 'fast' electronic system which occupies higher frequencies.

In practice, the decoupling of the electronic system from the ionic system is performed by separation of the wave function

$$\Psi_{N,e}(\{\mathbf{R}_N\}\{\mathbf{r}_e\}) = \Psi_e(\{\mathbf{r}_e\})\Psi_N(\{\mathbf{R}_N\}), \tag{2.17}$$

by which the Schrödinger equation in Eq. 2.14 can be solved independently for the system of electrons

$$H_e\Psi_e(\{\mathbf{r}_e\}) = (T_e + U_{e-e} + U_{N-e})\Psi_e(\{\mathbf{r}_e\}) = E_e\Psi_e(\{\mathbf{r}_e\}) \tag{2.18}$$

and nuclei

$$H_N\Psi_N(\{\mathbf{R}_N\}) = (T_N + U_{N-N} + E_e^0)\Psi_N(\{\mathbf{R}_N\}) = E_{nuc}\Psi_N(\{\mathbf{R}_N\}). \tag{2.19}$$

The nuclei positions $\{\mathbf{R}_N\}$ enter the electronic Schrödinger equation in Eq. 2.18 as known parameters and have therefore been omitted in the nomenclature since they need not to be solved for. Since the atomic positions are *fixed*, the interactions between electrons and nuclei, U_{N-e}, enter the electronic Hamiltonian H_e only as a static *external* potential.

In the separated Schrödinger equation for the nuclei, Eq. 2.19, E_e^0 is the ground state potential due to the electrons which has to be solved by minimizing Eq. 2.18 and enters therefore also as an external potential which depends on the atomic positions $\{\mathbf{R}_N\}$. This means that a feedback is incorporated in both directions, from the electronic to the system of nuclei and vice versa. Solving the nuclear Schrödinger equation yields the total energy of the system $E_{nuc} = E_i$ which is used in the thermodynamic potentials (e.g. Eq. 2.13) for different atomic configurations i. The Hamiltonian for the nuclei, H_N, contains the Born-Oppenheimer surface E^{BO} which governs the motion of the atoms

$$E^{\mathrm{BO}} = U_{N-N} + E_e^0. \tag{2.20}$$

In summary, the adiabatic approximation reduces the many-body problem of atoms and electrons to two separated problems. The complexity of the numerically challenging electronic system is significantly reduced since the positions of the nuclei enter only as external parameter. Even with this drastic simplification, a numerical solution of the electronic many-body equation remains infeasible due to its unfavorable scaling [15]. The solution to this problem is tackled by density functional theory.

2.2.2　Density functional theory

Density functional theory (DFT) has evolved to one of the most popular and successful methods for the calculation of the electronic structure of matter. Instead of the full many-body wave function it uses the electron density as the key variable from which physically relevant observables are derived. Its main achievement is the — in principal exact — mapping of the difficult many-body problem onto that of a single electron moving in an effective potential, determined by the electron density. The derivation of practical DFT calculations is usually split in two main steps: In a first step the

density is introduced by the Hohenberg and Kohn theorems which however is still a many-body problem. The second step, formulated by the Kohn-Sham equation, maps this problem onto one of non-interacting particles.

The foundation of DFT is based on two main theorems which were formulated and proved by Hohenberg and Kohn [16]:

1) *First Theorem:* For system of interacting electrons in an external potential (e.g. due to the fixed nuclei, U_{N-e}^{ext}) there is one unique ground state electron charge density $n_0(\mathbf{r})$. The nondegenerate many-body wave function in its ground state, $\Psi_e^0(\{\mathbf{r}_e\})$, is therefore a unique function of the ground state electron density

$$\Psi_e^0(\mathbf{r}_1, \mathbf{r}_2, \ldots, \mathbf{r}_n) = \Psi_e^0(\{\mathbf{r}_e\}) = \Psi[n_0(\mathbf{r})]. \tag{2.21}$$

2) *Second Theorem:* A functional for the energy $E[n(\mathbf{r})]$ can be defined in terms of the density $n(\mathbf{r})$. The electron density that minimizes the total energy of the interacting electrons is the ground state density $n_0(\mathbf{r})$ and therefore

$$E[n_0(\mathbf{r})] \leq E[n(\mathbf{r})] \tag{2.22}$$

where $n(\mathbf{r})$ is an arbitrary electron density and $E[n_0(\mathbf{r})] = E_e^0$ the ground state energy of the electronic system which is necessary to solve Eq. 2.19.

The second Hohenberg and Kohn theorem is based on the Rayleigh-Ritz variational principle which yields a practical way of finding the ground state energy E_e^0 given a suitable expression for $E[n(\mathbf{r})]$ and an arbitrary trial wave function $\Psi_{\text{trial}} = \Psi[n(\mathbf{r})]$.

The Hohenberg and Kohn energy functional $E[n(\mathbf{r})]$ for the system of interacting electrons defines Eq. 2.18 in terms of the density

$$E[n(\mathbf{r})] = F[n(\mathbf{r})] + \int n(\mathbf{r}) U_{\text{ext}}(\mathbf{r}) dr \tag{2.23}$$

where $F[n(\mathbf{r})]$ is a universal functional which is independent of $U_{\text{ext}}(\mathbf{r})$ and contains the kinetic energy of interacting electrons $T[n(\mathbf{r})]$ and the Coulomb potential $U_{e-e}[n(\mathbf{r})]$ due to electron-electron interactions

$$F[n(\mathbf{r})] = T[n(\mathbf{r})] + U_{e-e}[n(\mathbf{r})]. \tag{2.24}$$

The many-body wave function $\Psi_e(\mathbf{r}_1, \mathbf{r}_2, \ldots, \mathbf{r}_n)$ — a function of 3N spatial coordinates where N is the number of electrons — is reduced by means of the Hohenberg and Kohn theorems to a function of 3 spatial coordinates — $\Psi[n(\mathbf{r})]$ — which defines the electronic density. This drastic reduction in the degrees of freedom significantly simplifies the wave function and makes a solution of the many-body interacting problem for the electrons numerically feasible. However, no explicit way has yet been provided for the computation of the electronic ground-state density or the Hohenberg and Kohn functional. Though DFT can be realized in several ways, the Kohn and Sham approach is until today the most popular and successful one [17] to solve this problem.

2.2.3 Kohn-Sham equations

Kohn-Sham [17] proposed in 1965 an ingenious way to map the *interacting* many-electron system (in a static external potential due to the nuclei) onto a system of *noninteracting* electrons moving in an effective potential due to the charge density of all the other electrons. In this way an electron does

not interact with other electrons of the system but only with the effective 'Kohn-Sham' potential. Solving the Kohn-Sham equation for the non-interacting electrons — which evolve within the Kohn-Sham potential $v_{\text{eff}}^{\text{KS}}(\mathbf{r})$ — results in an electron density for the noninteracting system which equals the electron density of the interacting system $n(\mathbf{r}) \equiv n^{\text{KS}}(\mathbf{r})$. In the following however only the non-interacting Kohn-Sham density will be used and we drop the subscript by applying the nomenclature $n_0(\mathbf{r}) = n_0^{\text{KS}}(\mathbf{r})$ and $n(\mathbf{r}) = n^{\text{KS}}(\mathbf{r})$. Assuming a system of noninteracting particles, the universal functional $F[n(\mathbf{r})]$ can be defined by

$$F[n(\mathbf{r})] = T_S[n(\mathbf{r})] + E_H[n(\mathbf{r})] + E_{\text{XC}}[n(\mathbf{r})] \tag{2.25}$$

where $T_S[n(\mathbf{r})]$ is the single particle kinetic energy (the subscript S is used since this can be represented by a Slater determinant) which is exactly known for a non-interacting electron gas

$$T_{\text{S}}[n(\mathbf{r})] = -\frac{1}{2} \sum_{i=1}^{N} \int \psi_i^*(\mathbf{r}) \nabla^2 \psi_i(\mathbf{r}) \, d\mathbf{r} \tag{2.26}$$

and where the single-particle states $\psi_i(r)$ define the Kohn-Sham charge density $n(\mathbf{r})$ in terms of a set of N non-interacting electrons

$$n(\mathbf{r}) = \sum_{i}^{N} |\psi_i(\mathbf{r})|^2 \tag{2.27}$$

which are often called the Kohn-Sham orbitals. The classical electrostatic Coulomb interaction $E_H[n(\mathbf{r})]$ — also known as the Hartree term — is defined by

$$E_H[n(\mathbf{r})] = \frac{1}{2} \int \int \frac{n(\mathbf{r})n(\mathbf{r'})}{|\mathbf{r} - \mathbf{r'}|} \, d\mathbf{r} \, d\mathbf{r'} \tag{2.28}$$

and $E_{\text{XC}}[n(\mathbf{r})]$ is a small correction term — the exchange-correlation energy. $E_{\text{XC}}[n(\mathbf{r})]$ contains

a) the difference $T_C[n(\mathbf{r})]$ between the exact and the non-interacting kinetic energy $T_C[n(\mathbf{r})] = T[n(\mathbf{r})] - T_S[n(\mathbf{r})]$. The subscript C indicates that this is the so called 'correlation term'.

b) the correction due to the difference between the exact and interacting electron-electron Coulomb repulsion and the classical Hartree term $E_{e-e}[n(\mathbf{r})] - E_H[n(\mathbf{r})]$.

$E_{\text{XC}}[n(\mathbf{r})]$ includes therefore all many-particle interactions and although not known exactly, sophisticated approximations have been developed. Well known examples are the Local local-density approximation (LDA) and the generalized-gradient approximation (GGA) [18–20]. Once an approximation has been defined for the exchange and correlation functional, the non-interacting system can easily be solved since all terms of $F[n(\mathbf{r})]$ are known analytically.

As stated above, the non-interacting Kohn-Sham potential $v_{\text{eff}}^{\text{KS}}(\mathbf{r})$ reduces the many-body problem of interacting particles to solving a one-electron Schrödinger-like equation which is given by

$$\left(-\frac{\hbar^2}{2m} \nabla^2 + v_{\text{eff}}^{\text{KS}}(\mathbf{r}) \right) \psi_i(\mathbf{r}) = \varepsilon_i \psi_i(\mathbf{r}). \tag{2.29}$$

The above definition is the Kohn-Sham equation with Kohn-Sham orbitals $\psi_i(\mathbf{r})$ which are used to construct the electron density defined in Eq. 2.27. The Kohn-Sham potential is defined by

$$v_{\text{eff}}^{\text{KS}}(\mathbf{r}) = v_{\text{ext}}(\mathbf{r}) + v_{\text{H}}(\mathbf{r}) + v_{\text{XC}}(\mathbf{r}) = v_{\text{ext}}(\mathbf{r}) + e^2 \int \frac{n(\mathbf{r'})}{|\mathbf{r} - \mathbf{r'}|} d\mathbf{r'} + \frac{\delta E_{\text{xc}}[n]}{\delta n(\mathbf{r})}, \tag{2.30}$$

where $v_H(r)$ and $v_{XC}(r)$ are derivatives of $E_H[n(\mathbf{r})]$ and $E_{XC}[n(\mathbf{r})]$ with respect to the density $n(\mathbf{r})$ respectively.

Since a wave function and the corresponding density are necessary to evaluate the Kohn-Sham equation 2.29, an iterative way has to be found in order to find the true ground state density $n_0(\mathbf{r})$. This is done by choosing an initial trial density $n_{in}(\mathbf{r})$ and calculating $v_H(r)$ and $v_{XC}(r)$ to form the effective Kohn-Sham potential $v_{eff}^{KS}(\mathbf{r})$. In the next step the Kohn-Sham equation Eq. 2.29 is solved using the initial $v_{eff}^{KS}(\mathbf{r})$ to form a new density $n_{out}(\mathbf{r})$. Given that the predefined energy convergence criterion is not reached — the total energy difference between $n_{in}(\mathbf{r})$ and $n_{out}(\mathbf{r})$ — both densities are mixed to form a new density which is used for the next iterative cycle. This iterative procedure is repeated until self consistency is reached which yields the ground state electron density $n_0(\mathbf{r})$.

2.3 Approximate theories of lattice vibrations

2.3.1 Independent harmonic oscillators — The Einstein crystal

The first application of quantum theory to the motion of atoms in a solid was performed by Einstein in 1906 when he modeled the atoms of a carbon crystal as perfect harmonic oscillators, the famous Einstein solid [21]. In his model, Einstein assumed that all carbon atoms were oscillating independently and with the same frequency ω_0. The atoms in the crystal were not connected by springs with each other but rather, every atom was bound to its equilibrium position with a spring. The occurrence of a single frequency in the system is a direct consequence of the missing interaction between the atoms. No standing waves can form with the corresponding *spectrum* of frequencies which are found for real crystals. The Einstein solid is therefore equal to a sum of simple harmonic oscillators.

The discrete energy levels of a one dimensional quantum harmonic oscillator (or phonon energies) are given by

$$E_n = \hbar\omega_0 \left(\frac{1}{2} + n\right), \qquad n = 0, 1, 2, 3, \ldots, \infty \tag{2.31}$$

where $\omega_0 = \sqrt{\frac{\mu_0}{m}}$ is the eigenfrequency of the atom/oscillator and μ_0 and m are the spring constant and mass of the atom respectively. The spring constant μ can easily be determined by e.g., first principles by performing a small displacement Δx and calculating the force on the atom F which are related by $F = \mu\,\Delta x$. The general definition of the partition function in Eq. 2.9 can be used with the quantized energy levels of the one dimensional harmonic oscillator, Eq. 2.31, to determine the temperature dependent partition function of the quantum mechanical (qm) harmonic oscillator

$$Z_{qm}(T) = \sum_{n=0}^{\infty} e^{-\beta E_n} = \sum_{n=0}^{\infty} e^{-\beta\hbar\omega_0\left(n+\frac{1}{2}\right)} = e^{-\beta\hbar\omega_0/2}\left(1 - e^{-\beta\hbar\omega_0}\right)^{-1}, \tag{2.32}$$

where the following geometric series has been used

$$\sum_{n=0}^{\infty} x^n = \frac{1}{1-x}. \tag{2.33}$$

We use the derived $Z_{qm}(T)$ and Eq. 2.10 to define the temperature dependent Helmholtz free energy

of a single quantum harmonic oscillator

$$
\begin{aligned}
F_{\mathrm{qm}}(T) &= -k_{\mathrm{B}}T \ln\left[Z_{\mathrm{qm}}(T)\right] \\
&= -k_{\mathrm{B}}T \ln\left[\mathrm{e}^{-\beta\hbar\omega_0/2}\left(1-\mathrm{e}^{-\beta\hbar\omega_0}\right)^{-1}\right] \\
&= \frac{\hbar\omega_0}{2} + k_{\mathrm{B}}T \ln\left[1-\mathrm{e}^{-\beta\hbar\omega_0}\right],
\end{aligned}
\tag{2.34}
$$

where the positive term $\hbar\omega_0/2$ is the quantum zero point energy which is due to Heisenberg's uncertainty principle and increases the classically derived ground state energy E_0 by an order of about 30 meV per atom at $T{=}0\,\mathrm{K}$. At a constant volume V all thermodynamic quantities can be derived from the free energy $F_{\mathrm{qm}}(T)$. The internal energy e.g. of the quantum mechanical oscillator is defined in by Eq. 2.10 and yields

$$
U_{\mathrm{qm}}(T) = F_{\mathrm{qm}}(T) + TS_{\mathrm{qm}}(T) = F_{\mathrm{qm}}(T) - T\left(\frac{\partial F_{\mathrm{qm}}(T)}{\partial T}\right) = \hbar\omega_0\left(\frac{1}{2} + \frac{1}{\mathrm{e}^{\beta\hbar\omega_0} - 1}\right) \tag{2.35}
$$

where the entropy has been substituted from Eq. 2.2. The agreement of Eqs. 2.31 and 2.35 is apparent since $U \equiv \langle E\rangle$ and

$$
n = \langle n_{\mathrm{BE}}(T)\rangle = \frac{1}{\mathrm{e}^{\beta\hbar\omega_0} - 1} \tag{2.36}
$$

is identified as the Bose-Einstein distribution function $\langle n(T)\rangle$ which is also called *occupation factor*. Other thermodynamic quantities can be directly derived from the free energy by the definitions in Sec. 2.1. The isochoric heat capacity, e.g., is given by

$$
C_V(T) = \left(\frac{\partial U(T)}{\partial T}\right) = \frac{\hbar^2\omega^2 \operatorname{csch}(\frac{\omega\hbar}{2k_{\mathrm{B}}T})^2}{4k_{\mathrm{B}}T^2} \tag{2.37}
$$

with $\operatorname{csch}(z)$ being the hyperbolic cosecant of z which satisfies $\operatorname{csch}(z) = 1/\sinh(z)$ with $\sinh(z)$ the hyperbolic sine of z.

For a single atom vibrating in three dimensions — Eq. 2.34 corresponds to a one dimensional quantum harmonic oscillator — the free energy can simply be multiplied by three since the harmonic vibrations of atoms are independent for the three spatial coordinates. We define therefore the free energy of a quantum mechanical oscillator in three dimensions — an atom in an Einstein solid — by

$$
F_{\mathrm{qm}}^{\mathrm{atom}}(T) = 3\frac{\hbar\omega_0}{2} + 3k_{\mathrm{B}}T \ln\left[1-\mathrm{e}^{-\beta\hbar\omega_0}\right]. \tag{2.38}
$$

What happens however if all the N atoms in the considered system are not vibrating *independently* but are assumed to be *coupled* by harmonic springs (and are therefore also termed coupled harmonic oscillators)? It can easily be shown [22] that performing a Fourier decomposition on a harmonic Hamiltonian it is possible to fully *decouple* the set of N coupled atoms into a set of N *uncoupled* oscillators (phonon's) which have to be summed over all plane waves in the system of wave vector $\mathbf{k}$. For instance, considering a 1D atomic chain with length L and atomic distances a, only discrete k are allowed of $k = 2\pi/L, 4\pi/L, ...$ which are scalars for the simple 1D case. The number of possible wave vectors is L/a due to the periodic boundary conditions and is therefore equal to the number of atoms N. Summing over all wave vectors, the vibrational free energy $F_{\mathrm{qm}}(T)$ in

Eq. 2.34 is generally defined by

$$F_{\text{qm}}^{\text{vib}}(T) = \frac{1}{N} \sum_{\mathbf{k}}^{3N} \left[\frac{\hbar\omega_{\mathbf{k}}}{2} + k_{\text{B}}T \ln \left[1 - e^{-\beta\hbar\omega_{\mathbf{k}}} \right] \right], \tag{2.39}$$

where the prefactor $1/N$ normalizes the free energy for a single atom.

Let us now compare the differences between a single quantum harmonic oscillator in Eq. 2.38 (Einstein solid) and a classical harmonic oscillator for which the (classical) Hamiltonian is defined by

$$H = \frac{p^2}{2m} + \frac{\mu_0 x^2}{2} = \frac{p^2}{2m} + \frac{m\omega_0^2 x^2}{2} \tag{2.40}$$

where μ_0, m and $\omega_0 = \sqrt{\frac{\mu_0}{m}}$ are the spring constant, the mass and the corresponding eigenfrequency of the atom/oscillator respectively. The classical partition function $Z_{\text{cl}}(T)$ is derived from the general thermodynamic relation

$$
\begin{aligned}
Z_{\text{cl}}(T) &= \frac{1}{h} \iint_{-\infty}^{\infty} e^{-\beta H} \, dp \, dx \\
&= \frac{1}{h} \int_{-\infty}^{\infty} dp \, e^{-\beta \frac{p^2}{2m}} \int_{-\infty}^{\infty} dx \, e^{-\beta \frac{m\omega_0^2 x^2}{2}} \\
&= \frac{1}{h} \sqrt{\frac{\pi}{-\beta/(2m)}} \sqrt{\frac{\pi}{-\beta \frac{m\omega_0^2}{2}}} \\
&= \frac{1}{\beta\hbar\omega_0},
\end{aligned}
\tag{2.41}
$$

where the reduced Planck constant $\hbar = \frac{h}{2\pi}$ has been used (also known as the Dirac constant). Now we can obtain the classical definition for the free energy of a one dimensional harmonic oscillator at fixed volume due to Eq. 2.10

$$F_{\text{cl}}(T) = -k_{\text{B}}T \ln Z_{\text{cl}}(T) = -k_{\text{B}}T \ln \left[\frac{k_{\text{B}}T}{\hbar\omega_0} \right] = k_{\text{B}}T \ln \left[\frac{\hbar\omega_0}{k_{\text{B}}T} \right]. \tag{2.42}$$

The same argument as before can be used to define the classical oscillator free energy having three independent degrees of freedom corresponding to a (real) vibrating atom in a crystal with

$$F_{\text{cl}}^{\text{atom}}(T) = 3k_{\text{B}}T \ln \left[\frac{\hbar\omega_0}{k_{\text{B}}T} \right]. \tag{2.43}$$

Accordingly, the classical entropy is derived from Eq. 2.2 by

$$S_{\text{cl}}^{\text{atom}}(T) = -\left(\frac{\partial F_{\text{cl}}^{\text{atom}}(T)}{\partial T} \right) = 3k_{\text{B}} + k_{\text{B}} \ln \left[\frac{k_{\text{B}}T}{\hbar\omega_0} \right] = 3k_{\text{B}} - k_{\text{B}} \ln \left[\frac{\hbar\omega_0}{k_{\text{B}}T} \right]. \tag{2.44}$$

Having derived the free energy of the classical and quantum system, all thermodynamic material properties — for a single (fixed) volume — can be calculated by applying the corresponding thermodynamic derivatives defined in Sec. 2. Assuming an average frequency ω_0 is obtained from DFT for Al of 24 meV/atom (e.g. compare to a phonon dispersion of Al in Ref. [11]), Fig. 2.1 compares (a) the vibrational free energy, (b) the entropy and (c) the isochoric heat capacity between a
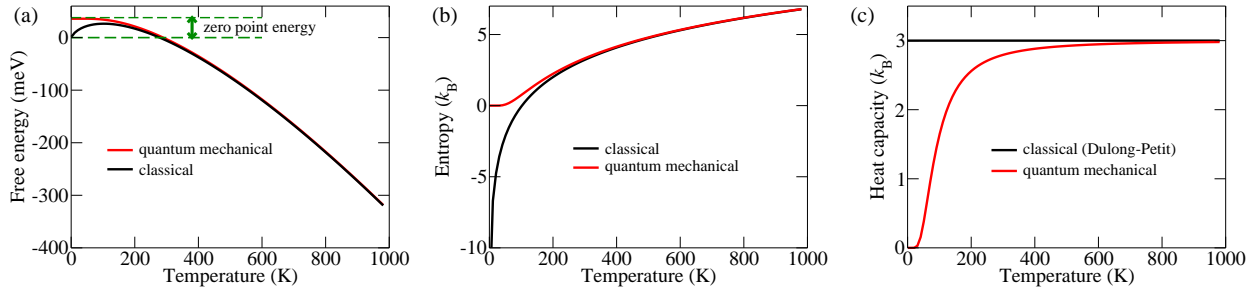
Figure 2.1: Comparison of the classical and quantum mechanical harmonic oscillator assuming a single frequency of $\omega_0 = 24$ meV. (a) Free energy in meV/atom as a function of temperature, $F_{\mathrm{qm}}^{\mathrm{atom}}(T)$ and $F_{\mathrm{cl}}^{\mathrm{atom}}(T)$, as defined in Eqs. 2.38 and 2.43. (b) Entropy in k_{B} gained by a derivative of the corresponding free energy using Eq. 2.2. The calssical definition is also given in Eq. 2.44. (c) Isochoric heat capacity as a function of temerature derived using Eq. 2.4.

quantum mechanical and a classical harmonic oscillator.

For the free energy in Fig. 2.1(a), the corresponding definitions for a single atom (3 degrees of freedom) have been used from Eqs. 2.38 and 2.43. It can be observed that at $T=0$ K both free energies differ by the zero point energy of the atom (indicated by green arrow). Already at room temperatures quantum mechanical effects are significantly diminished and the corresponding free energy converges to the classical limit at high temperatures. This has important consequences for *ab initio* molecular dynamics which are often performed classically. While those MD calculations will be close to the exact result at high temperatures, at low temperatures differences are to be expected due to the quantum mechanical nature of atomic motion. Fig. 2.1(b) compares the entropy by applying the derivation defined in Eq. 2.2 to the classical and quantum mechanical free energy. At high temperatures both curves converge, while, when decreasing the temperature, only the quantum mechanical oscillator approaches the limiting value of zero at $T=0$ K. This is a necessary condition in thermodynamics and is also known as the third law. Fig. 2.1(c) shows the isochoric heat capacity due to Eq. 2.4 where a drastic difference can be observed between the quantum and the classical oscillator. The law of Dulong and Petit (black solid line) is found for the classical harmonic system, 3 k_{B}, over the whole temperature range. This is however known to contradict experimental findings of solids at low temperatures. Using the quantum version of the harmonic oscillator, Einstein predicted in 1906 for the first time the correct behavior for the heat capacity of a carbon crystal also for temperatures below room temperature. With his work he showed that a quantitatively correct description can be gained assuming quantized energy level for the vibration of atoms. The energy quanta of lattice vibrations, $\hbar\omega$, are widely known as phonons.[1]

2.3.2 Debye and Grüneisen Approximation

A few year after Einstein's publication, accurate experimental measurements showed that the heat capacity of solids follows a T^3 dependence at low temperatures which could not be explained with Einstein's formula. In 1912 Debye suggested [23] that in a real crystal several frequencies are to be expected rather than a single frequency which was used in the Einstein solid. Debye argued that the interactions between the atoms, especially due to the nearest neighbors, are strong in the solid and that therefore atomic oscillations will be far from periodic. Analyzing the frequency spectrum of such a solid (e.g. by a Fourier transform of the atomic motion) would result in a *spectrum* of

---

[1]The quantity $T_E = \hbar\omega_0/k_{\mathrm{B}}$ is often referred to as the 'Einstein temperature'.
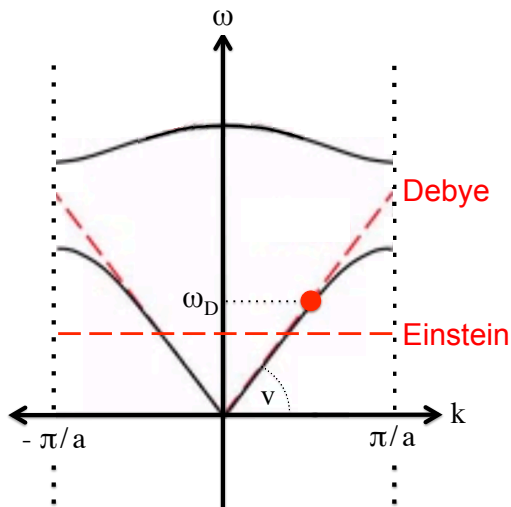
Figure 2.2: Exemplary dispersion relation (black solid) in one dimension for a crystal in comparison to the Einstein (red dashed, constant) and Debye (red dashed, linearly increasing) dispersion relation. While the crystal vibrates with a single averaged (mean) frequency ω_0 in the Einstein solid, the dispersion relation is given in Debye approximation by the speed of sound $v = \frac{\delta\omega}{\delta k}$. In the Debye approximation only frequencies are allowed up to ω_D and higher frequencies are cut off.

frequencies which is the direct consequence of atomic interactions. At that time however it was not possible to experimentally measure the frequencies within a solid and theoretical approximations were called for.

When analyzing the spectrum of frequencies in the solid two questions arise: a) which frequencies ω are present in the solid and b) to which wave length k does a particular frequency ω correspond to. The relation between the frequency and its wave vector is given by the dispersion relation. Debye assumed that the spectrum of available frequencies in the solid is similar to a homogeneous elastic continuum. He therefore approximated $d\omega/dk$ by a *constant* speed of sound $v = \frac{d\omega}{dk}$, a quantity which was experimentally accessible at the time of Debye and which corresponds to the long wave-length limit in the dispersion relation.[2] Since the speed of sound in a solid depends on the stiffness of the springs between the atoms — which are related to the atomic potential — a stiffer spring will transmit the sound wave quicker. Fig. 2.2 shows an exemplary dispersion relation with the assumed frequency dependence due to the Einstein and Debye model respectively.

Treating a d dimensional crystal of length L ($d = 1, 2, 3$, corresponds to an atomic chain of length L in one dimension or to a cube of edge length L in three dimensions) as a homogeneous elastic medium with $v = \frac{d\omega}{dk}$, an expression can be derived for the number of frequencies between ω and $\delta\omega$ — the phonon density of states (DOS)

$$g(\omega) = \frac{dN}{d\omega} = L^d \frac{d}{(2\pi)^d} s_d \frac{\omega^{d-1}}{v^d}. \tag{2.45}$$

Here, s_d is the "surface" of a sphere of radius 1 in $d = 1, 2, 3$ dimensions and $s_d = 2, 2\pi, 4\pi$ for $d = 1, 2, 3$ respectively [24]. $g(\omega)$ corresponds in three dimensions ($d = 3$) to

$$g_{3D}(\omega) = 3 \frac{\omega^2 V}{2\pi^2 v^3} \tag{2.46}$$

where $L^3 = V$ has been used and V corresponds to the volume of the considered crystal. Since in a real three dimensional crystal the number of modes is limited to $3N$ frequencies (N is the number

---

[2]In his model, Debye actually distinguished between a longitudinal and two transversal modes of oscillation.

of the atoms) Debye used the relation

$$3N = \int_0^{\omega_{\max}} g_{3D}(\omega) d\omega \tag{2.47}$$

to derive the highest frequency — a cutoff frequency $\omega_{\max}$ — in the system which is also known as the Debye frequency ω_D. Using Equations 2.46 and 2.47, ω_D can be calculated

$$\omega_D = \omega_{\max} = v(6\pi^2 \frac{N}{V})^{\frac{1}{3}} = 2\pi v(\frac{N}{V}\frac{3}{4\pi})^{\frac{1}{3}} \tag{2.48}$$

which depends only on the speed of sound v and the crystal density V/N, both experimentally well known. The Debye temperature is defined by

$$T_D = \frac{\hbar \omega_D}{k_{\mathrm{B}}}. \tag{2.49}$$

Since the speed of sound in a crystal corresponds to an average of sound velocities in longitudinal and transversal direction v_l and v_t, the speed of sound v in a crystal is

$$\frac{3}{v^3} = \frac{1}{v_l^3} + \frac{2}{v_t^3}. \tag{2.50}$$

Tabulated values of v_l and v_t for selected elements can be found in e.g. Ref. [25]. As an example we calculate the Debye temperature for aluminum: v_l and v_t are tabulated with 6374 m/s and 3111 m/s respectively [25]. This results in an effective speed of sound v of 3494.76 m/s using Eq. 2.50. The second factor which characterizes the Debye density of states and therefore ω_D in Eq. 2.48 is $\frac{N}{V}$ which can be calculated by the density of aluminum $\rho(Al) = 2.7$ g/cm^3 [25]:

$$\frac{N}{V} = \frac{N_A \rho(Al)}{M_{\mathrm{atom}}(Al)} = \frac{6.02 \times 10^{23} \mathrm{mol}^{-1} \times 2.7 \,\mathrm{g/cm}^3}{26.981 \mathrm{g/mol}} = 6.02 \times 10^{28} \,\mathrm{m}^{-3}. \tag{2.51}$$

Using the derived v and N/V in Eqs. 2.48 and 2.49 it follows that $\omega_D = 5.34 \times 10^{13}$ Hz which corresponds to a Debye temperature of $T_D = 408$ K for aluminum.

The free energy at a fixed volume in Debye approximation is given by the well known formula

$$F(T) = \frac{9}{8} k_{\mathrm{B}} T_D + k_{\mathrm{B}} T \left[3 \ln \left(1 - \mathrm{e}^{-T_D/T} \right) - D(T_D/T) \right] \tag{2.52}$$

with

$$D(y) = \frac{3}{y^3} \int_0^y \frac{x^3}{\mathrm{e}^x - 1} dx \tag{2.53}$$

and is seen to depend solely on the Debye temperature T_D. The definitions in Sec. 2 can be used to calculate all thermodynamic derivative quantities. The heat capacity in Debye approximation e.g. reads

$$C_V(T) = 9N k_{\mathrm{B}} \left[\frac{T}{T_D} \right]^3 \int_0^{T_D/T} \frac{x^4 \mathrm{e}^x}{(\mathrm{e}^x - 1)^2} \, dx \tag{2.54}$$

and correctly predicts the experimentally found temperature dependence at low temperatures which scales with T^3. Considering a linear dispersion relation, Debye improved Einstein's theory by effectively considering coupled atomic vibrations with an intuitive approximation for the lower part of the frequencies spectrum which is correctly given by the speed of sound in the solid.

While at low temperatures an accurate description for the heat capacity is given by Debye's approximation, going to higher temperatures significant deviations were found. The reason is that with increasing temperature the volume of the crystal expands and the corresponding frequencies decrease. This effect is often referred to as phonon softening and originates in the fact that increasing the atomic distance widens the potential well in which atoms vibrate and therefore the interatomic bonds become softer which results also in lower/softer frequencies. In order to make qualitative predictions of thermodynamic properties it is necessary to therefore access the frequency spectrum *and* its dependence on volume. One of the first approximations to this problem was to assume that the frequencies follow a simple exponential dependence of the change in phonon frequencies when changing the volume. This is known as the Grüneisen approximation which in the following is considered for cubic crystals when assuming an isotropic expansion of the lattice. The Grüneisen parameter γ_i is defined for every phonon mode i [22, 26] by

$$\gamma_i = -\frac{V}{\omega_i(V)}\frac{\partial \omega_i(V)}{\partial V} = \text{constant}, \tag{2.55}$$

with the corresponding volume dependent frequency $\omega_i(V)$. Solving this equation for $\omega_i(V)$ yields

$$\omega_i(V) = a_i V^{-\gamma_i}, \tag{2.56}$$

with an integration *constant a_i*. This can be simply verified by performing the derivative with respect to volume and substituting Eq. (2.56)

$$\begin{aligned} \frac{\partial \omega_i(V)}{\partial V} &= a_i(-\gamma_i)V^{-\gamma_i-1} \\ &= a_i V^{-\gamma_i}(-\gamma_i)V^{-1} \\ &= \omega_i(V)(-\gamma_i)V^{-1}. \end{aligned} \tag{2.57}$$

The total Grüneisen parameter is the sum of all γ_i's and introduces *at a constant volume* a change in the harmonic potential — more precisely from one harmonic potential to a generally softer harmonic potential. Since the potential now changes as a function of the volume the Grüneisen parameter is usually referred to as an indicator for the *anharmonicity* in a crystal. For the purpose of this thesis a different notation will be used however. Throughout this work a distinction is made between *quasiharmonicity* and *(explicit) anharmonicity*. While quasiharmonicity will be used when referring to changes in volume (while keeping a harmonic potential which however depends on the volume), the term anharmonicity will be used for explicit deviations of the atomic potential from a simple harmonic dependence $U = \frac{1}{2}\mu d^2$ where d is the atomic distance and μ the spring constant. While Debye and Grüneisen had to make assumptions for the frequency spectrum of the lattice vibrations and its dependence on the temperature, these quantities can nowadays be easily calculated — at least in harmonic approximation — for a given potential using *ab initio* methods.

2.3.3   Harmonic and Quasiharmonic Approximation

The presently most popular approach to compute thermodynamic properties from *ab initio* is the quasiharmonic (QH) approximation [27, 28]. Its basic idea is to apply the harmonic approximation at different volumes: the Helmholtz free energy $F(T)$ is derived in harmonic approximation at every volume $F(V_1, T), F(V_2, T), F(V_3, T), \ldots$ and a parametrization of these free energies is performed to obtain the final free energy surface $F(V, T)$. The parametrization of the free energy surface is standard and not the subject of this section. Since the $T=0\,\text{K}$ energy $E^0(V)$ is excluded from the

vibrational part, $F(V, T)$ can easily be obtained numerically by e.g. fitting low order polynomials as a function of volume for every temperature. The main focus of this section is the introduction of the harmonic approximation [29].

The basic concept of the harmonic approximation is similar to the Einstein solid, with one major difference: instead of a single frequency ω_0 which is allowed for atomic vibrations in the Einstein solid, the harmonic approximation samples all $3N$ frequencies of the crystal where N is the number of atoms. Every atom is connected to every other atom in the crystal by a *perfect* spring which obeys Hooke's law since the approximation is still harmonic. The interactions between the atoms result in a spectrum of eigenfrequencies. These frequencies are independent and the (quasi)harmonic approximation contains hence no phonon-phonon interactions. Instead of the approximative assessment of eigenfrequencies which was performed by Debye, the whole vibrational spectrum can be calculated nowadays numerically. The accuracy of the harmonic approximation is thus only dictated by the underlying potential and — the mapping onto a purely harmonic Hamiltonian.

The general expression for the Born-Oppenheimer surface defined in Eq. 2.20 — which defines the interatomic potential — can be expanded in a Taylor series around the equilibrium atomic positions $\{\mathbf{R}_i^0\}$ by

$$E^{\mathrm{BO}}(\{\mathbf{R}_i\}) \quad = \quad E_0^{\mathrm{BO}}(\{\mathbf{R}_i\}) + \underbrace{\frac{1}{2!} \sum_{ij}^{3N} \Phi_{ij}^{2\mathrm{ord}} \mathbf{u}_i \mathbf{u}_j}_{E^{\mathrm{h}}} + \underbrace{\frac{1}{3!} \sum_{ijk}^{3N} \Phi_{ijk}^{3\mathrm{ord}} \mathbf{u}_i \mathbf{u}_j \mathbf{u}_k + \ldots,}_{E^{\mathrm{ah}}} \qquad (2.58)$$

where $E_0^{\mathrm{BO}}(\{\mathbf{R}_i\})$ is the total energy for the crystal in equilibrium, the second term is the harmonic part and the following terms correspond to the anharmonic contribution of atomic vibrations. The derivatives are given by

$$\Phi_{ij}^{2\mathrm{ord}} \quad = \quad \frac{\partial^2 E^{\mathrm{BO}}(\{\mathbf{R}_i\})}{\partial \mathbf{R}_i \, \partial \mathbf{R}_j} = \frac{\partial F^{\mathrm{BO}}(\{\mathbf{R}_i\})}{\partial \mathbf{R}_i}, \qquad (2.59)$$

$$\Phi_{ijk}^{3\mathrm{ord}} \quad = \quad \frac{\partial^3 E^{\mathrm{BO}}(\{\mathbf{R}_i\})}{\partial \mathbf{R}_i \, \partial \mathbf{R}_j \, \partial \mathbf{R}_k} = \frac{\partial^2 F^{\mathrm{BO}}(\{\mathbf{R}_i\})}{\partial \mathbf{R}_i \, \partial \mathbf{R}_j}, \qquad (2.60)$$

$$\Phi_{ijkl}^{4\mathrm{ord}} \quad = \quad \ldots. \qquad (2.61)$$

where $F^{\mathrm{BO}}(\{\mathbf{R}_i\})$ are the Born-Oppenheimer forces which act on every atom in the crystal. In Eq. 2.58, the first order term $\Phi_i^{1\mathrm{ord}}$ has been omitted since it corresponds to the forces at equilibrium, which are zero. In *harmonic* approximation the potential is expanded only to second order. The central quantity in harmonic approximation is the *linear* force constant matrix $\Phi_{ij}^{2\mathrm{ord}} = \Phi_{ij}$ from which all phonon frequencies can be derived analytically as will be shown later. The total energy E^{h} for any configuration of atoms can be calculated in harmonic approximation by

$$E^{\mathrm{qh}} = \frac{1}{2} \sum_{ij}^{3N} \mathbf{u}_i \Phi_{ij} \mathbf{u}_j = -\frac{1}{2} \left(\sum_{i,j>i}^{3N} \Phi_{ij}(d_{ji} - d_{ji}^{\mathrm{eq}})^2 \right). \qquad (2.62)$$

Here, Φ_{ij} is the force constant matrix which holds the linear force constants and $\mathbf{u}$ is a displacement vector of the atoms from perfect equilibrium lattice and corresponds to an arbitrary configuration of atomic positions. Note that in this definition of Φ_{ij}, the variables i and j run

over the atoms *and* the displacement directions. Therefore $i = 1$ corresponds to displacing the first atom in the x direction, $i = 2$ corresponds to displacing the first atom in y direction and so on. The notation used for the term on the left side — which differs from the standard textbook definition but is equivalent — is chosen to illustrate the simple two dimensional nature of the force constant matrix. Substituting i with $i\alpha$ and j with $j\beta$ the standard textbook definition is obtained where greek letters α, β are used to indicate the Cartesian components of $\mathbf{u}_i$. The second term is derived in the Appendix A.1 on page 90. In this formulation it can be observed that the harmonic approximation is merely a sum which runs over all linear atomic force constants multiplied by the corresponding distance d_{ij} between two atoms in comparison to their equilibrium distance d_{ij}^{eq}. Evaluating the harmonic force constant matrices Φ_{ij} from *ab initio* can be performed by two approaches: perturbative methods based on linear response theory [30, 31] or the direct method — also called finite-displacement method — which calculates the response forces given a small atomic displacements [11, 32]. In the following only the direct method is shortly introduced.

Displacing an atom from its equilibrium position induces forces on all other atoms in the studied solid. Note that this is not the case in the Einstein solid where a force would only be found on the displaced atom. For small displacements $\mathbf{u}$ of an atom in a particular direction, the induced and numerically calculated forces on all atoms is proportional to the performed displacement and the atomic potential is probed in the 'true' harmonic regime. For Mg, tests have been performed as part of this PhD work which did show that atomic displacements ranging from 0.001 Å to 0.1 Å can be used and will all yield very similar free energies which differ at 1000 K by less than 3 meV. The harmonic free energy surface can therefore rigorously be calculated by numerical methods and is well defined. This is necessary since assessing the importance of anharmonic contributions — i.e. contributions which go beyond the harmonic approximation — is meaningful only when the correct harmonic part has been determined. Other ways of splitting the final free energy are possible but doing so the distinction between a harmonic and the anharmonic part would lose their meaning.

The two dimensional force constant matrix Φ for the entire solid can be obtained by displacing every atom i in the cell in the three Cartesian directions and calculating for each of those displacements the force on all atoms j. Symmetries can be used to reduce the number of necessary displacements to the irreducible one. Diagonalizing the force constant matrix of size $3N \times 3N$ the eigenfrequencies ω_i and the corresponding eigenvectors $\mathbf{k}_i$ can be directly obtained where i runs over the $3N$ entries of the matrix. The eigenfrequencies and eigenvectors are determined from the force constant matrix by solving the eigenvalue equation

$$\Phi\mathbf{k}_i = \omega_i^2\mathbf{k}_i. \tag{2.63}$$

The derived eigenfrequencies ω_i can then be used to calculate the free energy. Using the expression for the quantum harmonic oscillator in Eq. 2.34 and replacing ω_0 by ω_i one can sum over all $3N$ frequencies ω_i which are present in the solid to obtain the final temperature dependent free energy in harmonic approximation defined in Eq. 2.39. Using the small displacement method, the convergence of the free energy needs to be carefully checked with respect to the supercell size and with respect to the $\mathbf{k}$ point sampling. Diagonalizing Eq. 2.63 directly yields only the frequencies which correspond to commensurate $\mathbf{k}$-vectors within the sampled supercell. If the complete force constant matrix is known, the frequency at any $\mathbf{k}$-vector can be determined from the dynamical matrix which is defined as the Fourier transform of the force-constant matrix. For a monatomic crystal with a single atom in the primitive cell the dynamical matrix is defined by [29]

$$D_{\alpha\beta}(\mathbf{k}) = \frac{1}{m}\sum_j \Phi_{i\alpha\ j\beta}\ \exp\left[i\mathbf{k}\cdot(\mathbf{R}_i^0 - \mathbf{R}_j^0)\right]. \tag{2.64}$$

Here, m is the atomic mass and the Cartesian components α and β have been used. Using $D_{\alpha\beta}(\mathbf{k})$, the Brillouin zone can be integrated with a dense mesh of $\mathbf{k}$-vectors. This is readily found to significantly speed-up also the supercell convergence of the free energy. Having calculated $F^{\mathrm{h}}(T)$ at different volumes V, the quasiharmonic free energy surface $F^{\mathrm{qh}}(V, T)$ can be parametrized as mentioned before.

The quasiharmonic approximation is conceptually well defined and computationally efficient since it requires for high-symmetry configurations only very few configurations to be sampled to determine the full force constant matrix Φ [33]. A major drawback is, however, that its accuracy is difficult to assess. Its inherent approximation — a harmonic potential — does not represent the true nature of the interatomic potential. At low temperatures, only small atomic displacements occur in the system and a quadratic potential well is adequate. Consequently, thermodynamic properties have been found to agree well with experimental findings in the temperature regime close to $T=0\,\mathrm{K}$. The predictive power of the quasiharmonic approximation however decreases with increasing temperatures when atoms start to strongly deviate from their equilibrium positions and anharmonic effects become important. At these temperatures and in particular for non-harmonic systems, advanced methods are necessary to fully capture anharmonic contributions to the free energy.

2.3.4   Methods beyond the quasiharmonic approximation

In the following, two approaches are shortly introduced which go beyond the quasiharmonic approximation. These approaches — TDEP and SCAILD — stay in the harmonic framework but include finite temperature anharmonicity by sampling particular high temperature atomic configurations and map the corresponding forces onto a harmonic Hamiltonian. Concepts which explicitly allow a Hamiltonian which goes beyond second order are introduced thereupon in the following section 2.4.

Self-consistent *ab initio* lattice dynamics (SCAILD) method

SCAILD has been introduced in 2008 as a method to compute temperature dependent phonon spectra self consistently form first principles [34, 35]. Especially for structures which show a softening of the phonon dispersion at $T=0\,\mathrm{K}$ — those systems are not stable in harmonic approximation and cannot be calculated — this method is advantageous. SCAILD treats the calculation of temperature dependent phonon dispersions and material properties as follows: In a first step the harmonic approximation is solved and an initial harmonic dispersion is gained — which possibly might still contain imaginary modes. By defining a target temperature, average displacement amplitudes can be calculated and used to set up all the displacement vectors $\mathbf{k}$ which are contained in the sampled supercell. The displaced structures introduce forces which are calculated and consequently used to define a new dynamical matrix with new harmonic frequencies. These new eigenfrequencies together with the target temperature are again used to define new mean-square atomic displacements which eventually lead to a new force constant matrix. The procedure is repeated until the harmonic free energy of consecutive iterations converges to a predefined threshold. The resulting dispersion relations have been shown to agree well for all the sampled elements at high temperatures. An advantage of the SCAILD method is that no computationally demanding *ab initio* molecular dynamics have to be performed.

Temperature dependent effective potential (TDEP) method

A further approach to effectively capture anharmonic effects at high temperatures is the temperature dependent effective potential (TDEP) method [36]. The TDEP approach performs a phase space sampling derived from molecular dynamics to fit a set of temperature dependent coefficients $\Phi_{ij}^{\mathrm{eff}}(T)$ which replace the standard $T=0\,\mathrm{K}$ coefficients of the harmonic force constant matrix defined in Eq. (2.62). In this way the positions and forces obtained from MD are mapped onto a harmonic model Hamiltonian which is adjusted to a certain temperature and which is defined by minimizing the forces between DFT and the ones obtained from the model Hamiltonian. The (quasi)harmonic framework is retained and effective (quasi)harmonic free energies containing anharmonic corrections can be computed. The forces minimization is defined by

$$\min \Delta F = \frac{1}{N}\sum_{i}^{N}\left|F_i^{\mathrm{MD}} - F_i^{\mathrm{TDEP}}\right|^2 \tag{2.65}$$

where the molecular dynamics runs over N steps, F^{MD} are the corresponding DFT forces and F^{TDEP} the forces stemming from the harmonic TDEP force constant matrix $\Phi_{ij}^{\mathrm{eff}}(T)$ which is solved for in Eq. 2.65. The minimization of forces with respect to DFT molecular dynamics results in an TDEP Hamiltonian with an internal energy which equals the harmonic internal energy $\langle U_{\mathrm{TDEP}}\rangle = k_{\mathrm{B}}T3N$, where N is the number of atoms. The TDEP Hamiltonian can be regarded as the best possible harmonic one for a given temperature. In Sec. 3.1.3 a TDEP Hamiltonian is assessed among others as possible reference potential for thermodynamic integration. Although in the originally presented form of TDEP a harmonic model Hamiltonian was used, an extension to higher orders is in principle possible. A fundamental difference to the introduced SCAILD approach is the different phase space sampling. While TDEP samples directly DFT molecular dynamic, SCAILD evaluates snapshots which are self consistently predicted by the corresponding harmonic SCAILD Hamiltonian.

2.4 Solving lattice vibrations numerically exactly

In the previous section, *approximate* methods have been introduced which described the potential energy surface defined in Eq. 2.58 up to second order. The inclusion of higher orders however turns out to be a significant challenge. This section shortly describes two different approaches which take the missing higher order contributions into account.

2.4.1 Many-body perturbation theory

The general strategy of many-body perturbation theory (or higher order perturbation theory) is to separately calculate the second, third, fourth, etc. terms in Eq. 2.58 (see e.g. Ref. [37]). Recent reviews can be found e.g., in Refs. [38–40]. While the second order (harmonic approximation) includes only non interacting phonon's, the terms beyond second order correspond to phonon-phonon interactions and result in the creation or destruction of phonons. Similar to the harmonic approximation, the system is treated quantum mechanically and analytical formulas can be obtained which yield thermodynamic properties. Without going into the practical details which are involved when pursuing many-body perturbation theory calculations, it will be shown that the numerical demands increase exponentially with increasing order and that for this reason only a small subset of higher order terms can be calculated in practice.

A typical situation for any Taylor expansion, including Eq. 2.58, is that higher orders yield smaller contributions. In general however it is not known where to truncate this expansion. It is known that the third and forth order terms yield similar contributions to the free energy and need therefore to be considered simultaneously to obtain reliable results. Let us consider the amount of atomic configurations which are necessary to calculate the different terms $\Phi^{2ord}, \Phi^{3ord}, \Phi^{4ord}, \ldots$ of the Born-Oppenheimer surface. The general scaling is $((n-1) \cdot 3 \cdot N)^{(n-1)}$ where N is the number of atoms in the considered cell, 3 represents the three Cartesian directions and n is the respective order in the expansion. For the example of a $N = 32$ atom fcc crystal with a single atomic species it is therefore necessary to calculate 96 displacements in harmonic approximation — 2nd order — if no symmetries are applied. The 3rd and 4th order need already $\approx 10^5$ and $\approx 10^8$ calculations respectively. When symmetry considerations are taken into account, the necessary amount of displacements is one for the harmonic approximation, $\approx 10^3$ for the 3rd order and $\approx 10^4$ for the 4th order. It is seen that the number of terms rapidly increases which renders this ansatz a challenge for numerical approaches.

Very recent approaches of many-body perturbation theory to pristine fcc Aluminum managed to include all terms necessary up to third order fully from *ab initio* [41]. Another new implementation of higher-order perturbation theory, compressive sensing lattice dynamics (CSLD) [39] uses a scheme which determines the most relevant expansion coefficients from Eq. 2.58 and also their values from a set of DFT snapshots. Similar strategies are being applied in cluster expansion methods for determining the most relevant configuration interactions between atom pairs [42]. Related cluster expansion methods for the calculation of higher order anharmonic terms are also employed by Thomas et al. [43]. Ai et al. [44] and Chen et al. [40] have constructed a polynomial interatomic potential within next-nearest neighbors up to forth order. All these examples indicate that it is not trivial to rigorously determine the influence of the different terms entering Eq. 2.58. Furthermore it has been found that for strongly anharmonic crystals as He and Ne as well as for rare gas crystals perturbative methods fail [45]. Due to the high accuracy demands necessary in this study which were already mentioned in the introduction — better than 1 meV/atom for bulk systems and 0.1 meV/atom for systems containing defects — these approaches are not suitable for the present study. Methods which go beyond a perturbative treatment and are able to calculate the numerically exact free energy — and therefore the anharmonic contributions to *all* orders — will be introduced in the following.

2.4.2   Thermodynamic Integration

In comparison to many-body perturbation theory, classical statistical approaches (often referred to as sampling approaches) sample the full nuclei phase space explicitly by e.g., molecular dynamics or Monte Carlo methods [12]. Therefore, *all* orders in Eq. 2.58 are implicitly included in the sampling at the price that the necessary numerical calculations have to be performed at different temperatures. Thermodynamic integration [1, 46] is a particularly efficient statistical approach which is used to couple an arbitrary reference potential, e.g., a quasiharmonic reference, to e.g., the full DFT potential. Quantum mechanical effects, which are important in particular at low temperatures, can be explicitly included from the reference potential. The classically computed free energy difference between the systems which are being coupled is calculated *numerically exactly*.

Starting from a known reference potential U_0 where the free energy is known exactly or analytically — say a harmonic reference at a fixed external volume V and temperature T — the free energy difference can be computed with respect to another potential U_1, e.g. the full DFT potential energy surface. It has been noted earlier that a brute force sampling of phase-space requires on the order of $10^6 - 10^7$ *ab initio* computed configurations to converge the free energy to the here necessary

accuracy which is below 1 meV/atom for bulk systems. Depending on the quality of the reference potential U_0, thermodynamic integration allows to reduce the number of sampling configurations by usually more than 3 orders of magnitude providing thereby access to the numerically exact free energy surface. As was however mentioned in Sec. 2.1, the free energy difference ΔF between U_0 and U_1 cannot be calculated directly by casual molecular dynamics. The reason is that the sampled phase space as e.g. the averaged spatial coordinates, atomic distances and angles etc. are different for both systems U_1 and U_0 due to distinct partition functions. The free energy difference can nevertheless be calculated by defining a reversible path between both systems which is defined by a continuous variable. This variable is used to perform a (continuous) switching from a phase space sampling on U_0 to a phase space sampling on U_1. Averages of energy differences between both systems are computed for a distinct number of λ values and integrating those differences yields the numerically exact free energy difference ΔF.

A possible coupling coordinate for instance is the force, although other coupling coordinates are used in practice as well. Choosing the force as a coupling coordinate λ, the phase space is sampled for different λ values which linearly mix the forces stemming from U_0 and U_1 by

$$U_\lambda = (1 - \lambda)U_0 + \lambda U_1. \qquad (2.66)$$

At $\lambda = 0$, the phase space is evaluated with forces which are exclusively governed by U_0. At $\lambda = 0.75$ for instance only a quarter of an individual force is determined by U_0 while three quarters of U_1 forces are used. In this way different parts of phase space are sampled as a function of λ and results also in averaged atomic positions which change with the coupling strength. Gradually sweeping the λ parameter, a gradual change in the phase space sampling is obtained which also results in distinct averaged total energy differences between U_0 and U_1. For every λ value an MD has to be performed and the error of the averaged energy difference $\langle U_1 - U_0 \rangle_\lambda$ can be reduced by increasing the sampling time. By statistical

Figure 2.3: Exemplary thermodynamic integration for pristine bulk Ag (fcc) at the melting temperature of 1235 Kelvin. The integration is performed from a harmonic reference to DFT. The squares (red) corresponds to calculated averages between the DFT and the harmonic reference, $\langle U_{\mathrm{DFT}} - U_{\mathrm{qh}} \rangle_\lambda$, for distinct λ values. Integration of $\langle dU_\lambda/d\lambda \rangle_\lambda$ (red curve) yields the numerically exact free energy difference ΔF (gray shaded area) between DFT and the quasi-harmonic free energy.

considerations, the error of the free energy difference scales with $1/\sqrt{n}$ where n is the number of sampling points (atomic configurations). Integrating the finally obtained averages as a function of lambda, the numerically exact anharmonic free energy correction can be obtained.

The main steps for the derivation of thermodynamic integration are given in the following. Starting with the definition of the free energy in Eq. 2.10 which is dependent on the partition function, a well known result from classical statistical mechanics can be derived by considering the derivative of the free energy with respect to an 'external' change $d\lambda$

$$dF = \langle dU_\lambda/d\lambda \rangle_\lambda \, d\lambda. \qquad (2.67)$$
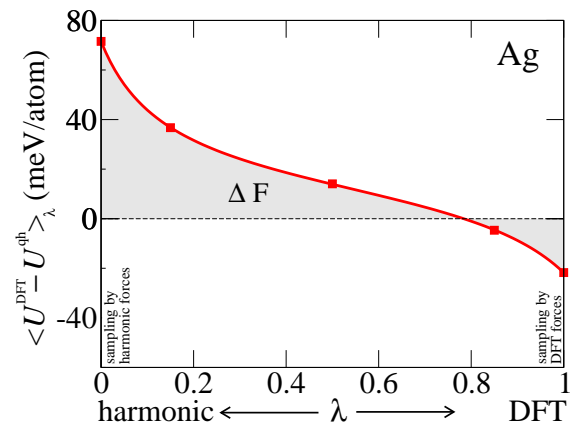
Here, a canonical ensemble average $\langle \ldots \rangle_\lambda$ is calculated for a given potential U_λ. Changes in U_λ by means of the reaction coordinate $d\lambda$ introduce a change in the Helmholtz free energy dF. The total free energy difference ΔF is defined by integration of dF over the coupling parameter λ

$$\Delta F = \int_0^1 d\lambda \; \langle dU_\lambda / d\lambda \rangle_\lambda. \tag{2.68}$$

An example for a $\langle dU_\lambda / d\lambda \rangle_\lambda$ curve is shown in Fig. 2.3 for fcc bulk Ag for a thermodynamic integration at the melting temperature (1234 Kelvin) from a harmonic reference potential ($U_0 = U_{\mathrm{qh}}$) to the full DFT potential ($U_1 = U_{\mathrm{DFT}}$).

A linear switching between U_0 and U_1 can be used as defined in Eq. 2.66 by which the free energy difference defined in Eq. 2.68 can be rewritten by

$$\Delta F = \int_0^1 d\lambda \; \langle U_1 - U_0 \rangle_\lambda. \tag{2.69}$$

A possible implementation of thermodynamic integration is by sampling distinct λ values and thereafter performing a fit through the numerically obtained points (this was similarly performed in Fig. 2.3 and resulted in the red curve). In case a harmonic potential has been chosen as reference, the calculated ΔF is the full anharmonic correction F^{ah} and equals the sum of all missing orders in a purely harmonic expansion of the Born-Oppenheimer surface in Eq. 2.58. The main challenge in thermodynamic integration is to minimize the error which is present in the thermodynamic average $\langle U_1 - U_0 \rangle_\lambda$ for the molecular dynamics runs at a given λ. How fast this difference converges is decisively influenced by the similarity of both Hamiltonians. An extensive test of different reference potentials for thermodynamic integration (usually denoted by U_0) to the full DFT potential (usually denoted by U_1) is performed in Sec. 3.1.

2.4.3   UP-TILD

The main challenge for the just introduced thermodynamic integration is its numerical convergence of the free energy difference ΔF. When performing thermodynamic integration using *ab initio* methods, a major speed-up can be achieved by the recently proposed *up-sampled thermodynamic integration using Langevin dynamics* (UP-TILD) method [2]. The basic idea is to separate the physical phase space sampling from the numerical convergence with respect to DFT parameters (e.g. cutoff, k-point sampling, etc.). A general observation when performing DFT molecular dynamics calculations is that fully converged cutoffs and k-points are in fact not necessary to sample the phase space with a high accuracy. The highly converged parameters change mainly the kinetic energy of the electrons which corresponds to a constant energy shift of the Born-Oppenheimer surface. The forces which determine the phase space sampling turn out to be sufficiently accurate already when using not the fully converged DFT parameters.

Therefore, a typical thermodynamic integration from e.g. a harmonic reference U^{qh} to a highly converged *ab initio* sampling, $U^{\mathrm{DFT,high}}$, can be split in two steps. In the first step the free energy difference is calculated by thermodynamic integration from the quasiharmonic reference to the DFT Hamiltonian with the not yet fully converged parameters which give the potential energy $U^{\mathrm{DFT,low}}$. Due to the similarity of the forces gained by the low converged DFT sampling to the fully converged DFT parameters, a nearly identical phase space is sampled. Therefore, in a consecutive step, a perturbative approach — the up-sampling — is applied which calculates the free energy difference between $U^{\mathrm{DFT,low}}$ and $U^{\mathrm{DFT,high}}$ based on the previously obtained sampling points as a function of λ. Due to the perturbative nature of the UP-TILD approach, its accuracy has been tested and

demonstrated in Refs. [2, 47] to be much better than one meV/atom in comparison to a sampling on the fully converged DFT parameters. The number of iteration steps is however significantly reduced using UP-TILD to about 10 calculations for a single lambda parameter in comparison to about several thousand DFT molecular dynamic steps using solely thermodynamic integration without UP-TILD. The calculation of the final vibrational free energy using UP-TILD can be summarized as follows

$$
\begin{aligned}
F^{\mathrm{vib}} &= F^{\mathrm{qh}} + F^{\mathrm{ah}} \\
&= F^{\mathrm{qh}} + \Delta F_{\mathrm{qh}}^{\mathrm{DFT,high}} \\
&= F^{\mathrm{qh}} + \Delta F_{\mathrm{qh}}^{\mathrm{DFT,low}} + \Delta F_{\mathrm{DFT,low}}^{\mathrm{DFT,high}} \\
&= F^{\mathrm{qh}} + \underbrace{\int_{\mathrm{qh}}^{\mathrm{DFT,low}} d\lambda \, \langle U^{\mathrm{DFT,low}} - U^{\mathrm{qh}} \rangle_{\lambda}}_{\text{thermodynamic integration}} + \underbrace{\int_{\mathrm{DFT,low}}^{\mathrm{DFT,high}} d\lambda \, \langle U^{\mathrm{DFT,high}} - U^{\mathrm{DFT,low}} \rangle_{\lambda}^{\mathrm{DFT,low}}}_{\text{UP-sampling}}
\end{aligned}
\tag{2.70}
$$

where $\langle \ldots \rangle_{\lambda}^{\mathrm{DFT,low}}$ indicates the up-sampling process which is performed on snapshots which are gained from the thermodynamic integration step. The corresponding energy difference $\langle \Delta E \rangle$ is calculated by an arithmetic mean

$$
\langle \Delta E \rangle = \langle U^{\mathrm{DFT,high}} - U^{\mathrm{DFT,low}} \rangle_{\lambda}^{\mathrm{DFT,low}} = \frac{1}{N^{\mathrm{UP}}} \sum_{u}^{N^{\mathrm{UP}}} \left[U_u^{\mathrm{DFT,high}} - U_u^{\mathrm{DFT,low}} \right]
\tag{2.71}
$$

for every λ point on the temperature and volume dependent free energy surface. N^{UP} is the number of up-sampled atomic configurations which are needed to gain the necessary statistical convergence but are significantly less than the number of MD steps for the phase space sampling by thermodynamic integration. In cases the ground state energy of the pristine cell $E_0^{\mathrm{BO}}(\{\mathbf{R}_i\})$ has been removed from the vibrational part defined in Eq. 2.58, it is also necessary to subtract the corresponding energies from every $U^{\mathrm{DFT,high}}$ and $U^{\mathrm{DFT,low}}$.

The significant reduction in calculation time is achieved due to the fact that (i) the numerical sampling on the not fully converged parameter set significantly saves computational time while (ii) the convergence of the UP-sampling is significantly enhanced due to the very similar phase space of the low and high Born-Oppenheimer surface. Fig. 2.4 illustrates the *up-sampled thermodynamic integration using Langevin dynamics* scheme introduced in Ref. [2]. It can be seen in (a) that the thermodynamic integration from a typical quasiharmonic reference needs several thousand steps to converge to the sub meV precision necessary for defect calculations. Using several of the gained structures and recalculating those with a higher DFT parameter set (up-sampling) is shown in (b). For those more demanding calculations typically only up to 30 uncorrelated MD configurations are necessary. Fig. 2.4(c) shows the sum of the UP-TILD procedure (red) which corresponds to the anharmonic contribution and consists of the thermodynamic integration (blue) energies and the up-sampling step (orange).
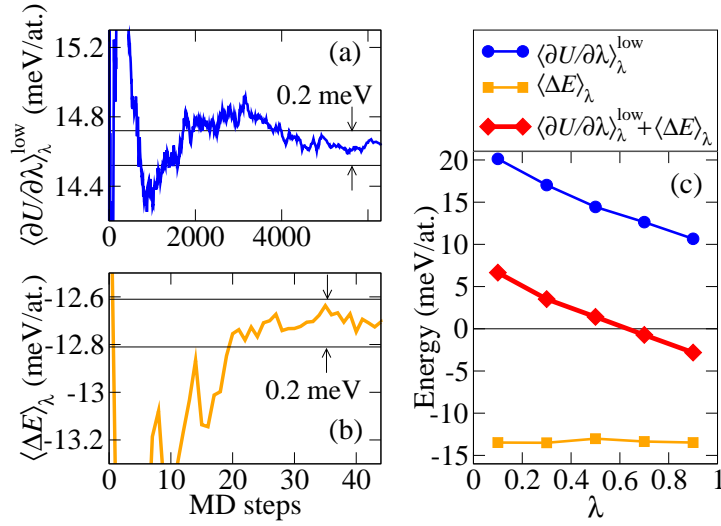
Figure 2.4: Illustration of the UP-TILD method: (a) Convergence of the average quantity $\langle U^{\mathrm{DFT,low}} - U^{\mathrm{qh}} \rangle_\lambda = \langle \partial U/\partial \lambda \rangle_\lambda^{\mathrm{low}}$ at $T = 900$ K and $\lambda = 0.5$ as a function of the number of molecular dynamics (MD) steps for the thermodynamic integration run on the not fully converged DFT parameter set. (b) Convergence of the average energy difference $\langle U^{\mathrm{DFT,high}} - U^{\mathrm{DFT,low}} \rangle_\lambda = \langle \Delta E \rangle_\lambda$ for a set of uncorrelated MD-structures taken from the $\lambda = 0.5$ run in a). (c) The λ dependence of the converged quantities from a) and b) and their sum, which corresponds to the highly converged quantity $\langle \partial U/\partial \lambda \rangle_\lambda^{\mathrm{high}}$, are shown. Figure and Caption were adapted from Ref. [2].

Chapter 3

Methodological developments

In this chapter the main methodological developments are discussed which were obtained during the present work:

- Section 3.1 summarizes the main observations and consecutive steps which led to the formulation of the *local anharmonic* (LA) approximation. Predictions of free energies using the *local anharmonic* approximation show a significantly improved accuracy in comparison to the quasiharmonic approximation. When used as reference potential for thermodynamic integration it yields a speed-up of approximately two orders of magnitude in comparison to the generally applied and previously used quasiharmonic reference.

- Section 3.2 shows the considerations which led to a *Local Grüneisen theory* (LGT) interpretation of defect formation. Using this formulation, it is possible to consolidate all experimentally measured high temperature vacancy formation energies of Al and Cu with fully *ab initio* computed results over the whole temperature range up to the melting point.

3.1 Efficient sampling of anharmonic contributions in bulk systems

The state-of-the-art methodology to study vibrational effects at high temperatures using first principles is the quasiharmonic approximation as introduced in Sec. 2.3.3. The errors due to this approximation are not well investigated since the full spectrum of vibrations, which would allow an unbiased comparison, is difficult to assess on an fully *ab initio* level. The importance to go beyond the harmonic picture by including the explicit anharmonic contributions due to phonon-phonon interactions has been recognized a long time ago [22, 26, 37, 48]. These contributions are responsible for deviations in specific heat, affect thermal expansion, phase transitions and significantly alter the behavior of thermoelectric materials [2, 9, 37, 48, 49]. The theoretical study of anharmonic contributions — which are all the missing vibrational contributions beyond the harmonic part — was for a long time significantly hindered due to a lack of accurate interatomic potentials in the early days of computer-aided materials design. Later, because the necessary tools to compute these contributions were still not developed on a fully *ab initio* basis. Early computational studies based on empirical potentials showed that anharmonic effects in bulk systems can in principle significantly modify free energies but were rejected since the strongly anharmonic results seemed unphysical at that time but also due to significant numerical convergence difficulties for the calculation of anharmonic contributions [50]. Only recent methodological advances, mainly based on thermodynamic

integration techniques (see Sec. 2.4.2) provided access to the numerically exact and fully *ab initio* free energy surface and did conclusively show the importance of anharmonic excitations for a few selected systems [1, 2, 9, 51]. From a physical point of view these studies were a significant break-through since the exact solution enabled for the fist time a true comparison of the errors introduced by different approximations. Examples include differences in the thermodynamic properties between e.g. LDA and GGA at finite temperatures as well as the assessment of established methods as the quasiharmonic, Einstein or the Debye model for calculating the heat capacity of solids. Having the full excitation spectrum at hand provides furthermore the basis for a detailed analysis, development and testing of new improved approximations.

Though the principle methods for the numerically exact thermodynamic solution are now known, fully *ab initio* based thermodynamic integration has been applied only to very few selected systems. All corresponding studies considered only one or at most two elements at a time. The reason is that the computational demands are still much too significant in order to apply these techniques on a regular basis. In fact, to avoid the computational cost of the numerically exact statistical sampling method as thermodynamic integration, approaches have been developed to get an approximate description of the potential energy surface which go beyond a quasiharmonic ansatz introduced in Sec. 2.3.3. Some of those approaches have been presented in Sec. 2. A main route in this direction is the treatment of anharmonic phonon-phonon interactions using second quantization [39–41], where the sum in Eq. (2.62) extends not only over pairwise interactions but includes higher order terms. Other approaches use machine learning [52] or cluster expansion [43] concepts for approximating the potential energy surface or replace the at $T=0\,\mathrm{K}$ computed force constant matrix by one that optimally describes thermodynamic averages at a given temperature [36]. In contrast to statistical sampling a systematic convergence of these approaches proves challenging making it difficult to assess their accuracy.

In order to practically enable fully *ab initio* based thermodynamic integration for a broad range of material systems, it is therefore necessary to significantly increase its efficiency which, as noted in Sec. 2.4.2, is exclusively governed by the reference potential at hand. At high temperatures only, inverse potentials have been successfully applied as a reference for the Al phase transition from solid to liquid [9]. However, as stated above, the quasiharmonic approximation is in general the method of choice when the whole temperature range of solid crystals is considered from $T=0\,\mathrm{K}$ up to melting [2, 53].

An investigation of the high temperature performance of the QH reference is performed in Sec. 3.1.1 and compared to the full DFT potential. The knowledge of this analysis will be used to derive a novel approach, the *local anharmonic* (LA) approximation, which combines ideas from the quasiharmonic approximation with anharmonic pair interactions and is presented in Sec. 3.1.2. It will be shown that (a) highly accurate forces and free energies can be predicted using the LA approach and that (b) using the LA as a reference for *ab initio* thermodynamic integration, results in speed-ups in comparison to the QH reference of approximately 2 orders of magnitude. In Sec. 3.1.3 alternative references are compared and insights from the derivation of the LA approximation are used to interpret thermodynamic integration results when using harmonic reference potentials.

3.1.1   Analysis of harmonic lattice dynamics at high temperatures

The currently established method to describe vibrational material properties at elevated temperatures from *ab initio* is the quasiharmonic approximation. Solid-state physics textbooks state that it yields results in agreement with experimentally observed thermodynamic properties in cases where (i) the deviation of the atoms from their equilibrium position is small (low temperatures) and (ii) the assumption of a harmonic potential (e.g. linear forces) holds [54]. A significant part of the work

summarized in this thesis was devoted to perform thermodynamic integration by using a harmonic potential as reference. Especially at high temperatures strong deviations from the true potential are observed which result in an significant increase of computational cost for thermodynamic integration. A major achievement of this study was therefore to investigate the high temperature properties of the QH reference and suggest a method which overcomes current limitations. In order to improve the efficiency of thermodynamic integration, the applied reference potential should meet several requirements:

- It should describe the correct phase space: Positions and forces of the atoms at a given temperature have to closely resemble the true positions and forces.

- The standard deviation of the reference energy with respect to the true potential has to be as small as possible. This is the main requirement for a fast convergence of thermodynamic integration and is prerequisite for minimal computational cost.

- The given reference potential should ideally be accurate over the whole temperature range, i.e. the same potential can be applied at any temperature.

In the following, the first of the above mentioned points is analyzed: the phase space behavior of the quasiharmonic approximation in comparison to the fully DFT computed one. The corresponding harmonic reference is derived for fcc Ag at $T=0\,\mathrm{K}$ via the small displacement method introduced in Sec. 2.3.3. The (harmonic) force constant matrix is gained by a single displacement due to symmetry considerations. It is subsequently used to perform a (harmonic) molecular dynamics run at the melting temperature of Ag at 1235 Kelvin. Any observable from this MD run can be compared against the same observable derived in a fully DFT-based MD which is performed for the same system and temperature.

For this purpose, MD data are analyzed to reveal correlations between atomic positions and various other phase space descriptors. A particularly useful quantity was found to be the distribution of the first nearest-neighbor vectors $\vec{d}_{1\mathrm{NN}}$ using [110] as the corresponding equilibrium direction. The vector between the two selected neighboring atoms was tracked in MD simulations. The QH and fully DFT-based distributions projected onto the (001) plane are shown in Fig. 3.1a. Both distributions show a distinctly different configuration space. The QH distribution shows a characteristic ellipsoidal shape which, due to its harmonic nature, is symmetric in longitudinal and transversal direction, $\vec{e}_{\mathrm{L}}$ and $\vec{e}_{\mathrm{T}}$ respectively. For the fully DFT-based MD a significantly different picture can be observed: only the transversal direction is symmetric, whereas a clearly non-symmetric (anharmonic) behavior becomes evident in the longitudinal direction. Going towards the atom which is (only in equilibrium) located at the origin, gives rise to a sharp, almost planar edge beyond which the probability to find a neighboring atom drops essentially to zero. On the opposite site, when considering long distances between the tracked neighboring atoms, a significant probability exists. The DFT distribution showing the correlation between both atoms can clearly not be described by a harmonic distribution. It is worth noting that the orientation of both symmetry axes in the full DFT case shown in Fig. 3.1a, $\vec{e}_{\mathrm{L}}$ and $\vec{e}_{\mathrm{T}}$, is very close to the symmetry direction observed for the QH distribution. The longitudinal direction between two atoms is in fact generally defined by the eigenvector corresponding to the highest eigenvalue of the harmonic force constant matrix. Effects on second, third, etc. nearest neighbors are shown in Fig. 3.1b for an EAM MD which was performed at 1000 Kelvin using a potential parametrization by Zhu et al. [55]. For first neighbors the same anharmonic behavior is observed while already second (and further) nearest neighbor interactions show a symmetric distribution. This underlines the localized character of the anharmonic interactions.
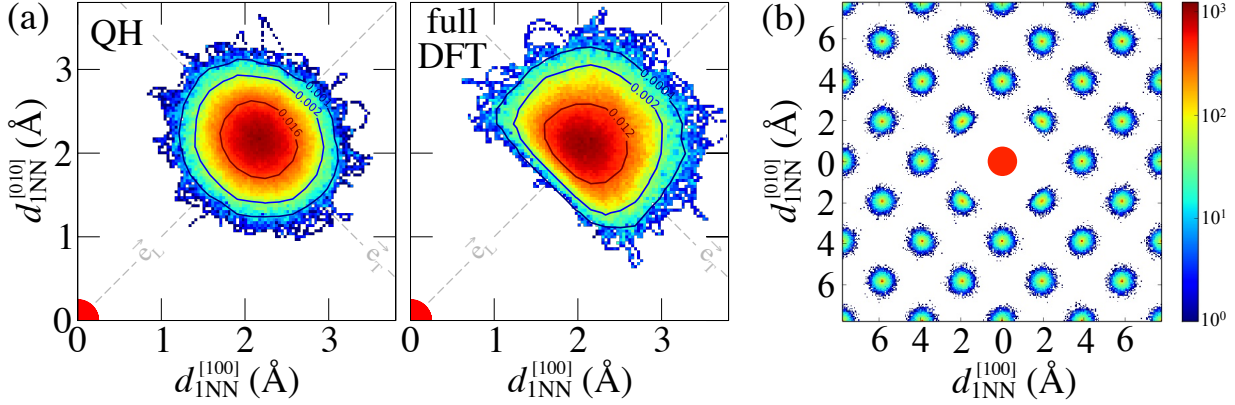
Figure 3.1: (a) Results from an MD run for Ag at the melting temperature. QH and fully DFT-based distribution of the projected nearest-neighbor vector $\vec{d}_{1NN}$ with the center of reference at (0,0) (red quadrant). (b) EAM MD for fcc Pd at 1000 Kelvin using the parametrization by Zhu et al. [55] with center of reference at (0,0). Projected are only atoms with equilibrium position on the (001) plane. As in the DFT case of Ag, only first nearest neighbors show an anharmonic distribution while second and further neighbors turn out to be symmetric and therefore not influenced by anharmonicity. Figure (a) and corresponding part of the caption is adapted from Ref. [33].

The distribution of the distance vectors between nearest neighbor atoms is surprising as it demonstrates an unexpectedly strong influence of anharmonicity and the failure of the quasiharmonic approximation to describe the corresponding configuration space correctly. First nearest-neighbor distances turn out to be a good collective coordinate to represent anharmonicity. To analyze the anharmonic longitudinal distances in detail the Gauss-broadened first nearest-neighbor distribution function[1] was computed

$$\rho_{1NN}(d) = \sum_j \delta([d_{1NN}^j - d_{1NN}^{eq}] - d) \tag{3.1}$$

where δ is the Dirac delta function and the index j runs over all first nearest-neighbor distances of all MD time steps of the simulation. For bulk Ag such a distribution function is shown in Fig. 3.2b for a DFT MD run at the melting temperature (red dashed line). Comparison with a distribution function obtained from a QH MD (black dashed line) reveals pronounced deviations: While the QH distribution is as expected fully symmetric, the one obtained at the full DFT potential shows a pronounced decrease/increase of configurations smaller/larger than the equilibrium distance. This redistribution of probabilities observed in the DFT MD case is not accessible by a symmetric QH potential. It provides direct insight into the mechanism of correlated atomic motion by which the system is able to lower its energy and which is the root of anharmonicity: By shifting shorter bond configurations to on average longer bonds, the system very effectively avoids the strong Pauli repulsion while having to pay only the price for stretched bonds were the corresponding interaction is softer. This picture becomes even more evident when the atomic distribution function is used to construct the corresponding effective potential

$$v_{eff} = -k_B T \ln \rho_{1NN}(d) \tag{3.2}$$

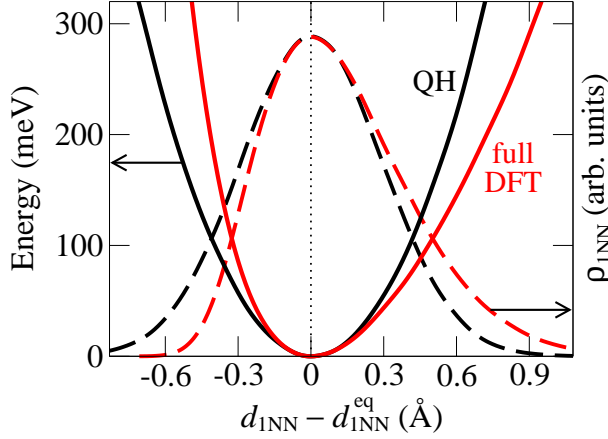[1]Every first nearest neighbor vector was considered without projecting on the [110] direction.

Figure 3.2: Gauss-broadened first nearest-neighbor distribution functions ρ_{1NN} (dashed lines; broadening parameter 0.04 Å^{-1}) and corresponding effective potentials v^{eff} (solid lines) obtained from full DFT (red) and QH (black) MD runs as a function of the first nearest-neighbor distance d_{1NN} around the effective equilibrium $d_{1NN}^{\text{eq,eff}}$ corresponding to the minimum of v^{eff}. The difference in $d_{1NN}^{\text{eq,eff}}$ obtained in quasiharmonic and full DFT calculations is shown in the appendix A.2 on page 92. Figure and caption are adapted from Ref. [33].

which is shown as solid black and red lines in Fig. 3.2. As expected the full DFT effective potential (red line) is harder/softer than the QH one for distances shorter/longer than the equilibrium bond length. In fact, the thus constructed nearest neighbor effective potential derived at the melting temperature of Ag closely resembles the well known features of a Morse potential that is often used to describe the strength and anharmonicity of a chemical bond at $T=0$ K.

3.1.2 Local Anharmonic (LA) approximation

In Sec. 3.1.1 a strongly anharmonic distribution was discovered for neighboring atoms at high temperatures. The corresponding distance dependence, shown in Fig. 3.2, was traced back to Morse-like local pairwise interactions. The question to be answered in this section is whether the corresponding interatomic potential can be *directly* derived at $T=0$ K, ideally from a few calculations. Exploring various strategies a method was derived which can be seen as an extension of the QH approach. Inspired by the distribution shown in Fig. 3.1a, the idea is to sample the local potential of atom pairs in longitudinal and both transversal directions, $\vec{e}_{\text{L}}$, $\vec{e}_{\text{T1}}$ and $\vec{e}_{\text{T2}}$ in contrast to the global x, y and z directions probed in quasiharmonic approximation. The longitudinal and transversal directions *for every atom pair* in the pristine cell can be obtained by a local unitary transformation which is given by the eigenvectors of the Hessian matrix. The transformation matrix, U^{loc}, is therefore an $N \times N$ block matrix with elements

$$U_{IJ}^{\text{loc}} = \nu_{IJ}, \qquad \Phi_{IJ}\nu_{IJ} = \vec{E}_{IJ}\nu_{IJ}, \tag{3.3}$$

where Φ_{IJ} corresponds to the quasiharmonic force constant matrix between atom I and J as defined in Eq. (2.62), ν_{IJ} is the corresponding matrix of eigenvectors, and $\vec{E}_{IJ}$ the vector of eigenvalues. Applying the $3{\times}3$ matrix U_{IJ}^{loc} on a Cartesian basis, $A^{xyz} = (\vec{e}_x, \vec{e}_y, \vec{e}_z)$, results in a *local* basis A_{IJ}^{loc} for *every* atom pair I and J

$$A_{IJ}^{\text{loc}} = (U_{IJ}^{\text{loc}})^{-1} \cdot A^{xyz} \cdot U_{IJ}^{\text{loc}}, \qquad A_{IJ}^{\text{loc}} = (\vec{e}_{\text{L}}, \vec{e}_{\text{T1}}, \vec{e}_{\text{T2}}), \tag{3.4}$$

with a longitudinal direction $\vec{e}_L$ and two transversal vectors $\vec{e}_{T1}$ and $\vec{e}_{T2}$ (orthogonal to $\vec{e}_L$, compare Fig. 3.1a). Using this new basis, the asymmetry in the DFT distribution function can be captured already from $T=0$ K calculations. For that purpose, it is necessary to start with a perfect crystal with all atoms in equilibrium positions. Then atom I is displaced by a vector u along each of the three principal vectors of A_{IJ}^{loc} as shown exemplary in Fig. 3.3. The $T=0$ K force $\vec{F}_J^{0K}$ and
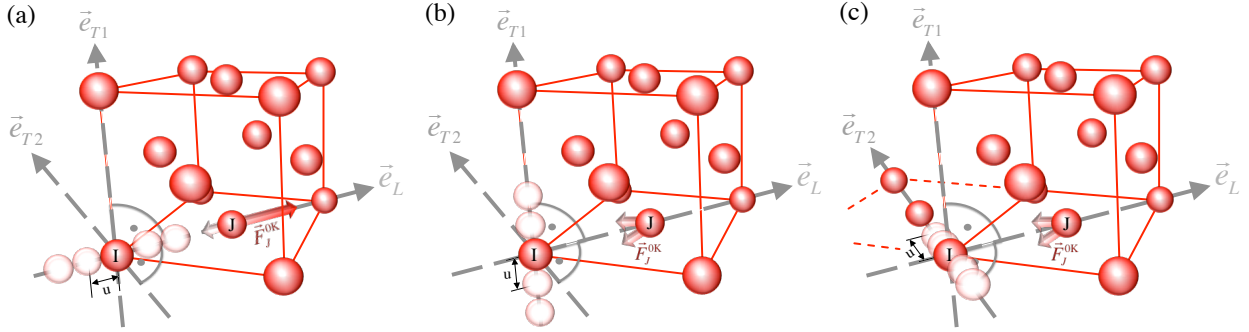
Figure 3.3: Mapping of forces in *local anharmonic* (LA) approximation for the example of an fcc crystal. Atomic positions of the pristine cell are shown in red. Atom I is displaced by a distance u a) along the longitudinal direction $\vec{e}_\mathrm{L}$ towards and away from its nearest neighbor atom J and b) and c) along the transversal directions $\vec{e}_\mathrm{T1}$ and $\vec{e}_\mathrm{T2}$ perpendicular to $\vec{e}_\mathrm{L}$. The force on atom J, $\vec{F}_J^{0\mathrm{K}}$, is projected onto the corresponding orthogonalized displacement direction as explained in the text (here $\vec{e}_\mathrm{L}$, $\vec{e}_{\mathrm{T1}'}$ and $\vec{e}_{\mathrm{T2}'}$) to get the parametrization of the corresponding longitudinal or transversal force $F_a(u)$ with $a =$L, T1, T2. When parametrizing transversal forces, longitudinal forces are subtracted from $\vec{F}_J^{0\mathrm{K}}$ first.

corresponding energy potential on the neighbor atom J are then mapped as

$$F_a(u) = \vec{F}_J^{0\mathrm{K}}(u\,\vec{e}_a) \cdot \vec{e'}_a, \qquad V_a(u) = \int_0^u F_a(u')du', \qquad (3.5)$$

with $a =$L, T1, T2. Vectors $\vec{e'}_a$ are gained by orthogonalization: When parametrizing the transversal forces by displacing atom I from its original position, the coordinate system of $\vec{e}_{\mathrm{IJ}}$, $\vec{e}_\mathrm{T1}$ and $\vec{e}_\mathrm{T2}$ is not strictly orthogonal since $\vec{e}_\mathrm{L}$ has to be replaced by $\vec{e}_\mathrm{IJ}$ due to the displacement u. Vector $\vec{e}_\mathrm{IJ}$ can be envisioned by connecting one of the displaced atoms in Fig. 3.3(b) with atom J. Doing this it is seen that the corresponding direction in $\vec{e}_\mathrm{T1}$ is not orthogonal to the just created vector. Applying a Gram-Schmidt process [56] to the vectors of A_{IJ}^loc a fully orthogonal coordinate system is recovered

$$A_{IJ}^{\mathrm{loc}'} = \vec{e'}_a = (\vec{e}_\mathrm{IJ}, \vec{e}_{\mathrm{T1}'}, \vec{e}_{\mathrm{T2}'}) \qquad (3.6)$$

spanned by the longitudinal direction $\vec{e}_\mathrm{IJ}$. The effects of orthogonalization turn out to be small since the significant part of the restoring force on atom J, $\vec{F}_J^{0\mathrm{K}}$, is directed along the displacement direction in fcc crystals. Crystal symmetries are employed to reduce the number of $T=0$ K calculations required to obtain the force and energy parametrizations to the irreducible ones. It has to be noted that once the longitudinal force $F_\mathrm{L}(u)$ is parametrized, it is subtracted from $\vec{F}_J^{0\mathrm{K}}$ for the parametrization of the transversal forces $F_{T1}(u)$ and $F_{T2}(u)$. Doing this ensures the sum of the parametrized $T=0$ K longitudinal and transversal forces to be close to the true DFT forces (not exact due to the projection).

Having the parametrization of the forces and potentials available, Eq. (3.5), the forces and energy for any atomic configuration, e.g., during an MD simulation, can be straightforwardly computed. While the scalar component of the force is given in Eq. 3.5, the force *vector* for example in an MD run $\vec{F}_J^\mathrm{MD}$ on an atom J is given by

$$\vec{F}_J^\mathrm{MD} = \vec{F}_\mathrm{L} + \vec{F}_\mathrm{T1} + \vec{F}_\mathrm{T2}, \qquad (3.7)$$

$$\vec{F}_\mathrm{L} = F_\mathrm{L}(|\vec{d}_{IJ}| - d_{IJ}^\mathrm{eq})\,\vec{e}_\mathrm{IJ}, \quad \vec{F}_{\mathrm{T}x} = F_{\mathrm{T}x}(\vec{d}_{IJ} \cdot \vec{e}_{\mathrm{T}x})\,\vec{e}_{\mathrm{T}x'}, \qquad (3.8)$$

with $\vec{e}_{IJ} = \vec{d}_{IJ}/|\vec{d}_{IJ}|$, $\vec{d}_{IJ}$ the vector between atom I and J during an MD run and $\vec{e}_{\mathrm{T}x'}$ the orthogonalized transversal vectors. The energy reads

$$E^{\mathrm{LA}} = \frac{1}{2} \sum_{J}^{N} \sum_{I}^{n} \left(V_{\mathrm{L}}(u_{IJ}) + V_{\mathrm{T1}}(u_{\mathrm{T1}}) + V_{\mathrm{T1}}(u_{\mathrm{T2}})\right), \tag{3.9}$$

with n the number of nearest neighbors, $u_{IJ} = |\vec{d}_{IJ}| - d_{IJ}^{\mathrm{eq}}$, $u_{\mathrm{T1}} = \vec{d}_{IJ} \cdot \vec{e}_{\mathrm{T1}}$, $u_{\mathrm{T2}} = \vec{d}_{IJ} \cdot \vec{e}_{\mathrm{T2}}$, $\vec{d}_{IJ}$ the vector between atom I and J, and with d_{IJ}^{eq} the equilibrium distance of these atoms at $T=0\,\mathrm{K}$. Since the proposed method is based on probing the local anharmonic potential the formalism was named *local anharmonic* (LA) approximation.

In the conventional QH direct-force-constant approach the force constants Φ_{IJ} are formally restricted to the limit of infinitesimally small displacements (typical QH displacements are ≈ 0.01 Å). In LA approximation however significantly larger displacements are sampled during the LA parametrization [u in Eq. (3.5)] to accurately reproduce the anharmonic character. The magnitude of the displacements is dictated by the distribution function at the given temperature (see red dashed line in Fig. 3.2 and Fig. 3.4a) and can reach values of >1 Å, i.e., two orders of magnitude larger than those of the QH method. The resulting dependence of the forces in particular of the longitudinal component is no longer a linear function but highly anharmonic.
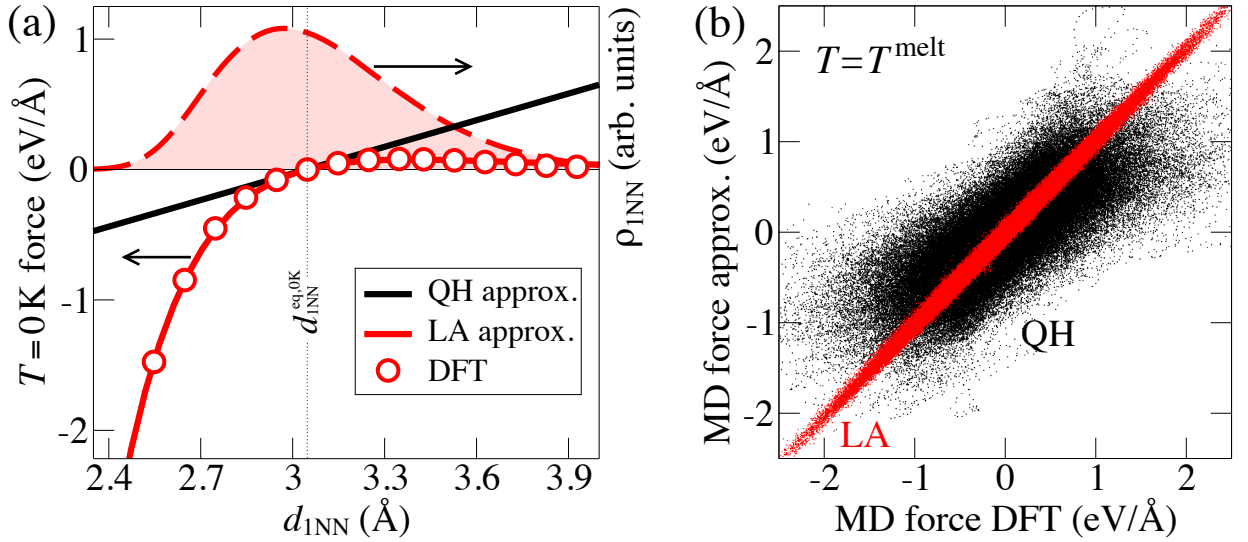
Figure 3.4: Application of the *local anharmonic* (LA) approximation to Ag. (a) Longitudinal $T=0\,\mathrm{K}$ DFT forces (open red circles) obtained by displacing an atom from its $T=0\,\mathrm{K}$ equilibrium position, $d_{1NN}^{\mathrm{eq},0\mathrm{K}}$, towards and away from its next-nearest neighbor. The red solid line shows a fit according to the LA approximation and the black solid line using the QH approach. The shown displacement region is dictated by the distance distribution at the melting temperature (red dashed line). (b) Comparison between full DFT and LA forces (red dots), and between full DFT and QH forces (black dots) for configurations obtained from a fully DFT-based MD run at the melting temperature. Figure and caption are adapted from Ref. [33].

An example for the DFT forces that are used to parametrize the LA approximation, $\vec{F}_{J}^{0\mathrm{K}}$, are shown in Fig. 3.4a for fcc Ag. The shown distribution function $\rho_{1NN}^{\mathrm{DFT}}$ is taken from a DFT MD run at the melting temperature. It extends over atomic distances from 2.4 Å to 3.9 Å. The corresponding longitudinal anharmonic forces (open red circles) which are directly derived from $T=0\,\mathrm{K}$ DFT displacements are highly non-linear in this regime. Trying to fit the DFT forces by a

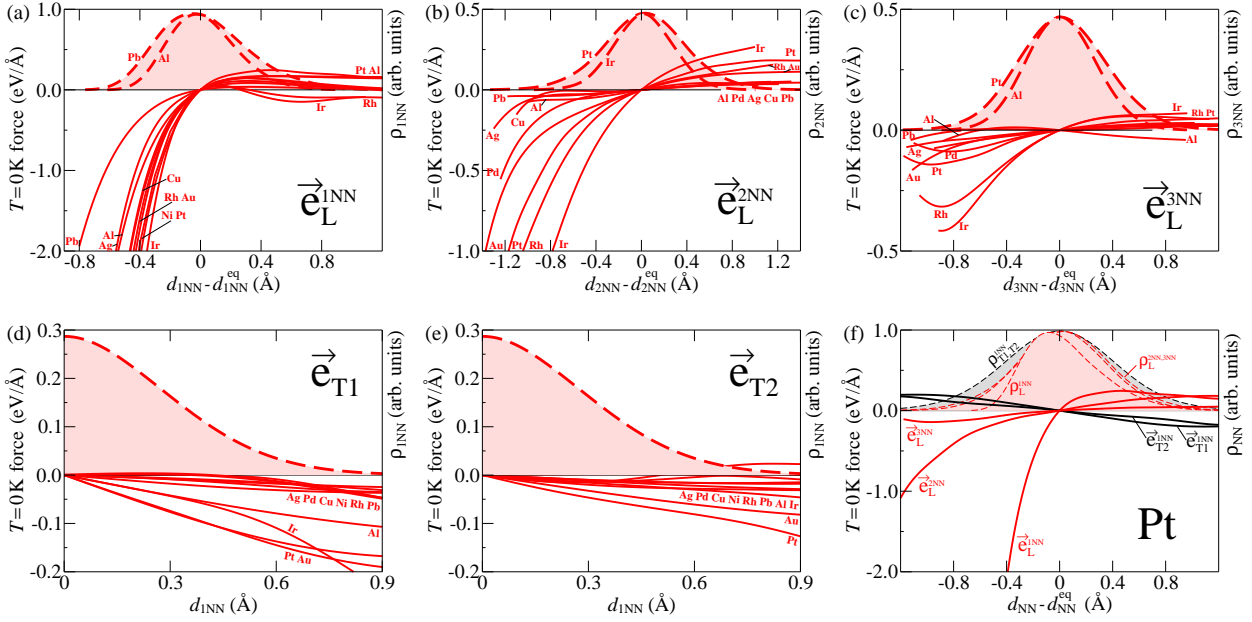Figure 3.5: Comparison of DFT forces derived at $T=0\,\text{K}$ for an extensive set of unary fcc-metals: Al, Ag, Au, Cu, Ir, Ni, Pb, Pd, Pt, Rh. All forces are derived by displacements in a $3 \times 3 \times 3$ cubic fcc supercell. (a-e) For the purpose of representation only the narrowest and broadest corresponding distributions (red shaded) are shown for all considered elements at their respective melting point. The shown magnitude of displacement was adapted for every element accordingly to the corresponding distribution. Figures (a), (b) and (c) compare longitudinal forces for different neighbor shells (first, second and third). Figures (a), (d) and (e) show for *first nearest neighbors* the forces in the three major directions of A_{IJ}^{loc}: $\vec{e}_{\text{L}}$, $\vec{e}_{\text{T1}}$ and $\vec{e}_{\text{T2}}$ which correspond to the displacements indicated in Fig. 3.3 (a), (b) and (c) respectively. Notice that first nearest neighbor forces in $\vec{e}_{\text{L}}$ direction are about 10 to 20 times higher compared to forces in $\vec{e}_{\text{T1}}$ and $\vec{e}_{\text{T2}}$ direction. Notice further that second nearest neighbor forces are strongest for Ir, Rh, Pt and Au and are much greater than first nearest neighbor transversal forces. Third nearest neighbor forces are observed to be significantly smaller as first and second nearest neighbor longitudinal forces. To emphasize the different scales used in Figs. (a) to (e), Fig. (f) combines all different force contributions for Pt in one picture.

linear function (black solid line) as inherently done by the quasiharmonic approximation is bound to introduce a large error. Rather a Morse potential is found to provide an accurate description of the longitudinal DFT $T=0\,\text{K}$ forces (red line in Fig. 3.4). Using a Morse-type fit is however not compulsory and in principle any function reproducing the anharmonic $T=0\,\text{K}$ forces correctly is feasible. A direct assessment of the quality of the LA approximation is obtained by comparing DFT finite-temperature forces extracted during a DFT-MD run with forces computed for the identical structures but using the LA potential. Such a comparison for Ag at its melting temperature is shown in Fig. 3.4b (red dots). A dramatically improved Person correlation coefficient [57] can be observed for the LA approach (0.997) as compared to the QH approximation (0.765) for which the forces (black dots in Fig. 3.4b) scatter largely around the DFT forces with deviations up to 2 eV/Å.

For a wide range of fcc elements, Al, Ag, Au, Cu, Ir, Ni, Pb, Pd, Pt, Rh, a systematic assessment of longitudinal and transversal forces was performed which define the LA potential. Fig. 3.5 summarizes the obtained $T=0\,\text{K}$ results by comparing in (a), (b) and (c) first nearest neighbor forces in the three principal direction of A_{IJ}^{loc}, $\vec{e}_{\text{L}}$, $\vec{e}_{\text{T1}}$ and $\vec{e}_{\text{T2}}$ with longitudinal forces on (d) second and (e) third nearest neighbors. This comparison of Fig. 3.5a-e reveals that for all elements the magnitude of longitudinal first nearest neighbor forces is in fact the dominant contribution to capture anharmonicity and is seen to be about a factor 10 to 20 higher compared to first nearest

	Al	Ag	Au	Cu	Ir	Ni	Pb	Pd	Pt	Rh
$\Delta F^{\mathrm{ah}}_{\mathrm{QH}}$	4	16	27	9	17	6	2	6	22	10
$\Delta F^{\mathrm{ah}}_{\mathrm{LA\ (L)}}$	6	1	25	1	6	0	1	3	24	3
$\mathbf{\Delta F^{\mathrm{ah}}_{\mathrm{LA\ (L+T1)}}}$	**1**	**1**	**3**	**0**	**6**	**0**	**1**	**1**	**4**	**3**
LA$_{(\mathrm{L})}$ Speed-up	8	244	37	200	22	158	29	67	23	49
LA$_{\mathbf{(L+T1)}}$ Speed-up	**52**	**523**	**213**	**256**	**22**	**158**	**29**	**198**	**39**	**49**

QH: Error: 2-27 meV
~ 1 static DFT calculation

route (i): Error: 0-6 meV
~10 static DFT calculations

route (ii): Error: 0 meV
DFT MD

Table 3.1: (Rows 1-3): Error in the free energy (in meV/atom at T^{melt} and V^{melt}) for the various approximations (QH, LA route (i) as described in text with and without $\vec{e}_{T1}$) with respect to the numerically exact DFT free energy. (Row 1): QH approximation. (Row 2): LA approximation using a first nearest-neighbor longitudinal Morse parametrization only. (Row 3): As row 2, but augmented with a transversal function in $\vec{e}_{T1}$ direction corresponding to the second largest eigenvalue in Eq. (3.3). (Rows 4 and 5): Speed-up factors for the thermodynamic integration when replacing the QH by the LA reference. The speed-up is defined by $n^{\mathrm{QH}}/n^{\mathrm{LA}}$, where n^{QH} and n^{LA} are the MD steps necessary to reach a given standard error (typically 1 meV/atom) with a QH and LA reference. Table and caption are adapted from Ref. [33].

neighbor transversal forces. The $\vec{e}_{\mathrm{T}1}$ and $\vec{e}_{\mathrm{T}2}$ directions are in an fcc crystal not equivalent (see Fig. 3.3). While the $\vec{e}_{\mathrm{T}2}$ displacement points towards a nearest neighbor and considering atom J defines the place of closest possible packing in fcc, $\vec{e}_{\mathrm{T}2}$ points in the direction to the second nearest neighbor and in direction perpendicular to the closest packed plane. It is therefore observed that forces in $\vec{e}_{\mathrm{T}2}$ direction have the smallest magnitude with roughly half the force in $\vec{e}_{\mathrm{T}1}$ direction. The magnitude of longitudinal forces on second neighbors on the other hand is seen to be significant and much stronger than first neighbor forces in transversal direction, even when taking into account that fcc crystals have only 6 second but 12 first nearest neighbors. It was furthermore found that the magnitude of the calculated DFT forces scales in good agreement with the eigenvalues for the corresponding eigenvector in QH approximation. It is therefore possible to estimate the importance of forces in a certain direction just by solving the quasiharmonic eigenvalue equation. Taking for all considered elements an average of their eigenvalues in first neighbor longitudinal direction and scaling it to 1, the corresponding mean eigenvalues in $\vec{e}_{\mathrm{T}1}$ and $\vec{e}_{\mathrm{T}2}$ direction amount to 0.12 and 0.032. Considering Fig. 3.5 it was chosen to include step by step all contribution starting with the strongest. The in the following presented investigations therefore include contributions in first neighbor $\vec{e}_{\mathrm{L}}$ and $\vec{e}_{\mathrm{T}1}$ direction while second and further nearest neighbors as well as $\vec{e}_{\mathrm{T}2}$ on first neighbors is ongoing work.

To compute anharmonic free energies, the LA approximation can be used following two principle routes:

(i) A direct computation of _local anharmonic_ free energies using Eq. (3.8). This is performed by a thermodynamic integration from the quasiharmonic reference to the LA potential at negligible computational cost once the LA potential is derived. Using this route less than ten static DFT calculation are sufficient for fcc bulk elements, i.e., there is no need for expensive DFT MD. Row 3 of Tab. 3.1 summarizes the accuracy which can be gained using this route.

(ii) Calculation of the numerically exact DFT free energies using the LA potential as a reference system for thermodynamic integration to the full DFT energy surface. Row 5 of Tab. 3.1 summarizes the speed-up factors which can be gained in comparison to a standard QH reference potential.

Following route (i), the LA potential was computed for all studied elements by a few DFT

displacements at $T=0\,\mathrm{K}$, i.e., without any computationally expensive DFT MD. The free energy in the LA approximation is given by

$$F_{\mathrm{LA}}^{\mathrm{ah}} = \widetilde{F}_{\mathrm{LA}}^{\mathrm{ah}} + \Delta E_{\mathrm{DFT}}^{\mathrm{LA}} \tag{3.10}$$

where $\widetilde{F}_{\mathrm{LA}}^{\mathrm{ah}}$ is the free energy obtained by thermodynamic integration from QH to LA potential and

$$\Delta E_{\mathrm{DFT}}^{\mathrm{LA}} = \frac{1}{N} \sum_{i}^{N} (E_i^{DFT} - E_i^{LA}) \tag{3.11}$$

is an averaged difference between LA and DFT energies, E^{LA} and E^{DFT}. This average difference is obtained from N uncorrelated snapshots taken from a computationally inexpensive LA MD and corresponds to an *UP-TILD* like procedure additional to thermodynamic integration. $\Delta E_{\mathrm{DFT}}^{\mathrm{LA}}$ is found to converge for all studied elements within a few (<5) uncorrelated structures to better than 1 meV. The actual assessment of the achievable accuracy in LA approximation using route (i) in comparison to fully *ab initio* computed anharmonic free energies is shown in row 3 of Tab. 3.1, $\Delta F_{\mathbf{LA}\ (\mathbf{L+T1})}^{\mathrm{ah}}$. The errors in LA approximation are in the order of a few meV for all elements highlighting the accuracy that can be achieved by very few (here < 10) $T=0\,\mathrm{K}$ DFT calculations. In particular for row 3 of Tab. 3.1, four displacements were calculated using DFT to parametrize the LA potential (longitudinal and $\vec{e}_{T1}$) and consequently gain $\widetilde{F}_{\mathrm{LA}}^{\mathrm{ah}}$, while two to four DFT calculations were necessary to converge $\Delta E_{\mathrm{DFT}}^{\mathrm{LA}}$ to better than 1 meV.

Following the second route (ii) numerically exact DFT free energies were computed by thermodynamic integration with the LA approximation as reference. Since the LA forces faithfully reproduce the DFT forces (Fig. 3.4b), the LA reference and the original system span very similar configuration spaces allowing to obtain a very fast statistical convergence. The speed-up factors with respect to the previously applied QH reference are given in the last row of Tab. 3.1, $\mathrm{LA}_{(\mathbf{L+T1})}$ Speed-up. Using the LA method the computational effort can be reduced by about 2 orders of magnitude: The previously necessary 10^4 MD steps for thermodynamic integration are now reduced to about (and partly less than) 10^2 steps when calculating the numerically exact DFT free energy. An actual example for the computational time in CPU hours is given in the following for Ag at the melting point and corresponding volume. The considered free energy contributions were converged to better than 1 meV/atom. A single quasiharmonic free energy calculation (single displacement for the bulk fcc case) takes 6 CPU hours (single core, Intel CPU, clock rate of 1800MHz, 8 cores per node) while the electronic calculations are computationally negligible. Using the QH reference for the anharmonic contribution of the free energy at melting, a total of 31.050 MD steps were required to reach the desired statistical accuracy and amounted to 4504 CPU hours (same architecture as mentioned above). Changing to the LA reference, < 9 CPU hours were used for the necessary 60 total MD steps. The additional UP-TILD like steps expressed by $\Delta E_{\mathrm{DFT}}^{\mathrm{LA}}$ are significant for the convergence of free energies but negligible in comparison to thermodynamic integration steps. For the considered Ag free energy, 15 UP-TILD steps were necessary using the QH reference compared to in total only 2 UP-TILD steps using LA. This example illustrates that the LA method opens the path towards routine, numerically exact *ab initio* free energies.

Having derived a simple parametrization for highly accurate free energies over the whole temperature range the question arises whether the proposed method can be efficiently used beyond the integral characteristics, i.e. for the calculation of phonon dispersion, linewidths and related parameters. This would allow to employ the presented approach in an even broader context. Focusing on one of the quantities — the phonon linewidth — first encouraging tests were performed. For the sample system, fcc bulk aluminum, an excellent agreement with experiment is found. Using the

calculated DFT longitudinal LA potential within the LAMMPS package [58] the X-point of phonon dispersion was sampled at a temperature of 300 K. A phonon linewidth of 1.3±0.4 meV is obtained which is close to the experimentally measured values of 1.75±0.9 meV [60]. Prior studies using many-body perturbation theory to third order [59] and employing the GGA functional resulted in a linewidth of 2.3 meV for the X-point. A systematic study of the performance to accurately compute non-integral finite temperature quantities goes beyond the present thesis and will be the focus of future studies.

3.1.3 Comparison of reference potentials

Tab. 3.1 summarized the performance of generally applied quasiharmonic approximation as reference potential for thermodynamic integration in rows 4-5. In this section other possible references are tested versus the QH approach for the example of Al and Cu as shown in Fig. 3.6. One of the tested methods is the inverse-power potential [9] (IP) which mixes the standard harmonic Hamiltonian derived from DFT with a repulsive pair potential. The pair potential parameters and the amount of mixing are determined in such a way as to ensure the minimization of the standard deviation σ for thermodynamic integration — in principle at a given temperature. The other tested approach is the temperature dependent effective potential (TDEP) method [36] which was already shortly introduced in Sec. 2.3.4.

In Fig. 3.6(a) the Speed-up and in (b) the corresponding standard deviation as a function of coupling strength λ are shown for MD runs at the corresponding melting temperature. The considered reference potentials contain different amounts of anharmonic contributions: LA (fully anharmonic), inverse-power potentials [9] (harmonic Hamiltonian mixed with anharmonic pair interactions), TDEP [36] and QH (fully harmonic). In (a) it can be observed that the quality of the thermodynamic integration reference improves with increasing degree of anharmonicity for both considered elements. The standard deviation, σ, shown in Fig. 3.6b is a direct measure for the fluctuations in total energy differences between DFT and the reference potential as obtained by finite temperature MD. Both anharmonic potentials, LA and IP, significantly reduce the standard deviation with respect to the harmonic references. It has to be stressed that effective harmonic Hamiltonians such as TDEP or SCAILD [34, 36] were not designed as reference potential for thermodynamic integration although previous studies have shown that such Hamiltonians can be used to effectively calculate accurate free energies and phonon dispersions. Due to the strong anharmonic interactions shown in Figs. 3.5a however, it is conceptually not possible to capture the correct phase space distribution by any effective harmonic Hamiltonian as indicated by the asymmetry in the right figure of Fig. 3.1a. A comprehensive list of GGA and LDA standard deviations gained for other elements by employing the quasiharmonic approximation as reference for thermodynamic integration can be found in the Appendix A.3 on page 93. A wide range of unary fcc elements (Al, Ag, Au, Cu, Ir, Ni, Pb, Pd, Pt, Rh) is considered and it is observed that Al and Cu are more harmonic in comparison to other elements which show larger anharmonic contributions and standard deviations at their melting temperature.

In the following an qualitative analysis will show that the increased standard deviation for quasiharmonic references, as shown in Fig. 3.6b, can be directly traced back to missing anharmonic flexibility of the reference potential. In a first step it is shown that the λ dependence of the anharmonic free energy directly dictates the standard deviation. It is than shown that the calculated anharmonic free energy as a function of coupling strength λ can be understood in a simple and intuitive LA picture by considering the difference of an 1D harmonic and anharmonic potential.

As a first step it is necessary to show how the energy differences, $U^{\mathrm{DFT}} - U^{\mathrm{QH}}$ between DFT and the quasiharmonic reference influence the standard deviation shown in Fig. 3.6b. To this end it
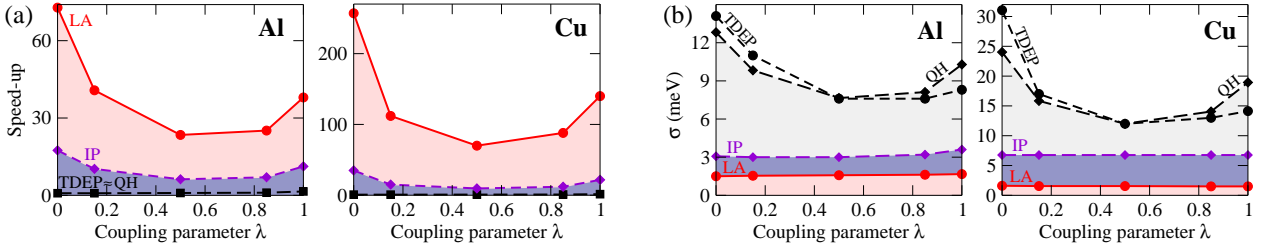
Figure 3.6: Thermodynamic integration results for Al and Cu as a function of coupling parameter λ obtained from MD runs at the respective melting temperature (for lattice constants of 4.13 and 3.75 Å). (a) Speed-up factors in comparison to the QH approximation and (b) standard deviation σ for various reference potentials: Inverse-power pair potentials (IP) [1], temperature dependent effective potentials (TDEP) [36] and *local anharmonic* (LA) approximation. The speed-up factors for fixed λ are determined by the ratio of necessary MD steps $n_{\mathrm{QH}}/n_{\mathrm{i}} = (\sigma^{\mathrm{QH}}/\sigma^{\mathrm{i}})^2$ (see also Eq. 4.5 on page 72) with standard deviations σ^{QH} and σ^{i} for the corresponding reference i=LA, IP, or TDEP. The standard deviation of the quasiharmonic reference for a wide range of fcc metals (Al, Ag, Au, Cu, Ir, Ni, Pb, Pd, Pt, Rh) is shown for LDA and GGA in the Appendix A.3.

is instructive to start with the definition of the anharmonic free energy in terms of thermodynamic integration

$$F^{\mathrm{ah}} = \int_{\lambda=0}^{\lambda=1} d\lambda \left\langle U^{\mathrm{DFT}} - U^{\mathrm{QH}} \right\rangle_\lambda, \tag{3.12}$$

where λ linearly couples the DFT and quasiharmonic system by

$$U_\lambda = \lambda U^{\mathrm{DFT}} + (1 - \lambda)U^{\mathrm{QH}} \tag{3.13}$$

and where the thermodynamic average $\langle \ldots \rangle_\lambda$ is determined by U_λ. The averages of total energy differences between DFT and the reference potential, $U^{\mathrm{DFT}} - U^{\mathrm{QH}}$ defined in Eq. (3.12), are key for the performance of any reference employed in thermodynamic integration. When performing a finite temperature MD run at fixed λ, the energy difference $U^{\mathrm{DFT}} - U^{\mathrm{QH}}$ is calculated for every time step. The thermodynamic average $\left\langle U^{\mathrm{DFT}} - U^{\mathrm{QH}} \right\rangle_\lambda$ used in Eq. (3.12) can be calculated for different coupling strengths λ and is shown for a wide range of fcc elements in Fig. 3.7(a) when employing a QH reference. In general a cotangent shaped curve can be observed with a strong λ dependence leading to averaged energies from -60 meV to 180 meV underlining the severe deficiencies of the quasiharmonic reference. The averages at fixed λ shown in Fig. 3.7a however directly dictate the standard deviation. Considering the textbook definition of the standard deviation

$$\sigma_\lambda^{\mathrm{QH}} = \sqrt{\frac{1}{N}\sum_{i=1}^{N}(x_i - \mu)^2}, \quad \text{with} \quad \mu = \frac{1}{N}\sum_{i=1}^{N}x_i, \tag{3.14}$$

and substituting every x_i by the energy difference of the MD step $U^{\mathrm{DFT}} - U^{\mathrm{QH}}$ and μ by a corresponding average $\left\langle U^{\mathrm{DFT}} - U^{\mathrm{QH}} \right\rangle_\lambda$, the λ dependence of the standard deviation shown in Fig. 3.6 is seen to scale with the magnitude of the average energy difference μ. The strong increase/decrease at small/large λ values is therefore responsible for the increased standard deviation in particular at $\lambda = 0$ and $\lambda = 1$ of Fig. 3.6.

It can furthermore be shown that also the λ dependence of average anharmonic energies $\left\langle U^{\mathrm{DFT}} - U^{\mathrm{QH}} \right\rangle_\lambda$ shown in Fig. 3.7(a) can be understood using the insights derived from the LA methodology. One can conclude from Tab. 3.1 that the first neighbor pair wise interactions are
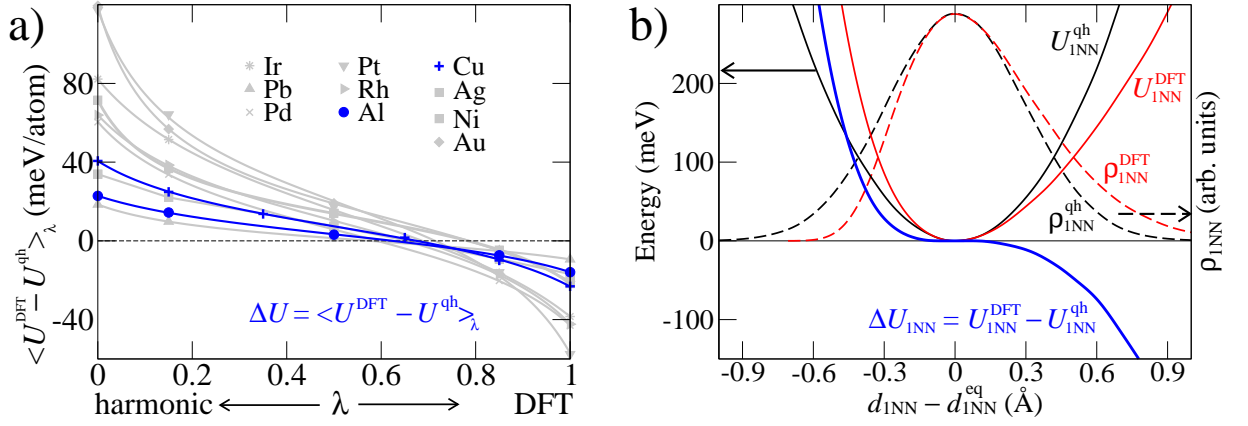
Figure 3.7: (a) λ dependence of the integrand from Eq. (3.12) at the melting temperature. (b) First nearest neighbor distribution function and corresponding effective potential for the DFT and quasiharmonic based MD runs.

mainly responsible for the vibrational contributions in fcc metals. For Tab. 3.1 exclusively these interactions were considered and were found to yield highly accurate free energies in comparison to the full solution. Consequently further neighbor effects are small. It shall be reminded that the LA potential contains implicitly the 'full' vibrational spectrum of harmonic and anharmonic contribution. For elements with negligible transversal contributions (Ag, Cu, Ir, Ni, Pb, Rh) exclusively the longitudinal first neighbor interactions are needed to accurately describe the free energy of the system. This is also seen when comparing the last two rows of Tab. 3.1: the dominant increase in speed-up is gained for the pure longitudinal potential. To capture the physics behind the λ dependence shown in Fig. 3.7a in a simple and intuitive model it therefore seems plausible to exclusively consider the mentioned longitudinal first neighbor interactions as the main reaction coordinate.

Fig. 3.7b shows a schematic similar to Fig. 3.2 where the harmonic and fully DFT computed distribution functions, ρ_{1NN}^{QH} (black dashed line) and ρ_{1NN}^{DFT} (black dashed line) are gained by corresponding MD simulations. The shown distributions are purely derived from longitudinal first neighbor distances, d_{1NN}. The gained U_{1NN}^{QH} potential (black solid line) is strictly harmonic reflecting the quadratic dependence of Eq. (2.62), whereas U_{1NN}^{DFT} (red solid line) shows a clear Morse-type anharmonic potential with a strong exponential repulsion for small distances and moderate attraction for large distances. By taking the difference $\Delta U_{1NN} = (U_{1NN}^{DFT} - U_{1NN}^{QH})$ (blue solid line) is is possible to explain the strong λ dependence of $\left\langle U^{DFT} - U^{QH} \right\rangle_\lambda$ shown in Fig. 3.7a. The two extreme cases, $\lambda = 0$ and $\lambda = 1$, can approximate by

$$\left\langle U^{DFT} - U^{QH} \right\rangle_{\lambda=0} \approx \int_{d_{1NN}} d(d_{1NN}) \, \Delta U_{1NN} \, \rho_{1NN}^{QH}, \tag{3.15}$$

$$\left\langle U^{DFT} - U^{QH} \right\rangle_{\lambda=1} \approx \int_{d_{1NN}} d(d_{1NN}) \, \Delta U_{1NN} \, \rho_{1NN}^{DFT}. \tag{3.16}$$

At $\lambda = 1$, ρ_{1NN}^{DFT} samples preferably the softer longer bonds corresponding to negative ΔU_{1NN} and resulting in negative averages $\left\langle U^{DFT} - U^{QH} \right\rangle_{\lambda=1}$ in agreement with Fig. 3.7. In contrast for $\lambda = 0$, ρ_{1NN}^{QH} samples large portions of the strongly increasing positive part of ΔU_{1NN} resulting in

large positive corrections. The behavior at other λ values can be explained in a similar manner by considering a mixed distribution function. The strongly non-linearly increasing positive part of $\Delta U_{1\text{NN}}$ which is shown in Fig. 3.7(b) will thereby dominate the integrals in Eqs. (3.15) and (3.16) explaining the positive anharmonic free energies presented in the first row of Tab. 3.1. The LA nearest neighbor picture therefore illustrates the deficiencies of a harmonic reference in comparison to the full anharmonic potential and explains qualitatively the functional dependence shown in Fig. 3.7 and the resulting standard deviations in Fig. 3.6.

3.2 Fully *ab initio* description of point defects at high temperatures

In the previous chapter a detailed investigation of the anharmonic contribution to pristine bulk thermodynamics was performed. Special emphasis was put on the *local* character of the anharmonicity. The current chapter will focus on consequences of anharmonicity for the formation of point defects. One of the main achievements of the present thesis is the formulation of the *Local Grüneisen Theory* (LGT) which allows to describe the nonlinear character of the point defect formation energy by explicitly considering the anharmonic distribution of atoms in the vicinity of defects. It is shown that the generally applied linear Arrhenius interpretation of defect formation needs to be replaced by the LGT which is able to capture non-linearities in defect formation energies as a function of temperature, an observation which is in fact often found in experiment as will be shown.

3.2.1 The Arrhenius model for defect formation

Vacancies are the most common point defects in crystalline metals and are typically found in concentrations of 10^{-3} to 10^{-4} in pure metals at their corresponding melting point [61]. For metals which melt at very high temperatures — as W, Mo and Cr — concentrations of 10^{-2} are reported [61]. Processes as self diffusion for instance are mainly mediated by vacancy type of point defects. The key quantity to characterize vacancies is their temperature dependent Gibbs energy of formation, $G^f(T)$, since it provides direct information regarding thermodynamic stability, equilibrium concentration, and solubility. In thermal equilibrium, the dilute limit concentration c for defects is related to G^f by

$$c = g \exp(-G^f/k_B T), \tag{3.17}$$

with g a geometry factor (e.g., $g = 1$ for mono- and $g = 6$ for di-vacancies in fcc) and k_B the Boltzmann constant. The current model for G^f in the vast majority of literature on point defects assumes an Arrhenius-like behavior [62–66]

$$G^f(T) = H^f - TS^f, \tag{3.18}$$

with a temperature *independent* enthalpy and entropy of formation H^f and S^f. Combining Eq. 3.17 and Eq. 3.18 the Arrhenius equation is obtained

$$c = g \exp(S^f/k_B) \exp(-H^f/k_B T) = A \exp(-H^f/k_B T), \tag{3.19}$$

which is widely used in 'Arrhenius plots'. Using this representation the concentration is plotted logarithmically as a function of inverse temperature and, assuming constant H^f and S^f, shows a strictly linear slope.

Obtaining precise values for the defect energy of formation and, in particular, for the entropy has been an outstanding challenge for both experiment and theory [67]. This is easily illustrated by using Eq. 3.18. Considering a G^f at 1000 K, an uncertainty of 0.1 eV in H^f introduces an error of already ≈ 1.2 k_B in the entropy of formation S^f. To minimize the error in experimental measurements [68], (a) vacancies must occur in concentrations well above the experimental detection limit, (b) their detection should not be shadowed by other defects or impurities, and (c) their concentration must have reached equilibrium. Particularly conditions (a) and (c) force experimentalists to go to high temperatures where concentrations are high and defect kinetics is fast. Trying to test the validity of the generally assumed Arrhenius ansatz (Eq. 3.18) is therefore a delicate task for exper-

iment due to (i) a limited resolution [69] and (ii) the mentioned restriction to high temperatures. As is seen from the example above, entropic quantities are difficult to assess experimentally. The main purpose of this chapter is therefore to theoretically investigate the temperature dependence of the defect formation energy with particular focus on its entropy dependence.

In the following it will be shown that assuming a classical harmonic theory of lattice vibrations results in a constant entropy as a function of temperature. A quantum mechanically calculated entropy converges at high temperatures to the same result — a constant entropy — in case a harmonic model is used for the bulk and defect system. The linear Arrhenius law as defined in Eq. 3.18 is therefore the necessary consequence for every (classical) harmonic model of defect formation[2]. The classical free energy for a harmonic system is defined in Eq. 2.43. Using harmonic (and therefore constant) frequencies for the bulk and the defect system, the defect formation energy becomes

$$
\begin{aligned}
F^{\mathrm{form}}(T) & = F^{\mathrm{defect}}(T) - F^{\mathrm{bulk}}(T) \\
& = k_{\mathrm{B}}T \sum_{\alpha} \ln\left[\frac{\hbar\omega_{\alpha}^{\mathrm{defect}}}{k_{\mathrm{B}}T}\right] - k_{\mathrm{B}}T \sum_{\alpha} \ln\left[\frac{\hbar\omega_{\alpha}^{\mathrm{bulk}}}{k_{\mathrm{B}}T}\right] \\
& = \underbrace{-k_{\mathrm{B}} \sum_{\alpha} \ln\left[\frac{\omega_{\alpha}^{\mathrm{bulk}}}{\omega_{\alpha}^{\mathrm{defect}}}\right]}_{\text{const.}} T
\end{aligned}
\tag{3.20}
$$

where the sum runs over all eigenfrequencies ω_{α} of the corresponding bulk and defect system. The shown temperature dependent part of defect formation in Eq. 3.20 is decreasing linearly with temperature since defect frequencies are generally softer (smaller) than bulk frequencies. The defect formation entropy, $S^{\mathrm{form}} = S^{\mathrm{defect}} - S^{\mathrm{bulk}} = -\frac{\partial F^{\mathrm{form}}(T)}{\partial T}$ is identified from Eq. 3.20

$$
S^f = k_{\mathrm{B}} \sum_{\alpha} \ln\frac{\omega_{\alpha}^{\mathrm{bulk}}}{\omega_{\alpha}^{\mathrm{defect}}} = \mathrm{const.},
\tag{3.21}
$$

for a classical harmonic system, a constant value. Using the general thermodynamic relation $\left(\frac{\partial H}{\partial T}\right) = T\left(\frac{\partial S}{\partial T}\right)$ it follows that also the enthalpy, H^f, is a constant.

Therefore, at high temperatures the classical *harmonic* theory directly leads to the generally applied *linear* Arrhenius law which assumes a *constant* entropy and enthalpy. When considering first principles investigations the harmonic approximation is state-of-the art and studies of defect formation which go beyond the harmonic picture have not received considerable attention. Furthermore it is often assumed that the vibrational entropy of defect formation is small and therefore only of secondary importance [70] which naturally supports the ansatz of constant entropy and enthalpy of formation. An example for a fully quantum mechanically calculated quasiharmonic entropy of vacancy formation for Al and Cu can be found in Fig. 4.13 on page 74 (thin orange line labeled qh+el). Despite the fact that some form of anharmonicity is included in the bulk and defect calculations — due to the volume dependence of the quasiharmonic approximation — the entropy of formation is seen to be nearly constant as a function of temperature.

Notable deviations from linear Arrhenius plots have however been observed in experimental studies of diffusion and vacancy formation. Examples for metals, in which non-Arrhenius diffusion behavior has been found include, e.g. sodium [71], potassium [72], silver [73], vanadium [74, 75],

---

[2]A quasiharmonic model is not harmonic due to volume expansion but contains anharmonic contributions to a certain degree.

zirconium [76], β-titanium [77–79] and α-zirconium [80]. Since discrepancies in S^f are in general very difficult to resolve experimentally, deviations from a linear Gibbs formation energy defined in Eq. 3.18 become most evident when different values for H^f are measured at different temperatures. For vacancy formation, a well documented non-Arrhenius behavior is known for aluminum where all high temperature measurements indicate significantly larger formation enthalpies than the low temperatures data (see Ref. [81]). The corresponding experimentally determined total entropies are about 2.4–3.12 k_B and — notably — only 0.8–1.1 k_B are considered to be due to single vacancies [64, 81, 82]. Remaining entropic contribution are assumed to stem from the presence of divacancies and the ansatz of the linear Arrhenius equation is applied for both defect species. This however is problematic, since the employed experiments measure *effective* vacancy concentrations and can not distinguish between different types of defects. Nonetheless, the existence of divacancies is necessary under the assumptions of the linear Arrhenius law. A theoretical investigation of a possible temperature dependence of defect formation parameters — like formation energies and entropies — is thus highly desirable.

An early theoretical study of vacancy formation energies which used empirical potentials showed the possible influence of anharmonic contributions [50]. Due to the limited resources and very significant inherent scatter of the results, no conclusive statements could be made at that time. The fully *ab initio* based study of vacancy formation performed in this thesis will show, (see Sec. 4.4) that the inclusion of the anharmonic contribution in fact significantly increases entropic contributions at high temperatures and that the experimentally measured effective entropy can be explained in terms of single vacancies only [68]. Attributing the full (effective) formation entropy exclusively to only one defect species disagrees however with the experimental interpretation of two involved types of defect. More importantly, the occurrence of anharmonicity would destroy the link between harmonic theory and the linear Arrhenius ansatz as stated in Eqs. 3.21 and 3.21. In order to enable a consistent interpretation of experimental measurements with anharmonic theoretical results, it is therefore desirable to formulate a theory of defect formation which is either based on or includes anharmonic contributions.

Several previous theoretical models of defect formation were derived to accurately account for entropic quantities by assuming anharmonic pair-potentials. Those attempts however concentrated on non-Arrhenius *diffusional* behavior rather than that of defect formation [67, 83] or were applied only at very low temperatures for the case of noble-gas crystals [84]. All of the mentioned works have one thing in common: By starting from anharmonic pair interactions, a non-Arrhenius behavior is derived. These results are obtained without the need to resort to other defect species and are therefore exclusively described in terms of a single defect. The underlying assumption is that the potential of the neighbor atoms close to the vacancy center becomes anharmonic and the corresponding frequencies become softer ($\omega_\alpha^{\mathrm{vac}} < \omega_\alpha^{\mathrm{bulk}}$). The suggested softening of the potential can in principle be directly investigated by performing MD simulations in a corresponding defect supercell. The attempt made here to formulate an anharmonic theory of defect formation will therefore first investigate the full potential of atoms close to a simple vacancy point defect and compare to a corresponding harmonic description in Sec. 3.2.2. Subsequently, the *local Grüneisen theory* (LGT) for defect formation will be derived in Sec. 3.2.3 and consequences for the interpretation of vacancy formation energies and in particular entropies will be shown.

3.2.2 High temperature lattice vibrations in the defect and bulk supercell

In Sec. 3.1.1 the correlated motion of atoms was investigated for bulk systems at finite temperatures. The analysis performed in this section is focused solely on the positions (coordinates) of the atoms closest to the vacancy. Due to the fcc symmetry of the investigated vacancy cell, which is shown in

Fig. 3.8a, the distribution of the vacancy neighbors can be reduced by a projection of their positions during a molecular dynamics run onto the (001) plane. The corresponding investigation will allow to qualitatively analyze the potential of atoms close to the vacancy.

It is important to consider how different models which describe the softening of phonon modes due to the presence of a defect can be realized in general. One approach was shown in Eqs. 3.21 and 3.21. There, a purely harmonic Hamiltonian was assumed for the bulk *and* the defect system to model the softening of the defect cell. It was shown that this ansatz necessarily leads to a constant enthalpy and entropy of defect formation — as assumed in the Arrhenius model. In this section and in the next section of this thesis, it will be shown that a distinctly different result is obtained when an anharmonic potential is assumed for the atoms close to the defect. To this end we follow the discussion in [68] for the first half of this section by investigating the first neighbor distribution function $\rho_{V,T}(x,y)$ of the metal atoms which are closest to the vacancy:

$$\rho_{V,T}(x,y) = \sum_i \delta\left(X^{\mathrm{NN}}_{V,T;i} - x\right) \cdot \delta\left(Y^{\mathrm{NN}}_{V,T;i} - y\right). \tag{3.22}$$

Here, the sum runs over all time steps i of a molecular dynamics run at a fixed volume V and temperature T of an fcc crystal. The $\delta(b)$ function in Eq. 3.22 is equal to 1 for $b = 0$ and otherwise 0. Further, $X^{\mathrm{NN}}_{V,T;i}$ and $Y^{\mathrm{NN}}_{V,T;i}$ are the coordinates of all first nearest neighbors of the vacancy at the ith molecular dynamics step transformed into the first quadrant of the xy-plane by proper point group symmetry operations. The corresponding xy-plane is indicated by black unit vectors in Fig. 3.8a together with the [110] equilibrium direction of the considered atom. The [110] direction represents a line through the vacancy center and the neighboring atom. Figure 3.8b shows for the example of Cu the computed distribution $\rho_{V,T}(x,y)$ for a quasiharmonic (black) and a fully DFT-based MD run (red) at the melting temperature. The QH reference potential was calculated, as in the bulk case in Sec. 3.1, by the small displacement method.

The QH and fully DFT-based distributions shown in Fig. 3.8b were for the purpose of Fig. 3.8c projected onto the [110] direction. The corresponding projection was computed by

$$\rho_{V,T}(d) = \sum_i \delta\left(\frac{1}{\sqrt{2}}\left[X^{\mathrm{NN}}_{V,T;i} + Y^{\mathrm{NN}}_{V,T;i}\right] - d\right) \tag{3.23}$$

and the result is shown in Fig. 3.8c. For both distribution functions, QH and DFT, the effective potential was constructed by

$$v^{\mathrm{eff}}_{V,T}(d) = -k_{\mathrm{B}}T \ln \rho_{V,T}(d), \tag{3.24}$$

which is also plotted in Fig. 3.8c. While the resulting quasiharmonic potential of the atoms closest to the vacancy is fully symmetric (Fig. 3.8b and c), $\rho_{V,T}$ and $v^{\mathrm{eff}}_{V,T}$ for the fully DFT-based calculation show an anisotropy along the [110] direction. This behavior can be intuitively understood by the fact that bond compression is absent towards the vacancy center and, as a consequence, the effective potential resembles a Morse-like potential which is softer. With increasing temperature the first nearest neighbors therefore access a larger part of the configuration space in comparison to the harder harmonic potential as indicated by Fig. 3.8b and Fig. 3.8c.

The large anharmonicity in the fully DFT-based potential is a direct consequence of destroying the inversion symmetry an atom has in a perfect fcc crystal: For the ideal bulk case without defect, the averaged position of the neighboring atom — and therefore its effective potential — has to be symmetric. This argument does not hold when considering the *correlated* motion of two atoms as performed in Sec. 3.1, but needs necessarily to hold when considering the average motion of a single atom in a fixed coordinate system due to symmetry considerations. The symmetry of the harmonic
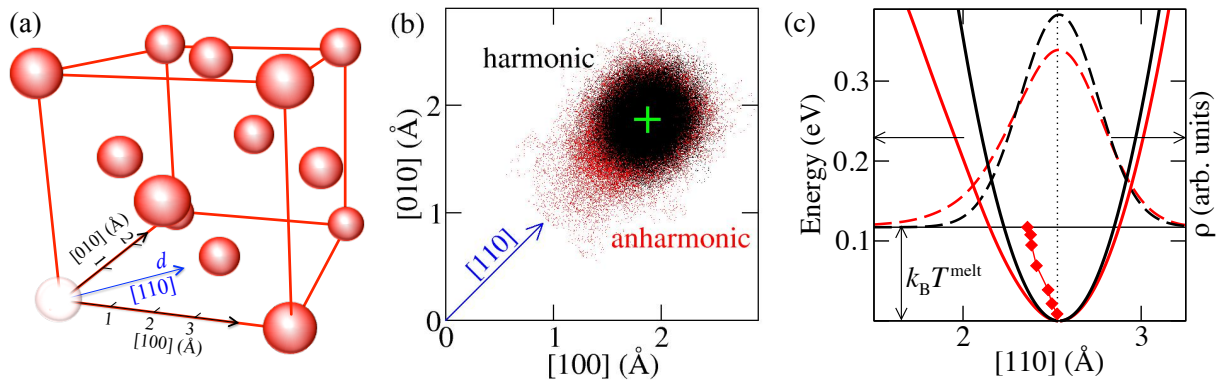
Figure 3.8: (a) Fcc crystal with vacancy at (0,0). Atomic positions of the atom in [110] direction are projected in (b) onto the indicated (x,y) plane. (b) GGA Harmonic (black) and anharmonic (red) distribution $\rho_{V,T}(x,y)$ according to Eq. 3.22 for Cu at $T^{\text{melt}} = 1360$ K for a lattice constant of 3.74Å. The vacancy center is placed at $(0,0)$ and the equilibrium position of the first-nearest neighbor is marked by a green cross. The points (black/red) show the MD trajectory of the atom at discrete time steps of 10 fs. The region close to the equilibrium position is densely populated and thus the individual points are not resolvable. The harmonic data are obtained from an MD on the harmonic potential. (c) Distribution function $\rho_{V,T}(d)$ (dashed lines) according to Eq. 3.23, i.e., projection of $\rho_{V,T}(x,y)$ onto the [110] direction indicated in (b), and corresponding effective potential according to Eq. 3.24 (solid lines). A Gauss-broadening of 0.04 Å^{-1} was used for the first neighbor distribution function. The zero line of the distribution function is shifted upwards by the energy $k_{\text{B}}T^{\text{melt}}$ according to the temperature at which $\rho_{V,T}(d)$ was calculated. The red diamonds (scaled by a factor of 10 on the [110]-axis) mark the shift of the center-of-mass of the shown anharmonic $\rho_{V,T}(d)$ at 1360 K and additionally at 250 K, 450 K, 800 K, 1100 K, 1250 K (related to the energy axis by $k_{\text{B}}T$). Fig. (b) and (c) and corresponding part of the caption are adapted from [68].

potential however cancels 3rd and higher odd order anharmonic contributions. In the supercell with the vacancy on the other hand inversion symmetry is lost and an atom near the vacancy center will experience sizable odd, in particular third order contributions as shown in the effective potential of Fig. 3.8c. The question whether the presence of the anharmonic potential on the nearest neighbor atoms close the vacancy will affect vibrations and consequently the temperature dependence of vacancy formation will be investigated in detail in the following Sec. 3.2.3.

Based on the above discussion, the largest anharmonic contributions in the defect cell should be along directions where inversion symmetry is destroyed locally. Indeed, this is found in the distribution shown in Fig. 3.8b: Odd order anharmonicity is large towards the line through the vacancy center (along [110]) but absent for directions perpendicular to the [110] direction due to the presence of a mirror symmetry. An important consequence of this finding is that the dominant collective degree of freedom is the displacement of the nearest neighbor atoms along a line through the vacancy center [68]. The effect of the vacancy on second, third and further neighbors can be observed to be small for the investigated Cu fcc crystal. Already for the bulk system discussed in Sec. 3.1.2 it has been found that anharmonic interactions are very short ranged. The same observation is made in the vacancy system for the averaged position of second and further neighbor atoms where asymmetries are seen to be small. Consequently, these contributions will effectively cancel out with the corresponding perfect bulk cell when calculating defect formation properties. It can be therefore concluded that the anharmonic potential of the nearest neighbor atoms in direction towards the vacancy center is crucial for vacancy creation — other effects as further neighbors and the directions perpendicular to the vacancy center will cancel out. Assuming however exclusively the just described anharmonic potential in one dimension to affect the defect properties, a qualitative assessment of defect formation energies can be performed by subtracting the shown (single)

anharmonic potential from a single harmonic potential. In this simplified picture, the fist neighbor potential can be equivalently used for the defect potential when considering defect formation.

So far, in Fig. 3.8, the DFT-based anharmonic potential induced by the vacancy at the melting temperature was compared to the averaged potential *for the same defect structure* obtained from the corresponding harmonic Hamiltonian. In the next step, the DFT-based anharmonic potential for the vacancy neighbor will also be compared to a fully DFT based *anharmonic* potential for the *pristine bulk* atom. The DFT MD is performed for the pristine cell at the same temperature and the same (fixed) lattice constant as used for the defect potential shown in Fig. 3.8. Due to the symmetry of the fcc crystal lattice, the distribution of atomic positions is, in average, fully symmetric and, as can be seen from Fig. 3.9, resembles an effectively harmonic potential although a DFT MD has been performed. Fig. 3.9 compares the finally obtained — and in both cases DFT-based — local potentials for the same atoms in a pristine (black) and vacancy (red) supercell. It is seen that the averaged potential for the bulk atom in Fig. 3.9 is very similar to the earlier considered *harmonic defect* potential shown in Fig. 3.8 (black). Further, the anharmonic bulk potential in Fig. 3.9 (black) is harder than the nearest neighbor defect potential (shown in red; identical to the one shown in Fig. 3.8c in red). This numerically derived result can be observed to hold for the attractive *and* the repulsive part of the potential — for displacements towards *and* away from the potential minimum.
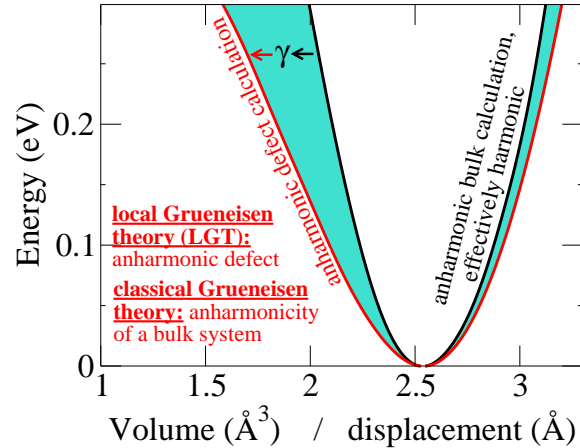

Figure 3.9: Effective potential according to Eq. 3.24 obtained from *averaged atomic positions* of fully DFT-based MD runs at the melting temperature of Cu in a pristine (black) and a defect (red) supercell. For the fully DFT-based bulk potential (black) no anharmonicity is visible due to the symmetry of the considered fcc cell as discussed in the text. The shown anharmonic potential (red) of an atom in the vicinity of the vacancy is the same potential which is shown in Fig. 3.8(c). Anharmonicity can be described in classical Grüneisen (for bulk systems) or in LGT (for a defect potential). In classical Grüneisen theory the softer part of the potential would be for larger displacements — not for smaller ones — which however only depends on the chosen vacancy neighbor and does not influence the discussion.

It has been indicated that the anharmonicity of the defect system is controlled by a collective variable, the nearest neighbor distance in the direction toward the vacancy. This formulation allows to draw a formal relation to the classical Grüneisen theory of solids [26] which describes the (quasi-) anharmonicity of an ideal bulk system with respect to a collective variable such as the lattice constant or the volume [68]. The anharmonicity in classical Grüneisen theory is described by the Grüneisen parameter γ. Instead of describing the anharmonicity of a bulk system however, the aim in the following section is to describe the anharmonicity due to the presence of the defect. The anharmonic potential, here induced by a vacancy, can be regarded as *local* (quasi-) anharmonicity — induced by the vacancy — which can be described by Grüneisen theory. The term *local* is used, since the anharmonic potential is fixed to the neighborhood of the defect whereas in classical Grüneisen theory the anharmonic potential describes the volume expansion of the bulk system

which is a collective process of many atoms and is defined for the whole crystal. Fig. 3.9 illustrates the relation between bulk and defect anharmonicity (text in red). Making such a formal connection, physical quantities which are related to the bulk collective variable in classical Grüneisen theory such as the lattice constant or the volume have to be replaced by analogous variables related to the anharmonic vacancy neighbor potential. In the following we name this new mechanism *local Grüneisen theory* (LGT).

3.2.3   Entropy of the defect

The aim of this section is to gain a qualitative model for defect formation on the ground of the preceding discussion. In the previous section it has been shown that the potential derived from averaged positions of atoms closest to the vacancy is highly anharmonic. The same averaged potential — taken from averaged positions — for a bulk system on the other hand has to be fully symmetric due to the crystal symmetry, resulting in an effectively harmonic potential. It was assumed that only the atoms in the vicinity of the defect influence the defect formation properties and that effects of further neighbors — and contributions from directions perpendicular to the vacancy center — are similar in the bulk and defect cell. Therefore, those contributions will cancel out when calculating the defect formation energy

$$F^{\mathrm{form}}(T) = F^{\mathrm{defect}}(T) - F^{\mathrm{bulk}}(T). \tag{3.25}$$

A connection was made between the (effectively harmonic) bulk and the (anharmonic) defect potential by the local Grüneisen theory which is able to describe the introduced anharmonicity by the parameter γ.

Another assumption that will be made in the following is related to the observation of an increasing volume of defect formation with temperature. The corresponding results will be presented in Sec. 4.4.4 (shown in Fig. 4.14 on page 83). There, it will be seen that with increasing temperature the volume of defect formation $v^f(T)$ is strongly increasing

$$v^f(T) = V^{\mathrm{defect}}(T) - N^{\mathrm{defect}} v^{\mathrm{bulk}}(T) = V^{\mathrm{defect}}(T) - V^{\mathrm{bulk}}(T), \tag{3.26}$$

where $V^{\mathrm{bulk}}(T)$ and $V^{\mathrm{defect}}(T)$ are the temperature dependent supercell volumes of the bulk cell (appropriately scaled) and the cell containing the defect respectively. $v^{\mathrm{bulk}}(T)$ is the temperature dependent volume of a single atom in the pristine bulk cell and N^{defect} the number of atoms in the defect supercell. To first approximation the volume expansion of both, the bulk and the defect cell, can be approximated linearly. The corresponding ansatz for both cells is

$$V^{\mathrm{bulk}}(T) = V_0^{\mathrm{bulk}} + b^{\mathrm{bulk}} T, \qquad \text{and} \qquad V^{\mathrm{defect}}(T) = V_0^{\mathrm{defect}} + b^{\mathrm{defect}} T, \tag{3.27}$$

with the $T{=}0\,\mathrm{K}$ equilibrium volumes V_0^{bulk} and V_0^{defect} and the corresponding linear expansion constants b^{bulk} and b^{defect} for the bulk and defect cell respectively. The results in Sec. 4.4.4 show an increase of the defect volume with temperature

$$v^f(T) = (V_0^{\mathrm{defect}} - V_0^{\mathrm{bulk}}) + (b^{\mathrm{defect}} - b^{\mathrm{bulk}})\, T, \tag{3.28}$$

which directly suggest

$$b^{\mathrm{defect}} > b^{\mathrm{bulk}}. \tag{3.29}$$

Based on the above assumptions, qualitative trends for the temperature dependence of defect formation will be studied in the following. In particular, the vacancy formation energy and entropy

will be investigated. While for the following derivation the classical free energy definitions will be used for simplicity, fully quantum mechanical free energies for the bulk and defect system will be shown in Fig. 3.10c to result in a very similar temperature dependence of the vacancy formation entropy. At high temperatures both free energy definitions — classical and quantum mechanical — converge by definition.

First we define the classical free energy expression (compare to Eq. 2.43) for the bulk and the defect system

$$F^{\text{bulk}}(T) = E_0^{\text{bulk}} + 3k_{\text{B}}T\ln(\frac{\omega_{\text{bulk}}}{k_{\text{B}}T}), \quad \text{and} \quad F^{\text{defect}}(T) = E_0^{\text{defect}} + 3k_{\text{B}}T\ln(\frac{\omega_{\text{defect}}}{k_{\text{B}}T}), \quad (3.30)$$

with the total energy of the corresponding bulk and defect cell, E_0^{bulk} and E_0^{defect} at $T=0\,\text{K}$. The factor 3 in Eq. 3.30 is necessary for describing a 3 dimensional system in contrast to the often found one dimensional case. The bulk and defect frequencies in Eq. 3.30, ω_{bulk} and ω_{defect}, will be described both by the Grüneisen dependence as defined in Eq. 2.56

$$\omega_{\text{bulk}}(V) = a_{\text{bulk}}V^{-\gamma_{\text{bulk}}} \qquad \text{and} \qquad \omega_{\text{defect}}(V) = a_{\text{defect}}V^{-\gamma_{\text{defect}}}, \quad (3.31)$$

with constant parameters a_{bulk}, a_{defect}, γ_{bulk} and γ_{defect}. Typical Grüneisen parameter for the bulk system (γ_{bulk}) are about 2-3 [11] while a similar order of magnitude can be expected for the — potentially softer — anharmonic local neighbor potential. Combining Eqs. 3.27 and 3.31, the average frequency of the bulk and defect system can be expressed as a function of temperature

$$\omega_{\text{bulk}}(T) = a_{\text{bulk}}(V_0^{\text{bulk}} + b^{\text{bulk}}\,T)^{-\gamma_{\text{bulk}}} \quad \text{and} \quad \omega_{\text{defect}}(T) = a_{\text{defect}}(V_0^{\text{defect}} + b^{\text{defect}}\,T)^{-\gamma_{\text{defect}}}. \quad (3.32)$$

Dropping for a moment the introduced indices for the bulk and the defect, the free energy becomes

$$F(T) = E_0 + 3k_{\text{B}}T\ln(\frac{a(V_0 + bT)^{-\gamma}}{k_{\text{B}}T}). \quad (3.33)$$

Correspondingly, the entropy can be defined (here in units of k_{B}) by

$$
\begin{aligned}
S(T) & = -\frac{\partial F(T)}{\partial T} \\
& = 3 - 3\ln\left(\frac{a}{k_{\text{B}}T}\right) + 3\gamma\left[\ln(V_0 + b\,T) + \frac{b\,T}{b\,T + V_0}\right] \\
& = 3 - 3\ln\left(\frac{\omega(T=0\,\text{K})}{k_{\text{B}}T}\right) + 3\gamma\left[2\left(\frac{b\,T}{V_0}\right) - \frac{3}{2}\left(\frac{b\,T}{V_0}\right)^2\right]
\end{aligned}
\quad (3.34)
$$

where the two terms inside the square bracket have been Taylor expanded for the final expression in Eq. 3.34. Reinserting the missing indices for the bulk and the defect in Eq. 3.34, the defect formation entropy is defined by

$$S^{\text{form}}(T) = S^{\text{defect}}(T) - S^{\text{bulk}}(T) = \left(-\frac{\partial F^{\text{defect}}(T)}{\partial T}\right) - \left(-\frac{\partial F^{\text{bulk}}(T)}{\partial T}\right)$$

$$= \underbrace{-3 \ln \left[\frac{\omega_{\text{defect}}(T=0\,\text{K})}{\omega_{\text{bulk}}(T=0\,\text{K})} \right]}_{S_0} + \underbrace{6 \left[\left(\frac{b\gamma}{V_0} \right)_{\text{defect}} - \left(\frac{b\gamma}{V_0} \right)_{\text{bulk}} \right] T}_{S'T} - \underbrace{\frac{9}{2} \left[\left(\frac{b^2 \gamma}{V_0^2} \right)_{\text{defect}} - \left(\frac{b^2 \gamma}{V_0^2} \right)_{\text{bulk}} \right] T^2}_{S''T^2} .$$
$$(3.35)$$

This formulation of entropy consists of an offset term S_0 at $T=0\,\text{K}$, a term $S'T$ which increases linearly with temperature, and the $S''T^2$ term which scales quadratically with temperature. Using the LGT analogy, the defect formation energy is described by comparing an anharmonic with an effectively harmonic potential

$$F_{\text{LGT}}^{\text{form}}(T) = F^{\text{anharmonic}}(T) - F^{\text{(effective) harmonic}}(T). \qquad (3.36)$$

It was already indicated in Eq. 3.29 that the bulk expansion coefficient b_{bulk} is expected to be smaller than the corresponding defect expansion coefficient b_{defect}. Within the LGT picture, the harmonic bulk has no expansion — due to its harmonic nature — resulting in $b_{\text{bulk}} = 0$ and $\gamma_{\text{bulk}} = 0$. This assumption results in the entropy due to LGT

$$S_{\text{LGT}}^{\text{form}} = \underbrace{-3 \ln \left[\frac{\omega_{\text{defect}}(T=0\,\text{K})}{\omega_{\text{bulk}}(T=0\,\text{K})} \right]}_{S_0 \approx 0} \qquad \underbrace{+ 6 \left(\frac{b\gamma}{V_0} \right)_{\text{defect}} T}_{S'T} \qquad \underbrace{- \frac{9}{2} \left(\frac{b^2 \gamma}{V_0^2} \right)_{\text{defect}} T^2}_{S''T^2} .$$
$$(3.37)$$

The ω_{defect} and ω_{bulk} parameters in Eq. 3.37 can be accurately assessed at $T=0\,\text{K}$ by the corresponding quasiharmonic frequencies[3]. For Al and Cu the ratio $\omega_{\text{defect}}/\omega_{\text{bulk}}$ is about 0.98, resulting in a negligible S_0 offset of $0.05 k_{\text{B}}$ at $T=0\,\text{K}$. For realistic values therefore $S_0 \approx 0$ and can be neglected.[4]

For a graphical representation of the temperature dependence of the LGT free energy and entropy of formation, it will be assumed that defect parameters for γ, b and V_0 are of a similar oder of magnitude as the corresponding bulk values. The necessary parameters are obtained by fitting to the quasiharmonic bulk properties of aluminum (which represents the anharmonicity due to the volume expansion). The harmonic bulk properties will be fitted to corresponding harmonic bulk free energies. It is noted that this ansatz is only performed to get access to qualitative values and to graphically represent the temperature dependence of the energy and entropy of defect formation due to LGT. No quantitative agreement is expected with experimentally measured defect formation properties.

The relevant harmonic and quasiharmonic bulk frequencies of aluminum as well as the corresponding bulk volume expansion are shown in Fig. 3.10(a) and (b). The quasiharmonic quantities are calculated by the small displacement method with DFT for a 32-atom pristine supercell of aluminum. The averaged frequencies shown in Fig. 3.10(a) (black dots) are used to fit the a and γ parameter in Eq. 3.31 (blue dots). The performed fit yields $\gamma = 2.2864$ and $a = 15648$ meV/Å$^{-3\gamma}$ and can be compared to the experimental Grüneisen parameter γ for Al of 2.06 [26, 85–87]. To determine approximate V_0 and b parameters for Eq. 3.27, the quasiharmonic volume expansion is plotted in Fig. 3.10(b). The performed linear fit results in V_0 and b parameters of 16.496 Å^3 and 0.0014 Å$^3/K$ respectively.

Using these parameters for the anharmonic potential in Eq. 3.36 and the corresponding harmonic

---

[3]While at elevated temperatures the reliability of the quasiharmonic approximation (QHA) is not rigorously known, the $T=0\,\text{K}$ properties can be expected to be accurately described in QHA.

[4]Using the quantum mechanical definition of the formation entropy, S_0 is strictly zero since the constituent quantum mechanical entropies are zero at $T=0\,\text{K}$, in agreement with the third law of thermodynamics.
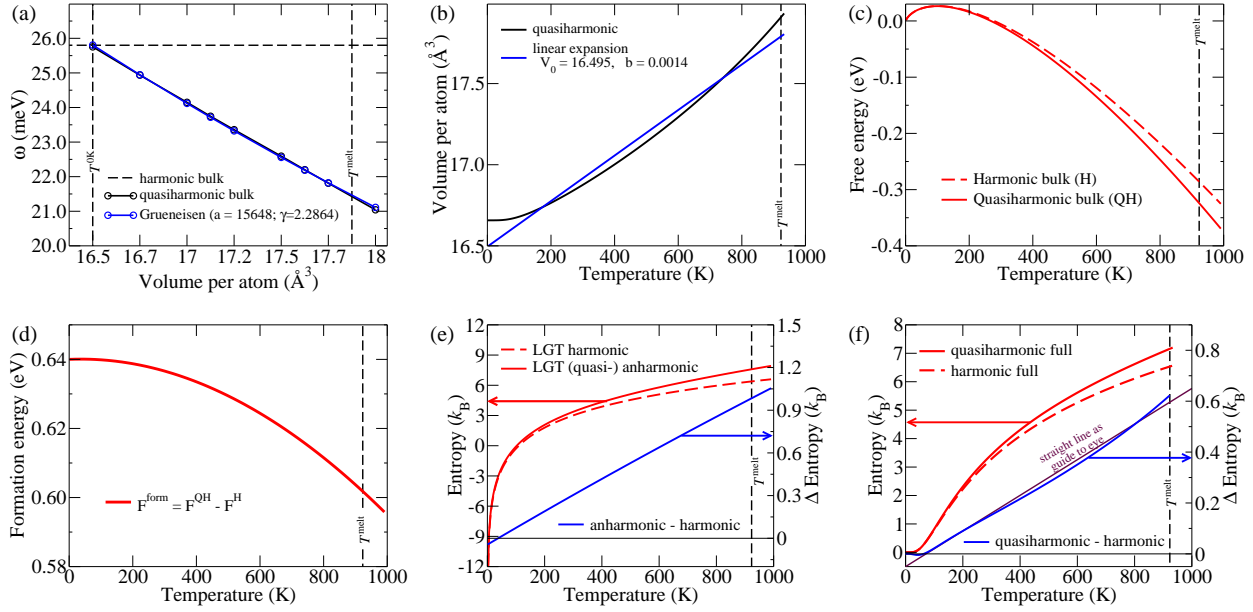
Figure 3.10: (a) Average frequencies (in meV) as a function of volume (in Å^3) for the aluminum bulk cell. The harmonic (black dashed line) and quasiharmonic frequencies (black dots and black line) are shown. The quasiharmonic frequencies are fitted by Eq. 3.31 (blue line) which results in a γ parameter of 2.29 (dimensionless) and an a parameter of 15648 in units of meV/Å$^{-3\gamma}$. (b) Quasiharmonic volume expansion for bulk Al (black). The best linear fit (blue line) yields $V_0 = 16.495$Å^3 and $b = 0.0014$Å$^3/K$. (c) Using the parameters gained in (a) and (b), the free energy in meV as a function of temperature in K is shown for the harmonic bulk with constant frequency (red dashed) and the quasiharmonic bulk (representing the anharmonic defect) (red full) as defined in Eq. 3.30. (d) Formation energy as a function of temperature derived from quasiharmonic and harmonic free energies in (c) with H_0^f of 0.64 eV exemplary. (e) Corresponding entropies to (c) (red, dashed and full) and the entropy of defect formation (blue) for the gained parameters. (f) Fully quasiharmonic entropy (including quantum effects) for bulk Al (red full) and the harmonic entropy (red dashed) for the lattice constant at $T=0$ K. Taking their difference results in an formation entropy shown in blue.

$T=0$ K frequency of 25.75 meV for the harmonic potential in Eq. 3.36 (taken from Fig. 3.10(a)), the bulk and defect free energies defined in Eq. 3.30 can be determined. Fig. 3.10(c) shows the corresponding harmonic (red dashed line) and anharmonic (red full line) functions. Both free energies are used in Fig. 3.10(d) to plot the corresponding temperature-dependent formation energy assuming $H_0^f = 0.64$ eV for Al which shows deviations from the typical linear Arrhenius law. Fig. 3.10(e) shows the corresponding harmonic and anharmonic entropies (red dashed and full lines) and the resulting entropy of defect formation (blue line) calculated by Eq. 3.37. In contrast to the generally anticipated constant formation entropy, the found entropy increases linearly with temperature. The linear S' term of Eq. 3.35 dominates while the term scaling quadratically with temperature is seen to be negligible. When the full quantum-mechanical quasiharmonic and harmonic free energies are used for Eq. 3.36 instead of the parameters gained by the fitting shown in Fig. 3.10(a) and (b), a similar result is found, which is plotted in Fig. 3.10(f) and also shows an linearly increasing entropy.

The found temperature dependence for the entropy can be compactly summarized by

$$S_{\text{LGT}}^{\text{form}}(T) \approx S'\, T \tag{3.38}$$

since the S_0 and the $S'' T^2$ terms seem to be small for typical values. This is in contrast to the constant entropy of defect formation which is found in Eq. 3.21 when assuming only a harmonic ansatz for both the defect and the bulk system.

Within the LGT assumptions the entropy of defect formation is not constant, which is the cornerstone of the generally applied Arrhenius law. The corresponding formation energies, as shown in Fig. 3.10(d), are found to be nonlinear. It is therefore possible to interpret nonlinearities found in experimental measurements of vacancy formation energies (i.e. as in Al), by an LGT form of defect formation instead of applying the linear Arrhenius model. In consequence it seems desirable to a) numerically investigate the corresponding divacancy formation energies including anharmonic contributions and b) apply the same procedure to the vacancy to be able to compare the resulting formation entropies and energies to an LGT temperature dependence. The corresponding numerical investigations will be performed in Sec. 4.4.

Chapter 4

Results: Impact of anharmonicity on the thermodynamics of selected material systems

When employing quantum-mechanically based *ab initio* approaches for the prediction of real-world materials properties such as e.g. thermodynamic phase diagrams it is crucial to not only rely on $T{=}0\,\mathrm{K}$ ground-state calculations but to take finite-temperature effects accurately into account. The necessary thermodynamic and statistical mechanics concepts have been introduced in Sec. 2. Combining these concepts with fully *ab initio* computed total energies [88, 89], it is possible to obtain a DFT level of accuracy over the whole temperature range. To this end it is necessary to calculate all relevant contributions entering the free energy surface

$$F(T,V) = E_{0\mathrm{K}(V)} + F^{\mathrm{el}}(T,V) + F^{\mathrm{qh}}(T,V) + F^{\mathrm{ah}}(T,V), \qquad (4.1)$$

fully from DFT. These contributions are the volume dependent $T{=}0\,\mathrm{K}$ energy $E_{0\mathrm{K}}(V)$ and the volume and temperature dependent electronic, quasiharmonic, and anharmonic free energy, F^{el}, F^{qh}, and F^{ah}, respectively. The computation of the first three contributions is standard and described in detail in Sec. 2.3.3 or e.g. in Ref. [11]. The computation of the anharmonic free energy which is the objective of this thesis is however still a significant computational challenge for first-principles calculations. The main reason is the fact that upon raising the temperature the phase-space that atoms can occupy exponentially increases due to atomic vibrations. Methods such as the one introduced in Sec. 3.1 enable to include the full spectrum of phonon-phonon interactions on a regular basis.

Due to the significant computational demands and resulting technical challenges only a few perfect bulk systems have been studied so far that include the full set of finite-temperature excitations based on first principles [1, 2, 9, 47]. For binary systems and defects no study has been performed on this level of theory to the best of our knowledge. Since a systematic study was not feasible so far it is presently largely unknown whether and how important anharmonicity is for an accurate description of thermodynamic properties. The quality of the widely applied quasiharmonic approximation cannot be assessed without the inclusion of all free energy contributions entering Eq. 4.1. Since temperature-dependent first principle evaluations — often performed in quasiharmonic approximation — are being applied in commercial thermodynamic databases as CALPHAD [90], investigations of the — in most cases — missing anharmonic contributions are necessary.

In Sec. 4.1 the anharmonic contribution to a wide range of fcc elements, namely Al, Ag, Au,

Cu, Ir, Pb, Pd, Pt and Rh, is investigated over the whole temperature range up to the melting point. Consequences on experimentally available quantities such as heat capacities and volume expansions are discussed. Sec. 4.2 goes beyond standard DFT approaches by presenting self-consistent calculations of thermodynamic properties of Pt, Ag and Au using the random-phase approximation up to melting. Sec. 4.3 assesses the binary Mg_2Si system including calculations on Si and Mg and draws conclusions for empirical rules such as the Neumann-Kopp rule which aim to predict temperature dependent thermodynamic quantities of alloys based on the constituents. In Sec. 4.4 the effect of the anharmonic contribution on point defect properties is investigated. In particular the vacancy and divacancy-formation energies have been calculated for Al and Cu. Applying the LGT method developed in Sec. 3.2, it is possible to consolidate all experimental vacancy formation energies and entropies of Al and Cu with *ab initio* calculated data over the whole temperature range [68]. The presented results of this thesis conclusively show that including anharmonicity is crucial to get accurate thermodynamic data, provides a significantly improved agreement to experiment [33, 91] and even changes thermodynamic quantities qualitatively [68, 92].

4.1 Fcc elements: A wide range study

The current section presents calculations of the anharmonic contribution for a wide range of fcc metals: Al, Ag, Au, Cu, Ir, Pb, Pd, Pt and Rh. Of particular interest is the volume and temperature dependence of the anharmonic contribution as well as a comparison between the performance of LDA and GGA in predicting free energies and derived quantities. In previous quasiharmonic studies it was found that GGA and LDA results yield a reliable confidence interval for *ab initio* assessments [11]. Having now the full free-energy surface including anharmonic contributions at hand, it is possible to test this empirically found error measure by comparing experimental results to the solution including the full vibrational spectrum.

In order to make a significant and meaningful distinction between harmonic and anharmonic (which is the full) contributions it is necessary to calculate the harmonic reference as accurate as possible. For all DFT calculations presented in the following the quasiharmonic free-energy surface is used as reference potential for thermodynamic integration. The QH free energies have been calculated using the small-displacement method introduced in Sec. 2.3.3 and are ensured to be converged to better than 1 meV/atom with respect to DFT related parameters and supercell sizes which were tested up to 256 atom supercells. For both considered exchange and correlation functionals, GGA and LDA, the self consistent volume range has been considered which differs significantly due to the well known overbinding of LDA and underbinding of GGA. Further details of the considered quasiharmonic volumes can be found in Fig A.2 on page 92 of the appendix.

4.1.1 Anharmonic free energy contributions in LDA and GGA

The anharmonic calculations were performed for all studied elements in a conventional 32 atom fcc cell and the free energy at the melting point was additionally tested in a 108 atomic conventional supercell[1]. Subsequently, the full Gibbs free energy as a function of volume and temperature was compared in a 108 atomic supercell for Al, Cu and Au. It is found that the anharmonic contribution of the smaller 32 atom cell is already converged to within 1 meV at the melting temperature which is understood by recalling the importance of nearest neighbor interactions found in Sec. 3.1 for the same elements. A summary of further computational details regarding the anharmonic

---

[1]Cell sizes of 256 atoms as performed for quasiharmonic assessments are usually prohibitive for anharmonic evaluations.
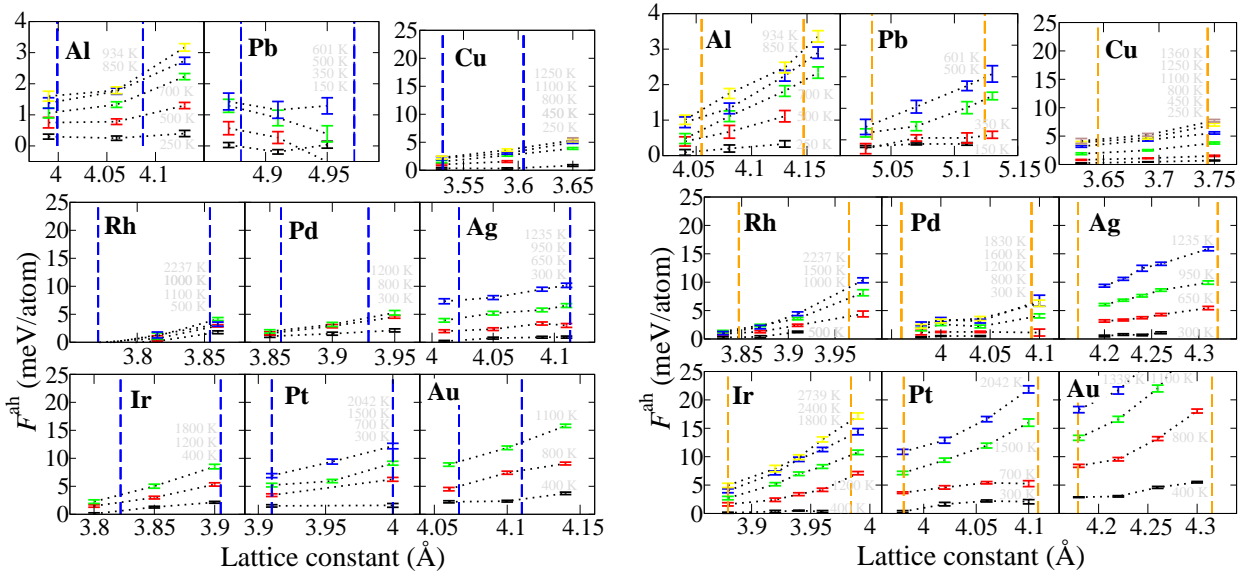
Figure 4.1: Explicit anharmonic free energy contribution F^{ah} as a function of lattice constant calculated for different temperatures (light grey) using LDA (left picture) and GGA (right picture). The energy scale is up to 25 meV for all elements but for Al and Pb where it is only up to 4 meV. Calculated statistical error margins are shown by horizontal lines. Vertical dashed lines mark the self consistently determined volume at $T=0\,$K and at the melting temperature.

calculations can be found in Ref. [33]. Besides the physical relevance of the anharmonic contribution to the thermodynamic properties, the presented results were prerequisite for assessing the quality of the derived LA methodology introduced in Sec. 3.1.

The results for the explicit anharmonic contribution to the free energy as a function of volume are shown in Fig. 4.1 for (a) LDA and (b) GGA. For both exchange-correlation functionals a positive anharmonic contribution is found for all the calculated fcc elements which leads on average to higher averaged frequencies and therefore to an effective hardening of the lattice upon inclusion of anharmonic contributions. Correspondingly the vibrational entropy increases. It can be therefore concluded that the quasiharmonic reference is too soft for *both* functionals. Taking into account that at $T=0\,$K LDA is known to overbind and usually results in too stiff lattices, this result is unexpected and has to be related to a general deficiency of the quasiharmonic approximation. This finding can be understood by considering Fig. 3.1 on page 34. At finite temperatures, the *harmonic* potential occupies positions where atoms are very close to each other. In contrast, using the *anharmonic* potential, this part of phase space is completely unaccessible for atoms due to the strong Pauli repulsion. In effect therefore, the anharmonic potential is stiffer compared to the relatively soft harmonic potential due to the strong repulsion at short distances One can therefore conclude that while LDA is too hard at $T=0\,$K, it is too soft at finite temperatures in quasiharmonic approximation of fcc metals.

An increase of the anharmonic contribution is seen for all temperatures as a function of volume. It has been found earlier [2, 10] that a linear dependence is not sufficient to describe the volume dependence of the anharmonic free energy. In fact it was pointed out in Ref. [2] that a linear dependence results in an artificial reduction of derived quantities such as the heat capacity and that the renormalized phonon frequencies which depend on volume and temperature should be used [2]. Therefore, for all results calculated in this thesis a corresponding parametrization is used which guarantees an accurate fit of the free-energy surface.

Comparing the left subfigure (for LDA) with the right one (for GGA) in Fig. 4.1 it is furthermore
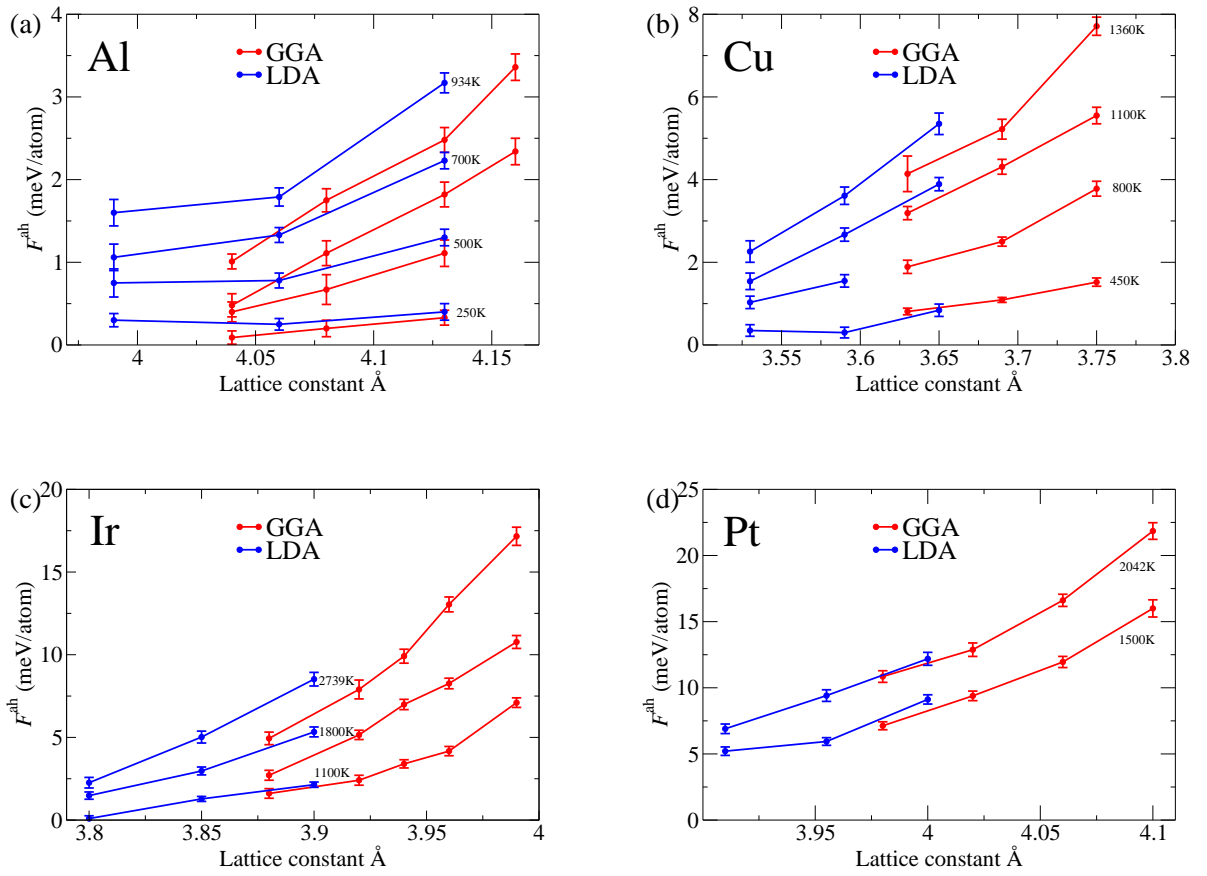
Figure 4.2: Explicit anharmonic free energy for bulk (a) Al, (b) Cu, (c) Ir and (d) Pt as a function of volume for LDA (blue) and GGA (orange). All elements are shown with an overlapping volume range. It can be observed that the explicit anharmonic free energy is dictated by the corresponding volume range to first order. Differences between LDA and GGA at fixed lattice constant are much smaller than the absolute anharmonic contribution. Elements with non overlapping volume range show a similar behavior.
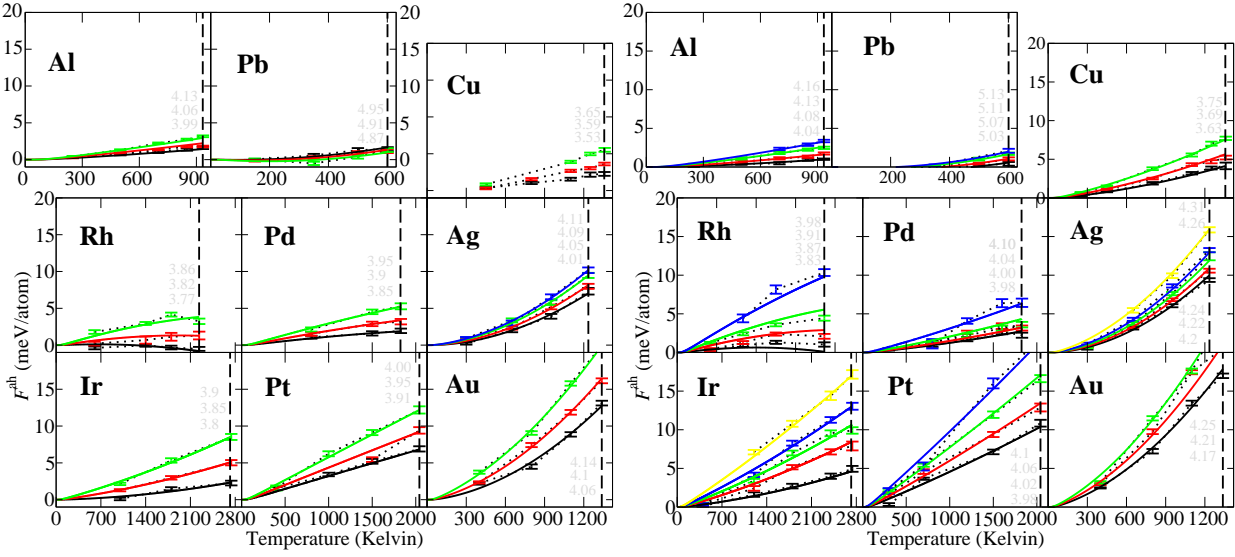
Figure 4.3: Explicit anharmonic free energy contribution F^{ah} as a function of temperature performed at different lattice constants (indicated by light gray in Angstrom) for LDA (left) and GGA (right). The dashed vertical line (black) marks the corresponding melting temperature.

apparent that the anharmonic contribution is larger for GGA than for LDA. The before-mentioned hardening will therefore be smaller for LDA than for GGA. The anharmonic contribution as a function of lattice constant is plotted for both functionals in a single plot for all elements where an overlap of calculated volumes can be observed (differences appear to the self consistently calculated volume range of LDA and GGA). The result is shown in Fig. 4.2 where an important finding of this study is revealed: to a good approximation the anharmonic contribution is not dictated by the exchange and correlation functional but is rather a function of the sampled volume range. When considering the same temperature for LDA (blue) or GGA (orange), a similar free energy correction is observed to within a few meV for all the shown elements irrespective of the used functional. A similar trend is also observed for the remaining elements with non overlapping volume range. This finding has important consequences. Since the anharmonic contribution is similar for the two investigated and very different functionals (LDA is overbinding, GGA is underbinding), it is reasonable to assume that at a fixed volume other functionals will yield very similar anharmonic contributions. Consequently, differences due to exchange and correlation effects will be small and can therefore be captured computationally very efficiently — due to the small delta in energy — by a perturbative approach. A corresponding approach is in particular very appealing for advanced functionals which are just becoming computationally feasible. Consequences of this finding are used in Sec. 4.2 to calculate finite temperature properties using the random phase approximation (RPA) over the whole temperature range up to the melting point.

The anharmonic free energy contribution as a function of temperature is shown in Fig. 4.3. It can be observed that the anharmonic contribution increases when electrons are added to the d-shell and therefore $F^{\mathrm{ah}}_{\mathrm{Rh}} < F^{\mathrm{ah}}_{\mathrm{Pd}} < F^{\mathrm{ah}}_{\mathrm{Ag}}$ and $F^{\mathrm{ah}}_{\mathrm{Ir}} < F^{\mathrm{ah}}_{\mathrm{Pt}} < F^{\mathrm{ah}}_{\mathrm{Au}}$. This observation is consistent with the strong anharmonic behavior known for solid rare (inert) gas crystals [37, 93, 94] which have a filled shell, and is also in line with the relative weak anharmonic contribution found in Al and Pb which have an unfilled p-shell. Also, when increasing the principal quantum number in the same group (period) of the table of elements, the anharmonic contribution is seen to increase and therefore $F^{\mathrm{ah}}_{\mathrm{Cu}} < F^{\mathrm{ah}}_{\mathrm{Ag}} < F^{\mathrm{ah}}_{\mathrm{Au}}$ which is also found for the other groups. It can be observed that the anharmonic contribution as a function of temperature may show a convex or concave (for Rh, Pd, Ir and Pt)

shape and for a correct description needs to be fitted by a curvature which goes beyond second order. When studying anharmonic contributions, largest effects are to be anticipated at highest temperatures and volumes.

4.1.2 Effects on derived quantities: Heat Capacity, Expansion

We now turn to the comparison of our DFT results to the derived quantities of the free energy surface. While $F(V,T)$ cannot be measured directly by experiment as was elaborated in Sec. 2.4.2, derived quantities such as the heat capacity or the volume expansion are accessible experimentally and will therefore be compared to the calculated results. Fig. 4.4(a) shows the isobaric heat capacity, which is a second derivative of the Gibbs free energy (see Eq. (2.3)) and therefore a very sensitive measure, for all studied elements. LDA results are shown in blue and GGA in red. The dotted lines are the results including quasiharmonic and electronic contributions while the full line is the final result additionally including anharmonic contributions. Up to room temperature the investigated fcc elements show a remarkable agreement already in quasiharmonic approximation with the experiment (black symbols) and the CALPHAD reference [6] shown by the black line. With increasing temperature the quasiharmonic heat capacity, in particular for GGA clearly overestimates in comparison to experiment for Pd, Ag, Pt, Au. Including anharmonicity decreases the heat capacity for all the studied elements and for both considered functionals. It can be thus deduced that the QH approximation consistently overestimates the final, and self consistent heat capacity of fcc metals.

The magnitude of the anharmonic correction to the heat capacity is consistent with the trend shown in Fig. 4.3: while the correction is small for Rh, Pd and Ir (about 0.1-0.4 k_{B}), it substantially increases when the d-shells are being filled or when the principal quantum number (period) is increased in the table of elements. For GGA the correction to C_P is in general larger than for LDA. When neglecting the divergence for GGA Au, corrections of up to $1.4k_{\mathrm{B}}$ are found for GGA while the largest LDA correction is $1.2k_{\mathrm{B}}$. Since it is generally anticipated that fcc elements are only weakly anharmonic, this finding is surprising.

It was found that the divergence observed for GGA Au can be fully cured upon inclusion of $T{=}0\,\mathrm{K}$ non-local many-body effects and additional anharmonic contributions at high temperatures [124]. While Fig. 4.4 shows that LDA is very accurate for describing the heat capacity of Au, it is also found to underestimate the heat capacity — when comparing to the recommended CALPHAD data — for elements such as Ir and Rh where anharmonic effects are small. It is important to note that neither GGA nor LDA seem to consistently yield reliable results for all the investigated elements. It will therefore be important to analyze the performance of both functionals to yield a reliable confidence interval for theoretical calculations which has been proposed based on quasiharmonic assessments [10].

The anharmonic contribution to the heat capacity in Fig. 4.4 is found to be larger for GGA than for LDA. This is directly related to the sampled volume range which is smaller/larger than the experimental volume for LDA/GGA and was elaborated in the discussion of Fig. 4.2. The quasiharmonic GGA heat capacity is however larger for all the shown elements and the inclusion of anharmonic contributions results in a significantly reduced discrepancy between LDA and GGA at the melting point. It thus appears that the quasiharmonic approximation 'amplifies' the intrinsic errors inherent to the specific xc functional while including anharmonicity reduces them.

On the basis of quasiharmonic heat capacity calculations, LDA and GGA were found to systematically provide a reliable *ab initio* confidence interval with respect to experiment [10]. Upon inclusion of anharmonic contributions the difference between LDA and GGA — the thus proposed error margins — are observed to decrease. This improved confidence interval is especially pro-
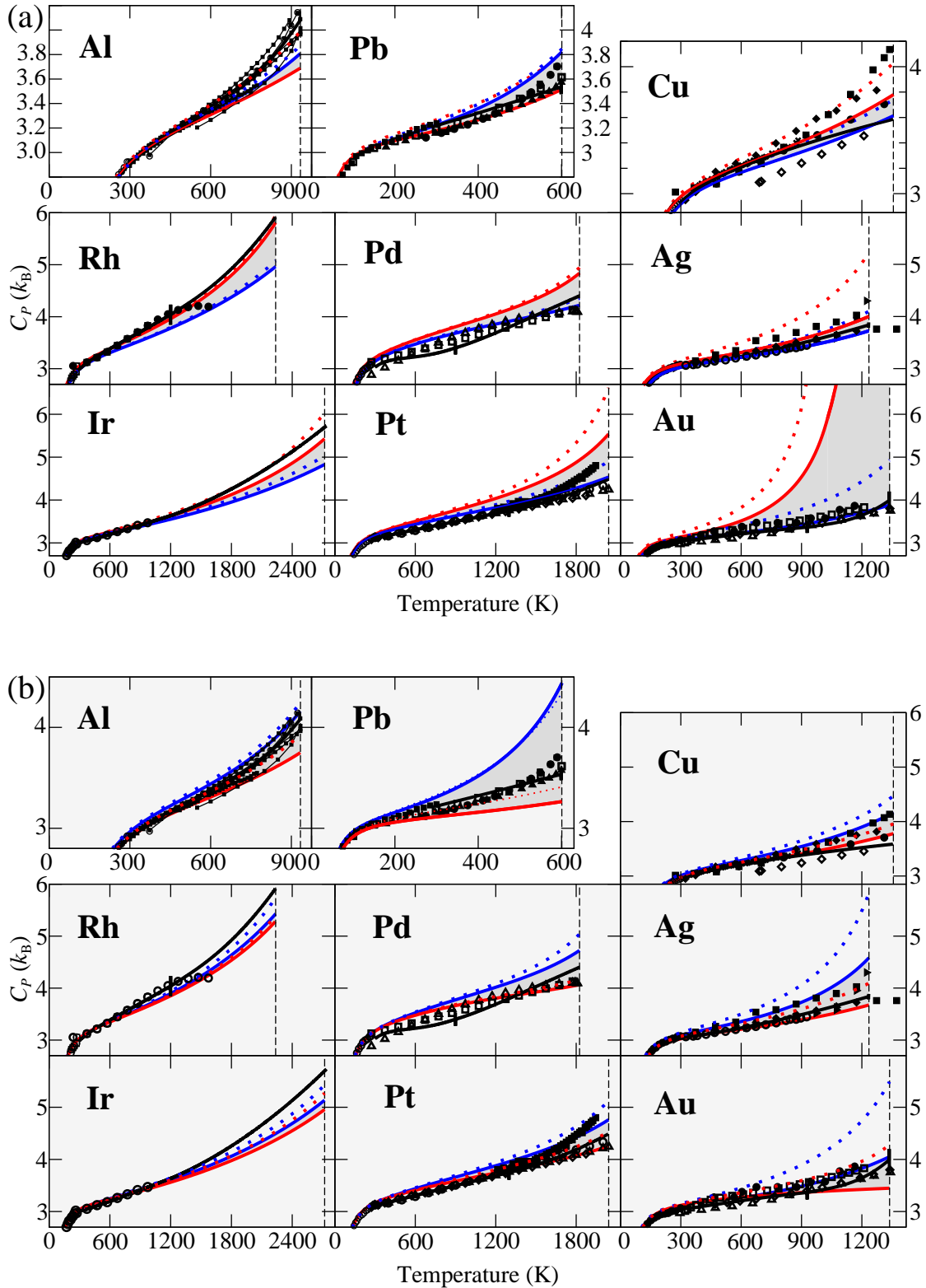
Figure 4.4: Isobaric heat capacity in units of the Boltzmann constant, k_{B}, as a function of temperature. The quasiharmonic plus electronic (dotted) and the full solution including anharmonic contributions (full line) is shown for LDA (blue) and GGA (red). In (a) the self consistent solution is shown whereas (b) shows the mixed approach where the $T=0\,\mathrm{K}$ contribution is taken from experiment. The black line is the CALPHAD Dinsdale evaluation from Ref. [6]. Experimental measurements are shown by full and empty symbols (black) and are taken from following references: Al [95–102], Pb [95, 103–105], Cu [106–112], Rh [105, 113], Pd [105], Ag [113–117], Ir [105], Pt [118–121], Au [105, 122, 123].

nounced in Pt and Ag. For Pb, the one element where the confidence interval increases, this turns out to be a favorable circumstance since in quasiharmonic approximation the experimental results were overestimated by both functionals. Further it can be observed that for five of the elements, Pb, Cu, Ag, Pt and Au, the quasiharmonic LDA and GGA results do not enclose the reliable and recommended CALPHAD SGTE heat capacity [6]. Only upon inclusion of the anharmonic contribution the recommended C_P curve is, for all the calculated elements, either enclosed or very close. From Fig. 4.2 it is therefore evident that at elevated temperatures anharmonic contributions are crucial for a quantitative description. For several of the investigated elements in Fig. 4.4, Al, Pb, Cu, Ag and Pt, the anharmonic contribution — which is the difference between the dotted and full line — is similar or even more significant than the error introduced by the exchange correlation functional (indicated by the gray shaded area). In the spirit of a full *ab initio* prediction of finite temperature properties this provides a strong argument to include anharmonicity in future calculations.

Near the melting point, corrections to the here presented heat capacities are expected due to vacancy point defect contributions [2, 33]. These positive contributions to the heat capacities were found however — also in the framework of this PhD thesis — to be small. For Al and Cu they were calculated to be 0.1 k_B [125] and can be therefore safely neglected in the following discussion. Since the investigated materials are non magnetic, Fig. 4.4(a) contains all relevant finite temperature excitations and can be regarded as a final result. Remaining discrepancies therefore have to be attributed to the exchange and correlation functional.

A method to test the inherent error introduced by the functional at $T=0\,\mathrm{K}$ is the 'mixed approach' [10] where the experimental bulk modulus and its derivative together with the experimental volume are used at $T=0\,\mathrm{K}$ instead of the self consistent values of the corresponding functional. Corresponding calculations have been performed and are shown in Fig. 4.4(b). It is directly evident that using the correct $T=0\,\mathrm{K}$ data, the divergence for the heat capacity of Au is lifted. Therefore the GGA evaluations become a lower bound and LDA an upper bound to experiment. In general, both functionals represent a convincing confidence interval for all the investigated elements. The agreement is significantly improved at high temperatures compared to a purely quasiharmonic assessment. The anharmonic correction is reduced for GGA in the 'mixed approach' in comparison to self-consistent calculations. This can be once again traced back to the volume dependence of anharmonic contributions. When using the mixed approach with GGA, smaller volumes are sampled compared to the self-consistent GGA volumes. This results in smaller anharmonic contributions in GGA. An overcorrection due to the lower bound of the quasiharmonic GGA results is therefore not observed with respect to experiment. The same argumentation explains the increase of the anharmonic contribution that is found when using LDA with the 'mixed approach'.

Fig. 4.5 shows the relative expansion of the lattice constant as a function of temperature. In the upper figure (a) the self consistent volume, bulk modulus and its derivative at $T=0\,\mathrm{K}$ have been used whereas in (b) the 'mixed approach' is applied as explained above. The effect of the anharmonic contribution becomes more pronounced, as for the heat capacity, when increasing the period and filling the d-shell. Using the quasiharmonic plus electronic approximation only, experimental expansion is not captured in the spirit of the GGA/LDA confidence interval for Pt and Au. Including anharmonic contributions improves this situation and all elements are found between the final self consistently calculated expansions. Employing the mixed approach which is presented in Fig. 4.5(b), the confidence interval shrinks but experimental measurements are still correctly contained within the now smaller error margins.

In order to compare the influence of the different contributions (electronic, quasiharmonic and anharmonic), Fig. 4.6(a) summarizes the heat capacity for all elements using the GGA functional.
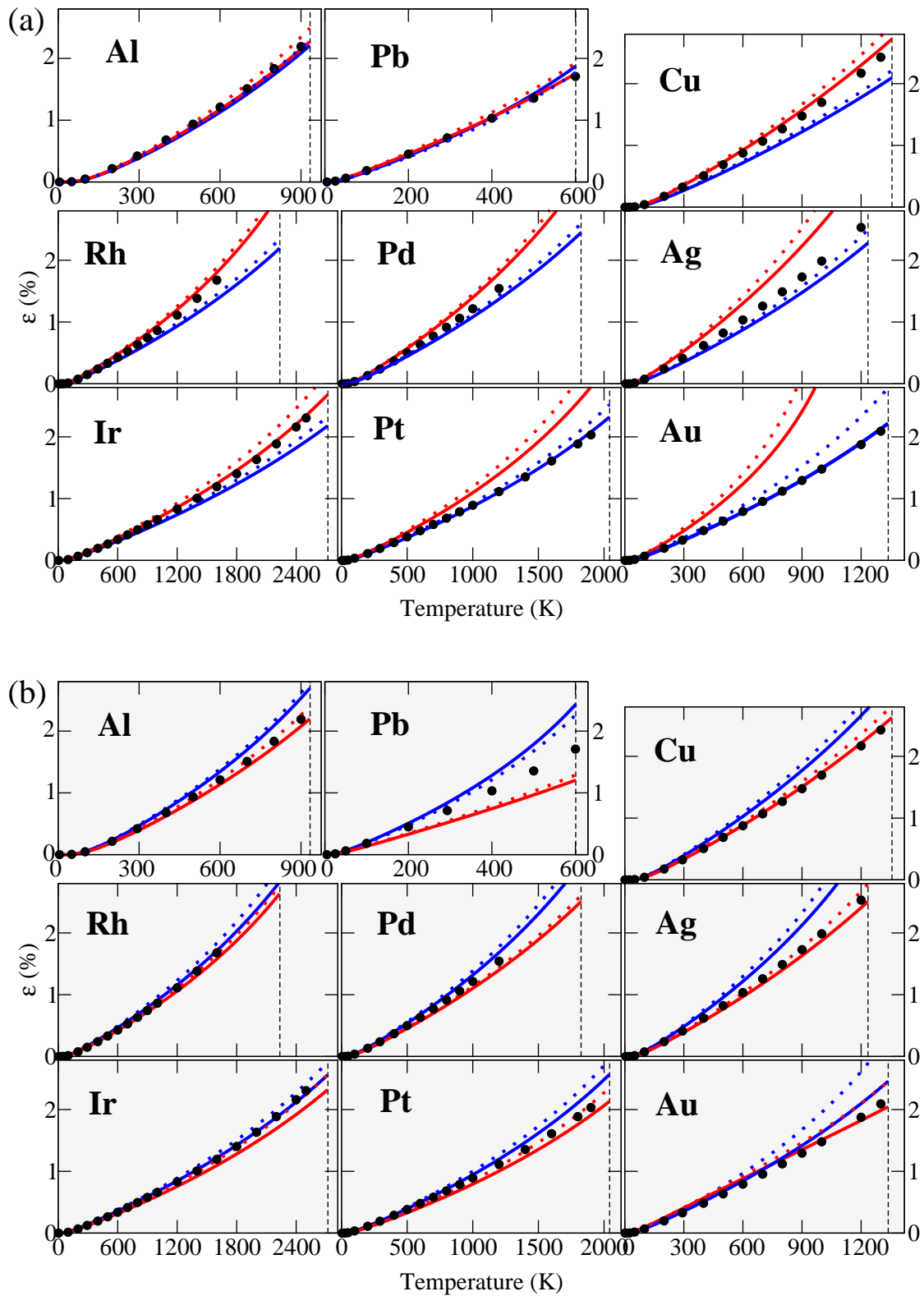
Figure 4.5: Relative expansion of the lattice constant as a function of temperature. (a) Self consistent and (b) solution using the 'mixed approach'. Results for GGA (red) and LDA (blue) are shown in quasiharmonic plus electronic approximation (dotted) and additionally including anharmonicity (full lines).
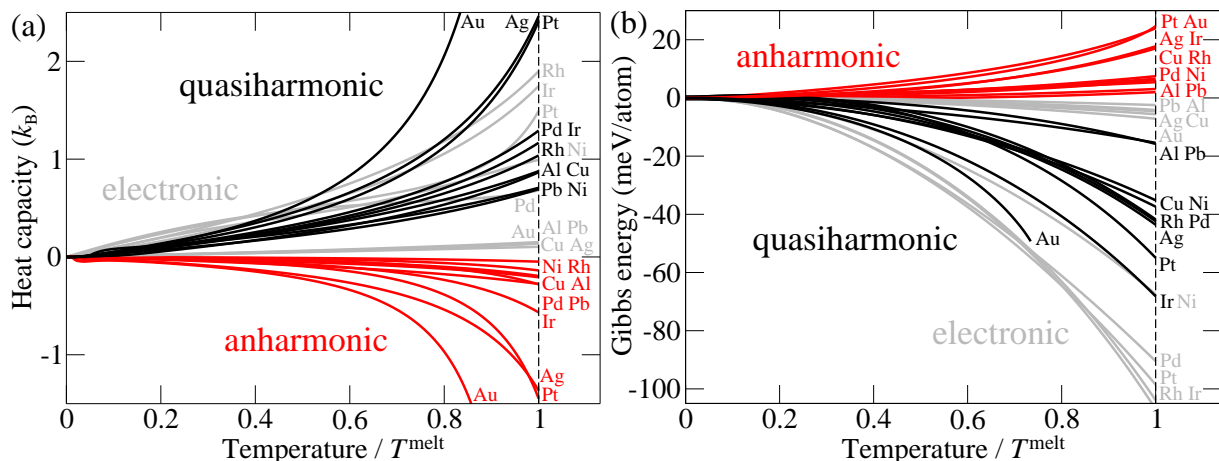
Figure 4.6: Comparison of quasiharmonic, electronic and anharmonic contributions in GGA to (a) the heat capacity and (b) the Gibbs energy as a function of homologous temperature. The qh data represent only the contribution beyond the purely harmonic part. Figure and caption were adapted from [33].

The displayed quasiharmonic contribution shows merely the part due to thermal expansion. It is directly evident that all three contributions are roughly of the same order of magnitude and are of equal importance. An attempt to model any of the studied elements without the inclusion of all excitations would therefore lead to an altered quantitative description and modify the final result. It can be seen that the quasiharmonic heat capacity is consistently positive, whereas, as shown before, the anharmonic one is throughout negative for the investigated fcc materials. The current practice to include only quasiharmonic contributions (sometimes additionally electronic contributions) is therefore insufficient since anharmonic effects show a similar magnitude and should not be neglected. Fig. 4.6(b) shows the Gibbs energies corresponding to the previous figure. In general it can be observed that the anharmonic free energies are roughly half the magnitude of the quasiharmonic contribution and electronic contributions are most significant. All these energies can easily modify phase transition temperatures and need therefore to be considered, e.g., in phase diagram calculations.

4.2 Beyond standard DFT: RPA up to melting

The previous section 4.1 has shown the capabilities and limitations of standard exchange-correlation functionals to describe finite temperature thermodynamic material properties. It has been unveiled in Fig. 4.4(a), that self consistent GGA calculations for Au show a divergence in C_{P}. Anharmonic contributions were found to push this divergence to higher temperatures but could not solve this deficiency of GGA in a self consistent manner. At $T=0\,\mathrm{K}$, the shortcomings of standard functionals are well-known. The 'mixed approach' was introduced as a possible solution which uses experimentally measured data at $T=0\,\mathrm{K}$ with finite temperature phonon-phonon vibrational contributions calculated by *ab initio*. It was shown that the $T=0\,\mathrm{K}$ error significantly influences finite temperature results. For systems where no experimental measurements have been performed such an approach will in general not be feasible. More important is however that *a priori* it is unclear to which extent the $T=0\,\mathrm{K}$ parameters influence the finite temperature phase-space sampling by coupling to vibrational contributions. In view of the limitations of the standard functionals an approach seems highly desirable which applies advanced functionals self consistently over the

whole temperature range. Hybrid functionals, e.g. Heyd-Scuseria-Ernzerhof (HSE), are a possible improvement since they introduce exact exchange. The correct amount of exact exchange however is not rigorously defined and has therefore to be adjusted to experimental measurements [126]. A promising route which goes beyond hybrid functionals is to include non-local many-body effects to the correlation energy. Following this route, the random phase approximation (RPA) has been developed and has been successfully applied at $T=0\,$K to many systems [127–129].
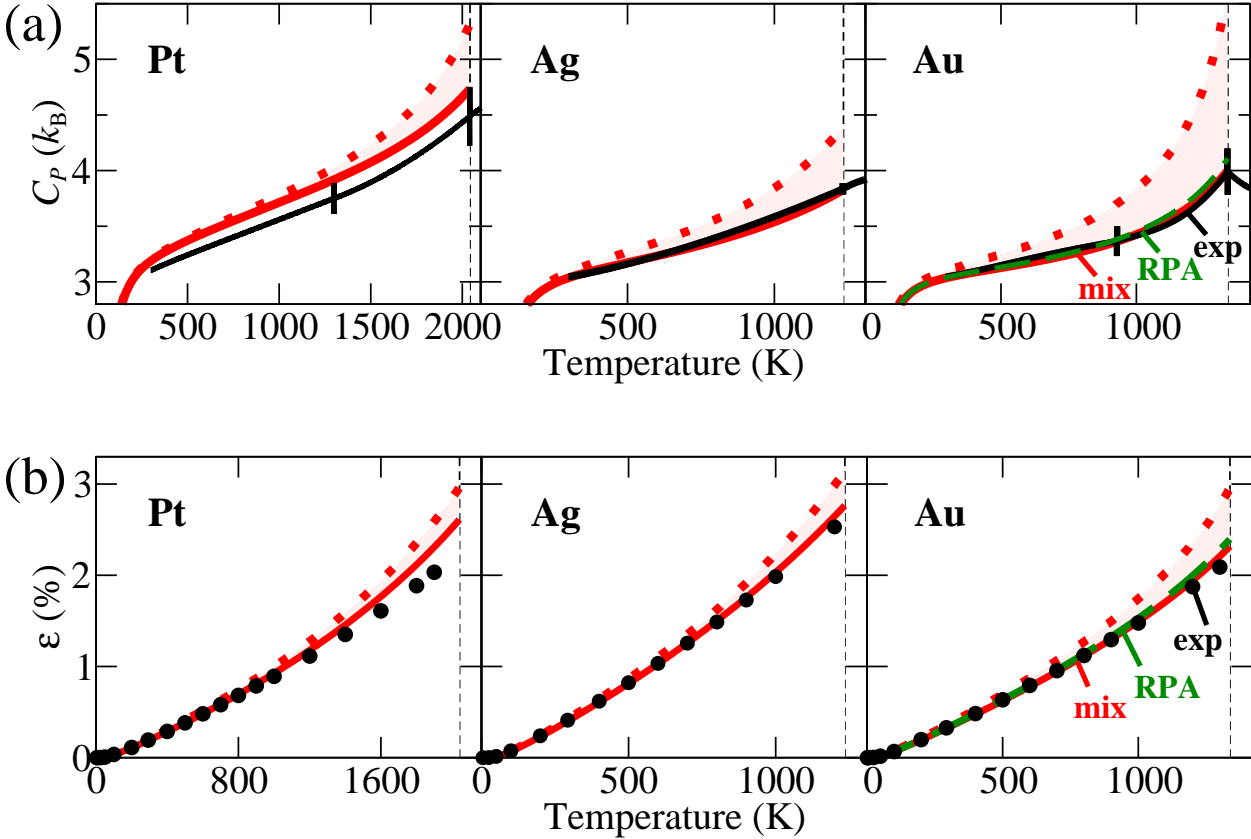

Figure 4.7: (a) Isobaric heat capacity and (b) linear thermal expansion as a function of temperature. The red dotted line corresponds to the quasiharmonic plus electronic contribution mixed with RPA at $T=0\,$K. The full line (red) additionally contains the GGA anharmonic contribution. The full RPA calculation was only performed for Gold and is shown by the dashed line (green). The error when neglecting the coupling of the $T=0\,$K contribution to finite temperature vibrational properties — the difference between the dashed green line and the full red line — is small. The red shaded area is the anharmonic contribution to the final result. Experimental values (black) are taken in (a) from Ref. [105] and in (b) from Ref. [6].

While advanced functionals calculations recently became feasible at $T=0\,$K, the calculation of finite temperatures free energies is currently out of reach on a similar level of accuracy due to significant computational demands. In Sec. 4.1 it was however found that the computationally most challenging finite temperature mechanism — anharmonic phonon-phonon interactions — are very similar in magnitude for different functionals. Corresponding contributions are therefore expected to be also similar in magnitude for advanced functionals. For this reason, perturbative approaches as the UP-TILD method can be applied by first performing the phase-space sampling on a GGA or LDA level and consequently calculating the correction to the anharmonic free energy by the advanced functional. This suggested two-step procedure decouples the computationally

demanding calculation of accurate *ab initio* free energies from the phase space sampling of atomic vibrations. Since non-local many-body effects have been shown to significantly influence the self-consistent volume of Au at $T=0\,\text{K}$ [129], the above elaborated procedure has been recently applied for the calculation of thermodynamic properties of Au to a RPA level of accuracy over the whole temperature range [124]. Out of all investigated elements in Sec. 4.1, Au has been revealed to contribute the most significant anharmonic free-energy contribution (see Fig. 4.1 on page 58). The effects of non local many-body effects as e.g. van-de-Waals interactions, which might also change the finite temperature anharmonic contribution has to be investigated.

The procedure for a finite temperature RPA treatment of Au is performed in the following way: The $E_{0\text{K}}$ contribution is calculated fully by RPA while the finite temperature atomic vibrations are sampled in a first step in the GGA approximation. In the final step, several of the sampled finite temperature GGA snapshots are recalculated by RPA and the UP-TILD approach. The energy difference between the GGA and RPA energies shows a rapid convergence since, as expected, the correction from GGA to the RPA anharmonic contribution turns out to be very small. The resulting averaged difference amounts to only 3 meV at melting. For other elements which show an even smaller anharmonic contribution, the correction due to RPA at finite temperatures is therefore expected to be even smaller. It was demonstrated that a perturbative approach is well suited for the calculation of — otherwise unaccessible — anharmonic contributions on a fully RPA level of accuracy. Using the fully RPA derived free energy for Au and additional anharmonic contributions, the divergence in the GGA heat capacity was eliminated in a self consistent manner [124].

Fig. 4.7(a) and (b) show the heat capacity and the relative expansion of the lattice constant as a function of temperature for Pt, Ag and Au. The performed $T=0\,\text{K}$ RPA calculations have been coupled with finite temperature GGA data introduced in Sec. 4.1. The dotted lines (red) are the quasiharmonic plus electronic GGA results where the $T=0\,\text{K}$ contribution has been calculated with RPA. The full line (red) contains additionally anharmonic contributions. Only for Au the full finite temperature coupling form GGA to RPA has been calculated and amounts to 3 meV at melting [124]. The fully self consistent RPA result is shown by the dashed line (green). For Pt and Ag no effects of the coupling is expected due to the already mentioned smaller anharmonic magnitude in comparison to Au. For C_P and ϵ in Fig. 4.7(a) and (b) effects of the anharmonic correction at finite temperatures are seen in all cases to yield the necessary contribution to reach a very good agreement with experiment. The maximum deviation from the experimentally found C_P is only 0.2 k_B when considering the whole temperature range.

4.3 Binary systems: From Mg and Si to Mg$_2$Si

Mg$_2$Si has been recognized as a promising thermoelectric material for the conversion of heat at temperature ranges from 500 K to 800 K [130–132]. It is non-toxic and, importantly, consists of abundant constituents, Mg and Si. One of the widely applied commercial alloys is the Al-Mg-Si system which is in particular used for lightweight applications. The stability of this alloy system is essentially dictated by the stability of Mg$_2$Si [91]. While the corresponding phase diagram of the Mg-Si system is well known, the thermodynamic properties of the single stable compound in this system, Mg$_2$Si, provides a considerable challenge for experimental measurements. Though its melting temperature is about 1346 K, very recent and previous attempts to measure its heat capacity beyond temperatures of 793 K failed [91, 133]. In view of this significant experimental challenge, the here presented methodology for the calculation fully *ab initio* based heat capacities including all finite-temperature excitations is highly desirable. Quasiharmonic plus electronic calculations for this material system were published during the PhD period; the corresponding computational

details, performed convergence checks, comparison to experiment and various computed results can be found in Ref. [91]. Here, the missing anharmonic contributions were calculated for Si, Mg and Mg$_2$Si and their effects on the heat capacity are presented below.

The thermodynamic integration calculations have been performed from the calculated quasiharmonic references used in Ref. [91]. All anharmonic free energies have been converged to a standard error of better than 0.5 meV for the three structures. For Si, supercells containing 64 and 216 atoms were tested of which the smaller cell converged to better than 1 meV in the anharmonic free energy at melting. For Mg and Mg$_2$Si, 36 and 96 atom supercells have been used. For Si, Mg and Mg$_2$Si cutoffs of 400 eV, 400 eV and 500 eV respectively have been found to be sufficient. The converged k-point grids for the highly converged UP-TILD calculations were 4^3 for the semiconducting Si and Mg$_2$Si while a 6^3 grid was used for the metal Mg.

An important finding for the material system of Si, Mg and Mg$_2$Si is that the final free energies calculated in GGA and LDA are very close to each other up to the melting temperature. This is consistently found for all of the three structures, for all the calculated excitations and is also observed for the finally obtained thermodynamic properties which are very similar for GGA and LDA. Following the discussion in Sec. 4.1 this corresponds to a very narrow *ab initio* confidence interval. The anharmonic contribution to the free energy at the melting temperature in silicon is 20 meV for GGA and LDA. The difference of the total free energy at the melting temperature between LDA and GGA — which is the sum of $T=0$ K, electronic and anharmonic contributions — is, on the other hand, only 1.5 meV. The anharmonic contribution is therefore significantly higher than the error due to exchange and correlation. Fig. 4.8(a) shows the heat capacity of Si as a function of temperature. It can be observed that the quasiharmonic contribution beyond the purely harmonic part is very small in Si (green shaded region labelled 'expansion'). This is well understood by the small expansion of Si in comparison to the fcc metals presented in Sec. 4.1. Due to the semiconducting nature of Si, the electronic contribution is also negligible. Anharmonic contributions turn out to be crucial for C_P. Without them, a quantitative description is not possible for Si. Including anharmonicity (red shaded area) significantly reduces the discrepancy between theory and experiment and brings the final C_P very close to the CALPHAD assessment. The blue and orange arrow at the melting point shown in Fig. 4.8(a) indicate the very close final C_P for GGA and LDA. On the basis of the calculated results and previously performed measurements, the most recent experimental data for silicon performed by Yamaguchi (grey triangles) seem questionable. The remarkable agreement for LDA and GGA for C_P to the CALPHAD assessments was already mentioned. The likely very similar Gibbs free energy of LDA and GGA deviates however from the SGTE CALPHAD assessment at ambient pressure and was found to be lower for both functionals by 20 meV at melting in comparison. In contrast to the assessed fcc elements (see Sec. 4.1), Si shows a negative anharmonic contribution which results in the shown *positive* correction to the heat capacity. The assumption that anharmonicity yields similar trends and corrections across the periodic table of elements — an assumption which could have been drawn from the wide range fcc study in Sec. 4.1 — has therefore to be dropped.

Fig. 4.8(b) shows the heat capacity contributions for Mg. As in the case of Si, the final total Gibbs free energies are very similar for GGA and LDA and show only a small difference of about 5 meV at melting. The anharmonic contribution is greater than 3 meV at melting and therefore in the same order of magnitude as the error due to the functional. Though hcp Mg is close packed and thus similar in structure to the investigated fcc elements in Sec. 4.1, the anharmonic free energy contribution is negative and of opposite sign to the fcc elements (same sign as Si). Due to the small 5 meV difference in the final free energy between LDA and GGA, small DFT error margins are expected for Mg. Indeed, the final heat capacity is very well described by both functionals.
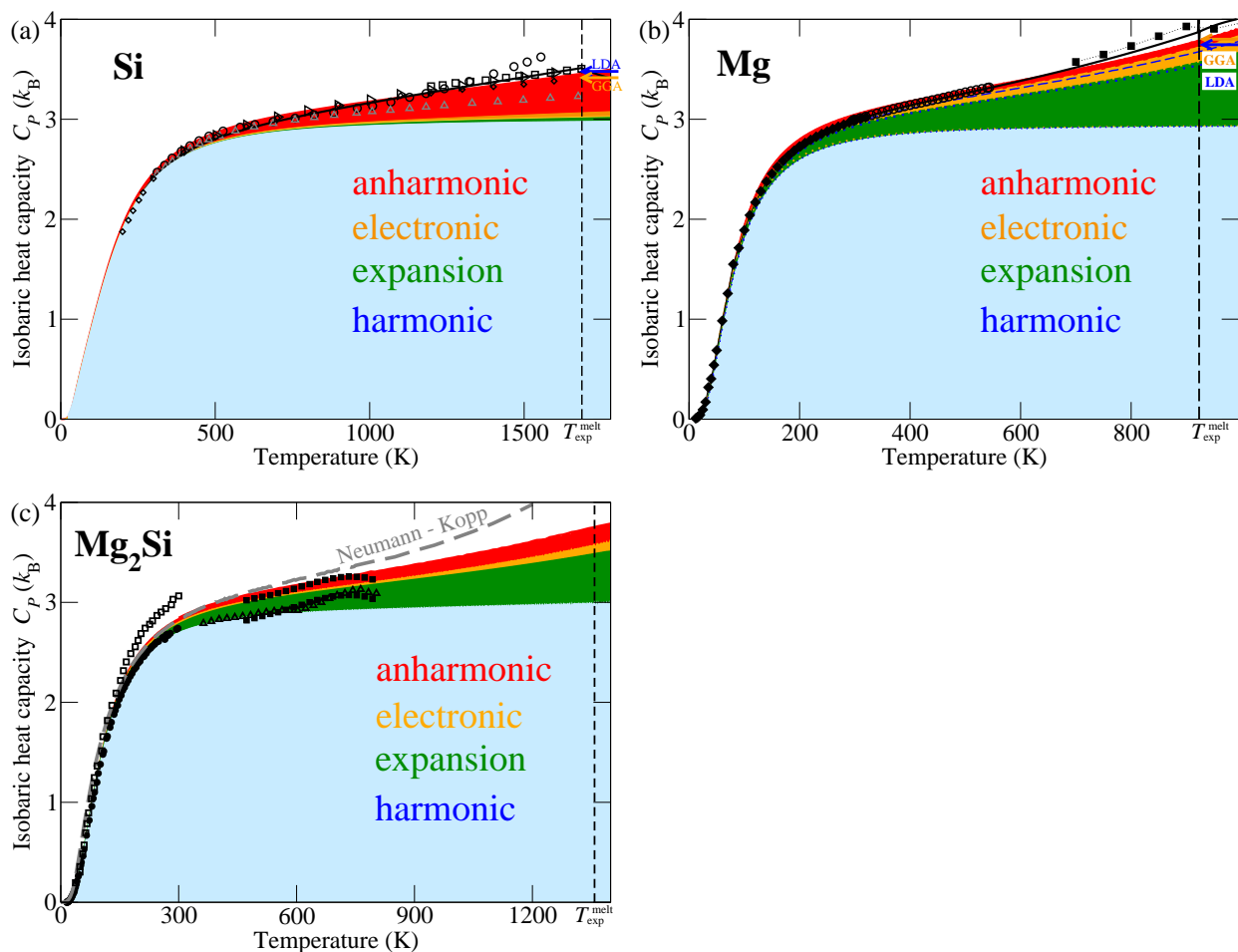
Figure 4.8: Isobaric heat capacity as a function of temperature for (a) Si, (b) Mg and (c) Mg$_2$Si. Different colors are used for the different contributions: harmonic (blue), expansion (green), electronic (yellow) and anharmonic (red). The blue (LDA) and yellow (GGA) arrows indicate the very small difference between both applied functionals for the finally obtained C_P. The very small difference can be observed for all contributions and all three systems and was found in other *ab initio* assessments to provide a confidence interval for experiment. Experimental data (black symbols) are taken from: Si [134–138], Mg [139–142], Mg$_2$Si [91, 133, 143, 144].

The quasiharmonic contribution, in contrast to Si, is large due to significant expansion of this hcp metal. Both the electronic and anharmonic contribution are not large but amount in total to a necessary contribution and yield a finally accurate description in agreement with experimental measurements. The yellow and blue arrow in Fig. 4.8(b) at melting indicate the small difference in the heat capacity between GGA or LDA.

Since it has been shown that anharmonic free energies are very similar for GGA and LDA — a result which was found so far for all fcc elements in Sec. 4.1 and also for the above presented hcp Mg and dc Si — the anharmonic contribution for Mg$_2$Si is exclusively calculated by GGA. The results for the C_P of Mg$_2$Si can be found in Fig. 4.8(c). At low temperatures the calculated heat capacity is very close to experimental measurements, a result which was consistently found for all so far investigated elements. A discussion of both experimental assessments at low temperatures is found in Ref. [91]. For temperatures up to 793 K, experimental measurements exist but are found to scatter significantly. Also different CALPHAD assessments presented in Ref. [91] showed differences of up to 0.7 k_B for the heat capacity at the melting temperature. On the basis of experimental data alone, a conclusive result seems therefore difficult. The theoretical error margins due to LDA and GGA on the other hand were found to yield reliable upper and lower bounds for experimental heat capacity data. In the quasiharmonic assessment of Mg$_2$Si, only a small difference of 0.2 k_B is found between GGA and LDA at the melting point of 1346 K. For Si and Mg, the error due to the functional amounted at their respective melting temperatures to about 0.1 k_B for the quasiharmonic as well as the anharmonic contribution. If similar error margins are assumed for Mg$_2$Si, the self consistent and final GGA prediction which includes anharmonic contributions will also possess a very narrow confidence interval. The final heat capacity for Mg$_2$Si is shown in Fig. 4.8(c). The small difference between the functionals usually corresponds to a high predictive power and is very useful for Mg$_2$Si where no experimental data was obtained above 793 K. The most recent C_P measurement is well in agreement with the theoretical prediction which however possesses the advantage that it is available up to the melting point.

In cases where no experimentally measured heat capacities are available for binary or multinary systems, the Neumann-Kopp rule [145] is readily applied. It extrapolates from the unary constituent heat capacities the resulting binary (or multinary) heat capacity. The Neumann-Kopp rule is formulated for a binary system by

$$C_P^\mathrm{C}(T) = xC_P^\mathrm{A}(T) + yC_P^\mathrm{B}(T) \tag{4.2}$$

where $C_P^A(T)$ and $C_P^B(T)$ are the temperature dependent constituent heat capacities, e.g. for Si and Mg, $C_P^C(T)$ is the resulting heat capacity due to the Neumann-Kopp rule and x and y are the corresponding molar concentrations of the unary elements. For the case of Mg$_2$Si this is given by

$$C_P^{\mathrm{Mg_2Si}}(T) = \frac{2}{3}C_P^\mathrm{Mg}(T) + \frac{1}{3}C_P^\mathrm{Si}(T) \tag{4.3}$$

and can be directly used with the heat capacities gained in Fig. 4.8(a) and (b). Fig. 4.8(c) shows the resulting heat capacity derived for Mg$_2$Si by the Neumann-Kopp rule from Eq. 4.3 by the dashed gray line. A significant discrepancy can be observed to the full *ab initio* calculated C_P curve which amounts at 1200 K already to 0.4 k_B. Similar concerns have been recently raised regarding the applicability of the Neumann-Kopp rule for mixed oxides at high temperatures [145]. In view of these results the general applicability of the Neumann-Kopp rule, in particular for CALPHAD assessments of multinary systems, seems questionable and temperature dependent *ab initio* calculations — as the one developed here — including all vibrational contributions seem a promising alternative for the calculation of heat capacities of binary and multinary solids.

4.4   Point Defects

The properties and performance of modern materials critically depend on the presence of point defects. Already minute changes in their concentrations are known to dramatically impact material properties. The industrial relevance of point defects can be classified into an electronic and an elastic regime. Electronic devices rely on controllable changes of electronic conductivity upon careful introduction of point defects into the perfect crystal. In semiconductors even minute additions can have substantial influence on electronic properties by placing active energy levels inside the band gap. In metallic materials, where electronic effects are less pronounced, the elastic influence of point defects is the basis for an optimized design of structural materials. Point defects act for example as pinning centers for dislocations or even grain boundaries having therewith a direct impact on mechanical strength and ductility. They control diffusion processes, accompany melting processes and therefore govern phase stability and phase transformations.

In view of this enormous economical impact, the experimental characterization of point defects is grossly limited often requiring an ingenious combination of various techniques. Experimentally it is not feasible to measure vacancy concentrations over the whole temperature range which makes theoretical studies indispensable. Sec. 4.4.1 sketches the challenges to compute the anharmonic contribution for defect formation on a fully *ab initio* basis with respect to the here employed thermodynamic integration techniques introduced in Sec. 2.4.2. In Sec. 4.4.2 the two most prominent experimental methods are introduced for measuring vacancy concentrations in solids and actual measurements are shown for Al and Cu. Calculations on divacancies are performed with the here presented methodology and are extended to monovacancies in Sec. 4.4.3.

By a careful study with the two standard exchange-correlation functionals, LDA and GGA, a fundamental observation is made regarding the temperature dependence of vacancy formation followed by a discussion of the results in Sec. 4.4.4. In particular it will be shown that a quasi-harmonic *ab initio* treatment of finite temperature vibrational effects — until recently the only available option for the study of point defects — is not sufficient to capture vacancy formation energies correctly. Further it will be shown that the linear Arrhenius ansatz, $G^f = H^f - TS$, has to be replaced in future studies by the Local Grüneisen theory (LGT) presented in Sec. 3.2.1. Consequences of the here presented results are discussed for the "official" point-defect data as, e.g., compiled in the Landoldt-Börnstein series. Implications are drawn for state-of-the-art DFT exchange correlation functionals.

4.4.1   Including anharmonic contributions to defect formation

For supplementing experimental measurements of defect properties, computational approaches have crystallized as valuable tools. In principle, computations based on empirical potentials have access to the full temperature range starting from $T=0\,\mathrm{K}$ up to the melting point. Indeed, various studies utilizing specifically the embedded atom method have been put forward in the 1990's seeking to explain experimentally found ambiguities [50, 146]. A general reasoning was shaped that the anharmonic contribution, i.e., phonon-phonon interactions beyond the simple non-interacting picture, is playing a crucial role. However, the authors had to admit that the employed empirical potentials showed large scatter and thus any concrete conclusion was fully out of question. Due to the high demands on accuracy, calculations on point defects based on empirical potentials have been questioned [64]. Consequently, great hope was put into an accurate DFT-based solution of the problem. Beginning with the pioneering work of Gillan [147] in 1989, DFT calculations on point defects were limited to $T=0\,\mathrm{K}$ throughout the 90's [148–150]. With advances in hardware technology, finite temperature contribution, in particular electronic and quasiharmonic (non-interacting phonons)

excitations started to be included [50, 151–153]. The full treatment of explicit anharmonicity due to phonon-phonon interactions — relevant at high temperatures — could however still only be performed by resorting to empirical potentials or model potentials derived from DFT. A fully *ab initio* based treatment was computationally too expensive and as of 2005 it was generally accepted that the full set of high temperature excitations cannot be captured within first principles as a consequence of high computational costs [154]. This situation changed only fairly recently, when methods were developed which allow to sample anharmonic contributions (phonon-phonon interactions) efficiently and accurately within the DFT methodology. First studies were put forward showing promising results [2, 9]. The focus of all so far performed *ab initio* studies was to compare concentrations limited to the experimentally accessible temperature range by the use of "Arrhenius" plots. An analysis of the Gibbs energy of defect formation on the other hand — a much more sensitive quantity — turns out to be the better descriptor when comparing theoretical and experimental predictions. Considering this quantity for the full temperature range, from $T=0\,\mathrm{K}$ to the melting temperature, and at the same time including the full excitations spectrum, resulted in a major break-through for the understanding of defect formation and was a major result of this thesis.

To compute the temperature dependence of G^f it is necessary to calculate the free energy of the bulk and the vacancy supercell by considering all relevant excitation mechanisms defined in Eq. 4.1 on page 56 on an *ab initio* basis. The computation of the $T=0\,\mathrm{K}$ total energy, the electronic and quasiharmonic free energy contributions are standard and can be done to a very high numerical precision without significant effort on nowaday's computational resources. Converging however the anharmonic contribution of the *defect formation energy* G^f to a similar precision as defined for the *bulk free energy* F in Sec. 4.1 — usually 1 meV — is a completely new challenge since the relevant energy is scaled *per defect* and not *per atom*, as it is the case for bulk properties. To illustrate this point, an example shell be considered where the anharmonic contribution needs to be sampled for the bulk and defect supercell to a statistical precision of $1\,\frac{\mathrm{meV}}{\mathrm{atom}}$ which for a 100 atom supercell equals $100\,\frac{\mathrm{meV}}{\mathrm{cell}}$ (see Ref. [2] for a discussion on the required precision). The molecular dynamic runs which are necessary for thermodynamic integration are performed for the bulk and defect system on the chosen reference as described in Sec. 2.4.2. Both references are usually obtained in a similar way and are therefore of similar quality. This implies that when energies are sampled for every snapshot, the corresponding energy difference between DFT and the reference potential is on average similar for the bulk runs and the runs containing the defect. Therefore the standard deviation σ is also similar for thermodynamic integration for the bulk and defect system, $\sigma^{\mathrm{bulk}} \approx \sigma^{\mathrm{defect}}$. In the bulk calculation, extensivity holds and the standard error, σ_n, can be calculated as a per atom quantity. In the case of a defect formation energy it is necessary to calculate energy differences of the two supercells (defect minus bulk) and the standard error will therefore be 100 times larger compared to the bulk free energy calculation. Consequences of this are exemplified in the following.

The necessary number of snapshots n in a molecular dynamics run is assessed using the definition of the standard error σ_n with

$$\sigma_n := \frac{\sigma}{\sqrt{n}}. \tag{4.4}$$

Having two reference potentials which either have different standard deviation σ_1 and σ_2 or need to be converged to different standard error σ_{n1} and σ_{n2} one can write

$$\frac{n_1}{n_2} = \left(\frac{\sigma_1}{\sigma_2}\right)^2, \quad \text{and} \quad \frac{n_1}{n_2} = \left(\frac{\sigma_{n1}}{\sigma_{n2}}\right)^2 \tag{4.5}$$

where n_1 and n_2 are the necessary steps to calculate in the corresponding MD run using the

respective reference (e.g. DFT, harmonic or other). Converging the standard error of the bulk system to $\sigma_n = 1\frac{\text{meV}}{\text{atom}}$ when assuming a standard deviation of $\sigma = 10\frac{\text{meV}}{\text{atom}}$ results in $n_b = 10^2$ MD steps for the bulk system. Converging the standard error of the defect system to $\sigma_n = 1\frac{\text{meV}}{\text{defect}} = 1\frac{\text{meV}}{\text{cell}}$ assuming the same standard deviation of $\sigma = 10\frac{\text{meV}}{\text{atom}} = 1000\frac{\text{meV}}{\text{cell}}$ however results in $n_d = 10^6$ MD steps which are necessary for the defect calculations. A dramatic effect is therefore observed on $n^{\text{defect}}/n^{\text{bulk}}$: to obtain the same precision in the defect formation energy as in the bulk free energy calculation a sampling time is necessary which increases by a factor of 10^4. Since, as has been shown in Sec. 4.1, converging the anharmonic bulk free energy to 1 meV/atom is already a difficult task on an *ab initio* level, it becomes clear that to converge defect formation energies to a similar quality is a considerable computational challenge.

For the here employed *ab initio* calculations the UP-TILD method was used as described in Sec. 2.4. Only a few hundred fully converged DFT configurations are needed to achieve to the here desired statistical accuracy of 0.1 meV/atom in $F(V, T)$ and 10 meV/defect in the corresponding 108(107) atom cell for G^f. Using this approach all contributions entering the free energy of the vacancy cell and perfect bulk cell, F^{vac} and F^{bulk}, are computed as a function of volume and temperature. The temperature and pressure dependent Gibbs energy of formation is then given by:

$$G^f(P, T) = F^{\text{vac}}(\Omega, T; N) - N F^{\text{bulk}}(V, T) + P v^f. \tag{4.6}$$

The volume of the defect supercell Ω with N atoms and the volume per atom V of the perfect bulk are self-consistently determined to correspond to a given pressure P (standard atmospheric pressure). The volume of vacancy formation is given by $v^f = \Omega - NV$.

For the in the following presented *ab initio* calculations on defect formation in Al and Cu a summary of technical aspects and a rigorous account for the convergence tests performed can be found in Refs. [68] and [92]. The convergence errors due to DFT related parameters (e.g., k-points, energy cutoff) are shown in the mentioned references for the performed $T=0$K, electronic and quasiharmonic and anharmonic calculations. Statistical sampling has been very carefully checked and is ensured to be below 0.1 meV/atom for every MD run.

4.4.2 Mono- and divacancy interpretation of vacancies in Al and Cu

The key quantity to characterize point defects is their Gibbs energy of formation, G^f, defined in Eq. 3.18 on page 45. Despite the enormous economical impact of point defects, large discrepancies can be found among the available G^f data even for simple materials like Al and Cu. The major obstacle is deeply rooted in the very nature of point defects: all affected properties are inevitably governed by the defect concentration $c = \exp[-G^f/(k_{\text{B}}T)]$. It is the exponential factor in this expression that renders any experimental observation a challenge, forcing strict bounds upon the available statistics and the accessible temperature window. In Sec. 3.2.1 it was therefore elaborated that measurements of point concentrations can only be performed at sufficiently high temperatures.

In practice, experiments are restricted to a temperature range between $\approx$60% to 100% of the melting point as indicated in Fig. 4.9 for Al and Cu by the gray shaded area. For any element in the periodic table virtually no measurements exist for vacancy concentrations below this temperature window. Take differential dilatometry (DD) as an example, the main experimental workhorse for determining vacancy concentrations pioneered by Simmons and Balluffi in the 60's [155]. DD is built on the fact that creating a vacancy — by bringing an atom to the surface — leads to an *increase* in the macroscopic length L of the sample, $\Delta L/L_0$, where L_0 is the length at a given temperature. Due to the presence of vacancies in the solid the macroscopic expansion is greater than

---

[3]Fitting the highly accurate DD data of copper [81] (>1220 K) as suggested in Ref. [82] results in $H^f = 1.35$ eV.
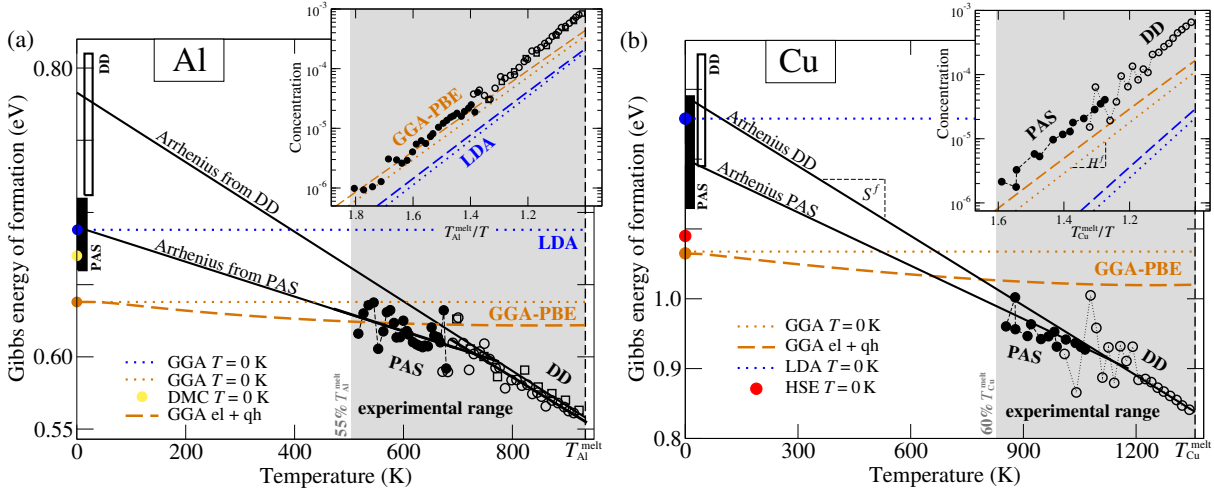
Figure 4.9: Experimental (black symbols) and DFT [blue/orange (LDA/GGA-PBE) lines] Gibbs energy of formation of vacancies in (a) Al and (b) Cu. The insets show the corresponding vacancy concentration in the typical Arrhenius plot. Experiments (PAS=positron annihilation spectroscopy [81], DD=differential dilatometry [81, 155]) are limited to a region (gray shaded) close to the melting point, $T_{\mathrm{Al/Cu}}^{\mathrm{melt}}$. Extrapolations of available PAS [81, 156–160] and DD data [81, 82, 155, 156, 161–163] to $T=0\,\mathrm{K}$ using the common Arrhenius ansatz introduced in Sec. 3.2.1, $G^f(T) = H^f - TS^f$, introduce scatter in the reported values (filled/empty black bars mark corresponding intervals)[3]. Formation energies computed by common *ab initio* approximations such as the $T=0\,\mathrm{K}$ (dotted line) and the electronic plus quasiharmonic (el+qh; dashed line) approach are shown. The yellow and red dots in Al and Cu correspond to highly accurate $T=0\,\mathrm{K}$ calculations using QMC (many-body diffusion quantum Monte Carlo) and the HSE (Heyd-Scuseria-Ernzerhof) functional taken from Refs. [126, 164].

the simultaneously measured increase in $\Delta a/a_0$ where a is the lattice spacing measured e.g. by X-ray techniques. Measuring $\Delta L/L_0$ simultaneously with $\Delta a/a_0$ with increasing temperature, accurate defect concentrations can be obtained at high temperatures and concentrations where statistics is sufficient. The final concentration using differential dilatometry is defined as $c = 3(\Delta L/L_0 - \Delta a/a_0)$. For a long time the mentioned high temperature DD data of Simmons and Balluffi [66, 155, 165–167] were an untouchable reference. In 1994, Hehenkamp [81] was able to set a new accuracy standard in DD measurements and it became possible to measure absolute defect concentrations down to about 10^{-5} which can also be seen in the insets of Fig. 4.9(a) and (b). The same figures nicely capture the strength and limitations of DD (open circles): in the temperature range from the melting point of both elements down to about 80% of T^{melt}, the data points are lying accurately on a smooth curve. Below 80% of T^{melt}, the measured points suddenly start exhibiting a strong scatter. In this temperature/concentration regime statistics are too poor to provide a reliable picture.

The situation can be somewhat improved by utilizing positron annihilation spectroscopy (PAS) developed in the early 70's (see Ref. [168] for a summary). PAS relies on the fact that positron lifetime inside a material increases with increasing vacancy concentration. Due to a strong correlation of this dependency, it allows to assess a lower concentration window (down to $\approx 10^{-6}$) and thus a lower temperature range than DD (filled circles in Fig. 4.9). PAS has, however, other severe limitations: above roughly a concentration of 10^{-4} saturation effects set in prohibiting accurate measurements. An even greater shortcoming is that PAS in general does not yield absolute vacancy concentrations and can do so only if the measured temperature dependence can be aligned with other absolute data [81]. In principle though it will only provide vacancy formation enthalpies H_f
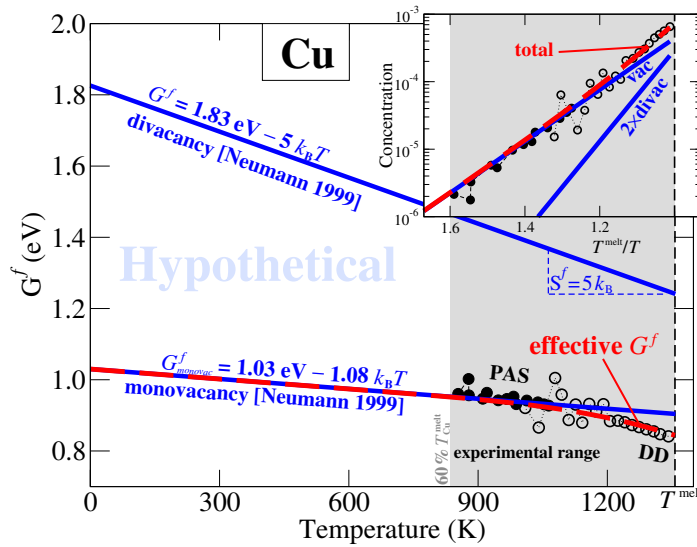
Figure 4.10: Example assessment for the copper vacancy formation energy in the generally applied mono- and divacancies picture as evaluated by Neumann [82]. The blue solid lines show the corresponding Gibbs energies of formation. Respective concentrations of mono- and divacancies are plotted in the inset. Due to application of the Arrhenius law, enthalpy and entropy of formation are temperature independent for both defect species. The red dashed line is the effective $G_{\text{eff}}^f(T)$ in Eq. 4.10 which is obtained assuming $c_{\text{total}} = c_{\text{vac}} + 2c_{\text{divac}}$ as explained in the text. Experimental data (black) are similar to Fig. 4.9.

which correspond to the slope in the insets of Fig. 4.9 but in general never entropies of formation. All this renders experimental point defect characterization a daunting task. Yet, combining both methods, the best one can ever hope to achieve for unary elements are accurate concentration measurements to not lower than $\approx 60\%$ of the homologous temperature. Details regarding DD and PAS can be found in Refs. [61, 92, 168, 169].

Despite the new accuracy standard set by DD and PAS, significant and so far unexplained ambiguities remain: depending on the method and considered fitting range, the extrapolated enthalpy of formation yields a large window which is shown in Fig. 4.9 by the filled and empty black columns on the left, marked by DD and PAS. This clearly introduces uncertainties regarding the interpretation of point defect measurements. The established model for point defect formation assumes an Arrhenius-like behavior $G^f(T) = H^f - TS^f$ with temperature *independent* enthalpy and entropy H^f and S^f. As shown in Fig. 4.9, the limited and scattered experimental data do not allow to check the accuracy of this assumption in the experimentally accessible range. Indeed, Fig. 4.9 indicates deviations from the simple linear Arrhenius behavior [difference in slopes between positron annihilation spectroscopy (PAS) and differential dilatometry (DD) data] [68] which have been extensively and controversially discussed over the last decades [50, 63, 64, 81, 152, 170]. There are essentially two, not exclusive, alternatives which are heavily debated in literature [64] to explain the inconsistencies between PAS and DD measurements: Either (A) the enthalpy and entropy of formation of the point defect, H^f and S^f, are temperature dependent or (B) the experiment measures effective concentrations which are dominated not only by one, but by at least two types of point defects. Model (A) is in principle plausible since PAS and DD access different temperature windows (see also black open and filled experimental data in Fig 4.9) and consequently measure different H^f values. Assumption (B) however is clearly favored in literature with divacancies as the second defect species. A temperature dependence of H^f and S^f on the other hand was until recently clearly against expectations [64] leaving divacancies as the only considered solution.

Assuming the mono- and divacancy picture, the effectively measured vacancy concentration is written as

$$c = c_{\text{total}} = c_{\text{vac}} + 2c_{\text{divac}} \tag{4.7}$$

Element	Al	Al	Cu	Cu	Cu	Cu
Reference	[64]	[163]	[82]	[171]	[156]	[173]
S_{mono}^f	0.76	0.6	1.08	2.5	1.4	0.35
S_{di}^f	3.2	2.2	5	6.7	4.9	1-2
factor	**3.7**	**4.2**	**4.6**	**2.7**	**3.5**	**2.9-5.7**

Table 4.1: Mono- and divacancy entropies of formation for Al and Cu. The factor S_{divac}^f/S_{vac}^f illustrates the remarkably high divacancy entropies which have to be assumed in a mono- divacancy picture to fit the corresponding experimentally found curvature of G^f. Reference [82] is additionally illustrated in Fig. 4.10.

where the factor 2 emphasizes that a divacancy effectively creates two free lattice sites. Corresponding concentrations of mono- and divacancies are defined using Eq. 3.17 on page 45

$$c_{vac} = 1 \exp\left[\frac{-G_{vac}(T)}{k_B T}\right], \qquad \text{and} \qquad c_{divac} = 6 \exp\left[\frac{-G_{divac}(T)}{k_B T}\right] \qquad (4.8)$$

where the corresponding geometry factors have been used. Assuming an Arrhenius behavior for the mono- and the divacancy,

$$G_{vac}(T) = H_{vac} - T S_{vac}, \qquad \text{and} \qquad G_{divac}(T) = H_{divac} - T S_{divac} \qquad (4.9)$$

and solving Eq. 3.17 for $G^f(T)$, yields an effective Gibbs energy of vacancy formation

$$G_{eff}^f(T) = -k_B T \ln[c_{total}] = -k_B T \ln\left[\exp\left(-\frac{H_{vac} - T S_{vac}}{k_B T}\right) - 12 \exp\left(-\frac{H_{divac} - T S_{divac}}{k_B T}\right)\right],$$
$$(4.10)$$

which is not linear and can be fitted to experimental data. This situation is illustrated in Fig. 4.10 for an assessment of copper by Neumann [82]. The aluminum vacancy is another prominent and rigorously investigated example where the high temperature DD measurements consistently indicate a larger effective formation enthalpy than the low temperature positron data [81]. These observations result in a significant curvature of formation energy in the high temperature regime (compare Fig. 4.9(a)).

A crucial requirement when applying Eq. 4.10 is that the offsets and slopes of the mono- and divacancy G^f curves, i.e., $H_{vac/divac}$ and $S_{vac/divac}$, obey certain relations in order to be in agreement with the observed curvature of the effective $G_{eff}^f(T)$ in the high temperature region. In particular, S_{divac} needs to be considerably higher for the divacancy in comparison to the monovacancy. Table 4.1 collects current evaluations for aluminum and copper and highlights the huge differences between S_{vac} and S_{divac} which result in significant divacancy concentrations. Depending on the assessment, about 20% to 40% of the defects at the melting temperature have to be divacancies. This generally found experimental interpretation is found in numerous evaluations [64, 82, 156, 163, 171–173]. Unfortunately however it is not possible to separate the experimentally measured effective concentrations into mono- and divacancies. A verification of experimentally evaluated divacancy concentrations is currently not feasible and a theoretical investigation therefore highly desirable.

Theoretical studies on mono- and divacancy formation have so far been restricted to $T=0$ K. Corresponding formation energies for Al and Cu are shown in Fig. 4.9 as dotted lines. Finite temperature vibrational effects could only be approximated for these systems in a harmonic or (quasi-) harmonic ansatz and the results for Al and Cu are also shown in Fig. 4.9. The possible
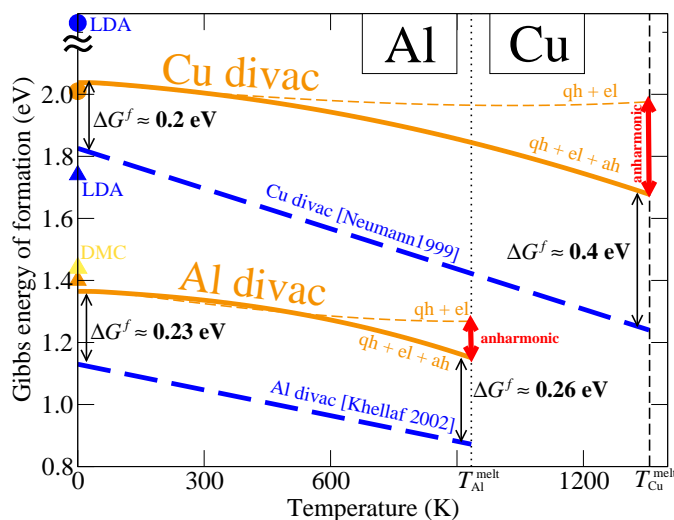
Figure 4.11: Gibbs energies of divacancy formation for Al and Cu based on DFT GGA-PBE results of the present study including all relevant excitation mechanisms: quasiharmonic, electronic and anharmonic. Experimental assessments (blue dashed lines) are taken from Refs. [64, 82]. Resulting divacancy concentrations at the melting point differ by approximately two orders of magnitude between DFT calculations and the shown assessments for both elements. LDA and QMC results for Al and Cu at $T=0\,\mathrm{K}$ (yellow and blue triangles and dot) are taken from Refs. [152, 164, 174].

deficiencies of this approach on defect formation properties have been discussed in Sec. 3.2.1. To treat the full temperature dependence on a fully *ab initio* basis was until recently fully out of question. Taking the theoretical restrictions to low temperatures and the experimental restriction to high temperatures into account, it becomes evident that a direct and conclusive comparison of experiment and theory has so far been hampered by a large temperature gap. To test current assessments as presented in Fig. 4.10, the formalism introduced in Sec. 4.4.1 is ideally suited. It allows to investigate the full vibrational spectrum of defect formation including anharmonic contributions and is therefore able to in particular clarify whether, as postulated by model (B), di-vacancies contribute to the non-Arrhenius behavior shown in Figs. 4.9 and 4.10. Applying presented methodology by including all excitation mechanisms including quasiharmonic, electronic and especially anharmonic contributions the temperature dependence of G^f_{divac} was calculated.

Fig. 4.11 shows for the GGA functional the calculated quasiharmonic plus electronic Gibbs energy of divacancy formation (dashed orange lines) for aluminum and copper as well as the final result including anharmonic contributions (full lines) up to the melting temperature. The calculated GGA formation energy compares well with recent literature values at $T=0\,\mathrm{K}$ for Al [175] (orange triangle) and Cu [63] (orange dot). The shown $T=0\,\mathrm{K}$ LDA and QMC formation energies (blue and yellow) from Refs. [164, 170, 176] are higher in comparison to GGA results. This trend is well known in literature [177] and consistent with the formation energies in GGA and LDA for the mono- vacancy shown in Fig. 4.9. For both material systems a substantial anharmonic contribution can be observed, indicated by red arrows at the corresponding melting temperature. Especially the high divacancy formation enthalpies at $T=0\,\mathrm{K}$ result in gross deviations from postulated divacancy results shown by the dashed blue lines. The temperature dependence of the final curves shows deviations from the generally assumed linear Arrhenius dependence. The resulting divacancy concentrations are found to be in gross contrast to the estimated values. Focusing on Cu, the $T=0\,\mathrm{K}$ G^f (actually H^f) for divacancies is roughly equal to the 2 eV, being therewith approximately twice the value for the monovacancy G^f of 1.06 eV (see Fig. 4.9). The governing physics is quickly identified: for creating a monovacancy it is necessary to break 12 bonds (fcc structure) while $(2 \times 12 - 1)$ bonds are removed for a divacancy. The resulting GGA divacancy concentrations at the melting point resulting from our calculations are about $6 \times 10^{-7} - 7 \times 10^{-7}$ and are summarized in Table 4.2. The corresponding PBE monovacancy concentrations are reported for completeness and taken from Sec. 4.4.3. Comparing to the total effectively measured exper-

Table 4.2: Comparison of mono- and divacancy concentrations in Al and Cu at their corresponding melting temperature which in experiment cannot be measured independently. Monovacancy results are presented in detail in Sec. 4.4.3 and are reported for completeness. A concise summary of Al vacancy data can be found in Ref. [81]. For Al the experimental concentrations are taken from Ref. [64] by the given values of $H_{\mathrm{vac}}^f = 0.65$ eV, $H_{\mathrm{divac}}^f = 1.13$ eV, $S_{\mathrm{vac}}^f = 0.8$ eV and $S_{\mathrm{divac}}^f = 3.2$ eV.

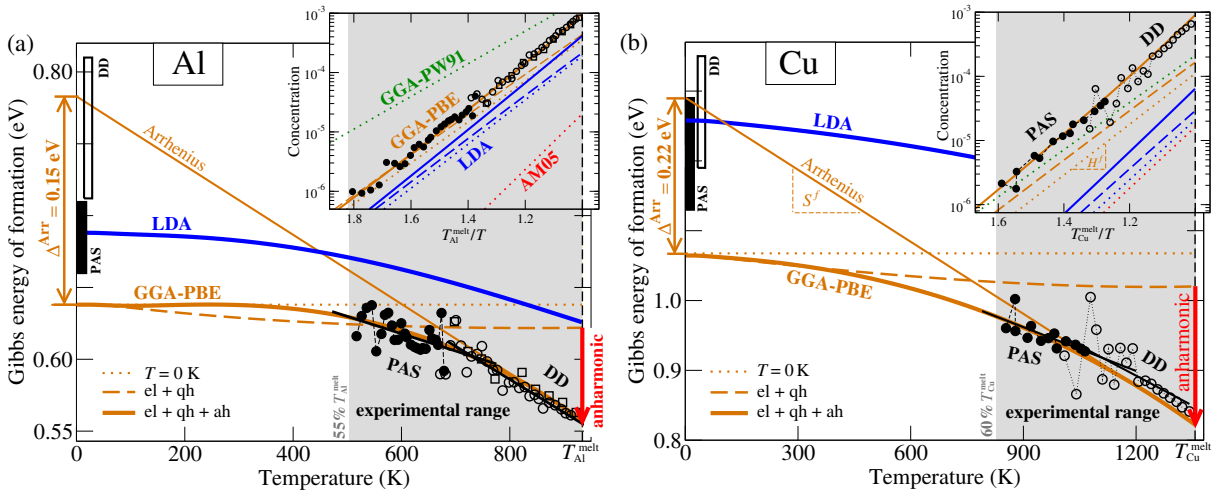|		Reference	c_{total}	c_{mono}	c_{divac}	$c_{\mathrm{divac}}/c_{mono}$
Experiment	Al	[64]	9.3×10^{-4}	6.9×10^{-4}	1.2×10^{-4}	17%
	Cu	[82]	7.4×10^{-4}	4.4×10^{-4}	1.5×10^{-4}	34%
Theory	Al	this work (PBE)	9.7×10^{-4}	9.7×10^{-4}	7.0×10^{-7}	$\sim0.1\%$
	Cu	this work (PBE)	8.8×10^{-4}	8.8×10^{-4}	5.9×10^{-7}	$\sim0.1\%$

Figure 4.12: Extended version of Fig. 4.9, in which additionally the full curves are shown (el+qh+ah) which include all free energy contributions in particular anharmonicity. The error resulting when assuming the Arrhenius extrapolation, $\mathbf{\Delta}^{\mathrm{Arr}}$, is marked by the orange arrow at $T{=}0$ K. Figure is adopted from Ref. [68].

imental concentrations, $7 \times 10^{-4} - 9 \times 10^{-4}$, those are $\sim0.1\%$ for Al and Cu, respectively, and not 20% to 40% as had to be assumed in the empirical model (B), i.e., two orders of magnitude smaller. Divacancy formation energies in LDA or using QMC formation energies are seen to be even *higher* and therefore result in even *lower* divacancy concentrations with corresponding *greater differences* to experimental estimates. The consequence of these observations is that (a) the ratio between the mono and di-vacancy entropy is rather similar and not differing by up to a factor of 5 as was summarized in Table 4.1 and, more importantly, that (b) di-vacancies [model (B)] can be clearly ruled out as a source of the non-Arrhenius behavior for both elements [152] due to negligible concentrations. The strong temperature dependence of the formation energy of the mono-vacancy shown in Fig. 4.9 remains therefore as an exclusive source.

4.4.3   Gibbs energies and entropies of defect formation

In the previous section the mono- divacancy model has been ruled out as a possible mechanism to explain the temperature dependence observed for PAS and DD data shown in Fig. 4.9. From the same figure it is also evident that a purely *ab initio* quasiharmonic treatment of atomic vibrations including electronic contributions is not sufficient to capture the experimental results of mono-
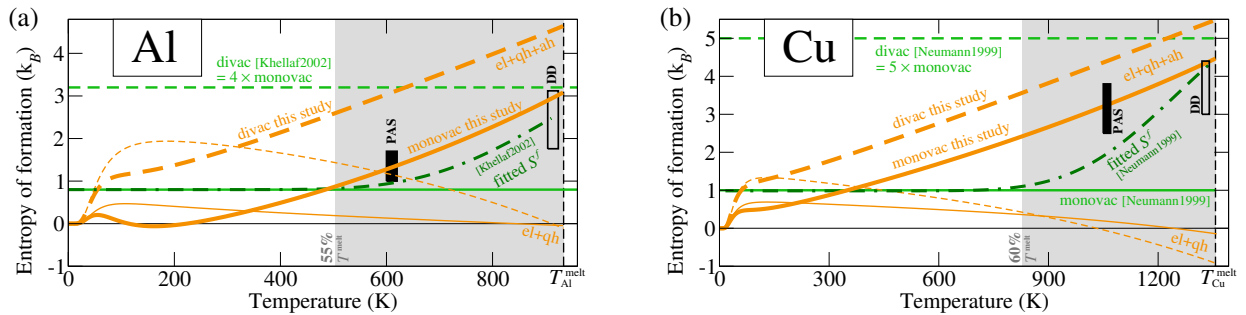
Figure 4.13: Entropy of formation, $S^f = -dG^f/dT$, for the (a) Al and (b) Cu mono- (solid) and di-vacancy (dashed line). The thinner lines indicate the entropy of formation considering only the electronic and quasiharmonic free energy contribution (el+qh). The thick curves include all contributions in particular anharmonicity (el+qh+ah). Green lines represent numbers suggested in Refs. [64, 82] for explaining non-Arrhenius behavior within a mono- and di-vacancy model. Experimental PAS and DD entropies (filled/empty black bars) are derived from the experimental data shown in Fig. 4.12. Note that in general PAS experiments only provide the enthalpy of formation, H^f. The values for the entropy of formation, S^f, are given in experiments when the trapping rate is known or additional DD data is available to align PAS measurements as done in Ref. [81]. Figure (b) and the caption are adopted from Ref. [68].

vacancy formation. In this section, results will be presented which employ highly accurate finite temperature DFT calculations for the monovacancy including in particular anharmonic excitations.

Fig. 4.12 compiles available experimental data and shows the resulting Gibbs energy of mono-vacancy formation for Al and Cu for the two commonly employed exchange-correlation functionals LDA and GGA (thick solid blue and orange lines). For the full solution a strong non-negligible deviation from the linear Arrhenius law can be observed. Considering only the experimentally accessible temperature window (gray shaded regions in Fig. 4.12) this deviation is difficult to determine with certainty. Having the full temperature dependent formation energy at hand, from $T=0$ K to the melting temperature, allows to measure the error introduced by assuming the state-of-the-art linear Arrhenius extrapolation. When applying the general procedure, a fit through the GGA high-temperature data (orange "Arrhenius" lines), the extrapolated $T=0$ K vacancy formation energy significantly overestimates the actually calculated formation energy by 0.15 eV ($\approx 23\%$) for Al and 0.22 eV ($\approx 20\%$) for Cu [68]. Since so far only the linear Arrhenius extrapolation has been used also for other elements, non-negligible corrections to the generally accepted $T=0$ K formation energies might possibly be found also for other systems. For the investigated elements, Al and Cu, the differences between PAS and DD formation enthalpies can now be understood by the presented results. As assumed by model (A) in Sec. 4.4.2, the two methods are restricted to distinct temperature ranges and probe therefore the slope of the temperature dependent (non-Arrhenius) formation energy curve in different temperature regions.

The presented results reveal that anharmonic phonon-phonon interactions are an integral contribution to vacancy formation energies and need to be considered in future studies. Previously reported discrepancies between DFT-GGA and experimental vacancy formation disappear and it is possible for the first time to consolidate PAS and DD measurements and theoretical *ab initio* results in one unified picture.

Having determined the full vacancy formation energy $G^f(T)$ it is furthermore possible to directly derive the *ab initio* computed formation entropy $S^f(T)$. For both elements, Fig. 4.13 shows the corresponding results. The current experimental assessments which were restricted to the mono- and divacancy picture, are shown in green. The experimental entropies for Al [64] and Cu [82] are

presented in light green for the monovacancy (full line) and divacancy (dashed line). To reflect the difference between experimental PAS and DD formation entropies, a critical assumption that had to be made in the empirical mono- divacancy model was to assume for di-vacancies a much larger entropy of formation than for mono-vacancies. This can be seen in Fig. 4.13 and is also summarized for other evaluations in Table 4.1 on page 76. The dark green (dashed dotted) curve represents the final and effective experimental formation entropy which takes into account mono- and divacancies. It reflects the increase in entropy at high temperatures. From the fully *ab initio* calculated results it is seen that the actual ratio between mono- and divacancy entropy of formation (orange dashed versus full lines) is positive but in gross contrast to the factor of up to 5 higher which had been postulated when assuming an Arrhenius behavior. The here presented calculations show that this assumption is unsustainable and that the ratio between the mono- and divacancy entropy of formation is very similar in the experimentally accessible high temperature region.

4.4.4 Breakdown of the Arrhenius law and implications

Parts of the following discussion follow the outline of Ref. [68].

In Sec. 3.2.3 defect formation energies and entropies were assessed by making a formal connection to the Grüneisen theory of solids which goes beyond a harmonic ansatz for the potential of atoms close to the defect. This connection allows to understand a further important feature which can be observed in the calculated vacancy formation entropy of Al and Cu in Fig. 4.13: The formation entropy it is not a temperature independent constant. This assumption however is essential for the Arrhenius approximation. For Al and Cu a linear temperature dependence is found with an offset at low temperatures and the same behavior is observed in good approximation for both, mono- and di-vacancies. Integrating this linear temperature dependent entropy of vacancy formation leads to the observed T^2 scaling in the Gibbs formation energy (see Fig. 4.12). It can therefore be followed that the calculated numerical results follow the temperature dependence found for the LGT energy and entropy of formation which were derived in Sec. 3.2.3 and are shown in Figs. 3.10(d) and (f) on page 54. These findings suggest that the nature of this behavior for defect calculations might be generic.

It has been shown [68] that at least for Al and Cu the formation entropy, S, is not constant but has to be replaced with a model in which it is expanded up to the first order in temperature $S^f(T) \approx S_0 + S'T$. This definition is similar to the LGT entropy (Eq. 3.38) derived in Sec. 3.2.3. A further observation from Fig. 4.13 is that for mono-vacancies (solid orange line) the S_0 term is negligible with respect to the $S'T$ term. For divacancies the corresponding offset is higher but the corresponding contributions have been found to be negligible for the effective vacancy concentrations and do not influence the effective results. It will be therefore further approximated:

$$S^f(T) \approx S'T, \quad \text{with } S' = \text{const.} \tag{4.11}$$

Using the general thermodynamic relation

$$\left(\frac{\partial H}{\partial T}\right) = T\left(\frac{\partial S}{\partial T}\right) \tag{4.12}$$

and inserting the entropy in Eq. 4.11, the enthalpy of formation can be gained by integrating both sides

$$H^f(T) = C + \frac{1}{2}S'T^2 = H^f_{0K} + \frac{1}{2}S'T^2 \tag{4.13}$$

where the integration constant C is identified as the formation enthalpy H^f_{0K} at $T=0$ K. This

Table 4.3: Comparison of the previously applied linear Arrhenius approximation and the newly proposed Grüneisen theory (LGT). Table is adopted from Ref. [68].

	Enthalpy of formation	Entropy of formation	Gibbs energy of formation	Temperature dependence of G^f	Fitting coefficients
Linear Arrhenius approximation	$H_{0K}^f \equiv$ const.	$S^f \equiv$ const.	$G^f = H_{0K}^f - TS^f$	linear	H_{0K}^f, S^f
Local Grüneisen theory (LGT)	$H_{0K}^f \equiv$ const.	$S^f = TS'$ $S' \equiv$ const.	$G^f = H_{0K}^f - \frac{1}{2}T^2 S'$	quadratic	H_{0K}^f, S'

relation corresponds to fitting experimental point defect formation Gibbs energies to

$$
\begin{aligned}
G^f(T) &= H^f - TS^f \\
&= H_{0K}^f + \frac{1}{2}S'T^2 - T\,S'\,T \\
&= \boxed{H_{0K}^f - \frac{1}{2}T^2\,S'}
\end{aligned}
\tag{4.14}
$$

rather than to $G^f = H_{0K}^f - T\,S^f$ with $S^f =$ const. The *ab initio* derived LGT based on Eq. (4.14) has the same number of fitting coefficients as the linear Arrhenius model [68]. While both require H_{0K}^f, the fitting of S in Arrhenius approximation is replaced by fitting the slope, $S' = \partial S^f / \partial T$, in LGT. Table 4.3 is used to compare the main differences between the conventional linear Arrhenius approximation and the *ab initio* derived LGT.

Assuming an LGT type of vacancy formation as derived in Eq. 4.14 has far reaching consequences with respect to experimental and theoretical evaluations of vacancy formation. All experimental studies have so far used the conventional Arrhenius dependence with *constant* entropies of formation. Applying however the LGT extrapolation to experimental measurements will result in $T=0$ K enthalpies which differ from the experimentally assessed values. For Al and Cu, revised enthalpies of formation at $T=0$ K (equivalent to H_{0K}^f) are given in Tab. 4.4 when using solely experimental input data with the LGT extrapolation derived in Eq. 4.14 (eights row, grey shaded: LGT DD+PAS). These values are compared to previous Arrhenius extrapolations of PAS and DD data (fourth and fifth row, Arrhenius DD and Arrhenius PAS). When performing such a linear extrapolation, errors of up to 0.24 eV are introduced in comparison to fully *ab initio* calculated data (Δ^{Arr} in Fig. 4.12).

For Al, the experimental DD and PAS assessments extrapolated by the Arrhenius law span a range of up to 0.15 eV as shown in Fig. 4.12 by the filled and empty black bars. Tab.4.4 shows that the Landoldt-Börnstein formation energy — extrapolated linearly from PAS data — is close to the revised LGT formation energy (delta of 0.01 eV) and thus unlikely to change any conclusions/benchmarks where this value has been used [68]. For Cu a similar spread of 0.25 eV is found at $T=0$ K between experimental PAS and DD extrapolations. Here however the difference between the revised LGT value and the one recommended by Landoldt-Börnstein is 0.22 eV, i.e., an order of magnitude larger as for Al, making it mandatory to use the revised value [68]. Recent *ab initio* calculations on Ag [126] using HSE $T=0$ K calculations show an excellent agreement between high temperature experimental data extrapolated to $T=0$ K using LGT. Corrections due to LGT turn out to be 0.15 eV for Ag with respect to the recommended Landoldt-Börnstein values. Consequently, providing revised experimental enthalpies also for other elements seem highly desirable to guide future studies which rely on the availability of highly accurate experimental data.

For elements as Cu and Ag a direct comparison of theory and experiment can not be achieved without the use of accurate extrapolation methods as LGT. Future studies need to clarify whether the assumption $S_0 \approx 0$ made in Eq. 4.11 is valid for Al and Cu only (and apparently Ag) or whether this assumption can be universally applied when calculating vacancy formation entropies.

Table 4.4: Comparison of experimental formation enthalpies from the compilation in the Landoldt-Börnstein series [178] and of Arrhenius-extrapolated PAS and DD formation enthalpies (averaged values of black filled/empty bars in Fig. 4.12) with experimental values obtained from the here proposed local Grüneisen theory (LGT; Tab. 4.3) and with *ab initio* computed formation enthalpies at $T=0\,\mathrm{K}$. For computing the *ab initio* values various flavors of exchange-correlation functionals have been employed: LDA, GGA-PBE, GGA-PW91, and AM05. Additionally, surface corrections based on the scheme from Ref. [177] have been used for the PBE and PW91 functional. The columns labelled Δ_{exp} give the difference to the LGT DD+PAS value. Table and caption are used form Ref. [68].

		Al		Cu	
		H_{0K}^{f}	Δ_{exp}	H_{0K}^{f}	Δ_{exp}
Experiment	Landoldt-Börnstein [178]	0.67	0.01	1.28	0.22
	Arrhenius DD	0.72	0.06	1.30	0.24
	Arrhenius PAS	0.68	0.02	1.20	0.14
	LGT DD	0.67	0.01	1.07	0.02
	LGT PAS	0.65	-0.01	1.05	-0.01
	LGT DD+PAS	**0.66**	**0.00**	**1.06**	**0.00**
Theory	LDA	0.69	0.03	1.26	0.20
	PBE	0.64	-0.02	1.06	0.00
	PBE+surface corr.	0.82	0.16	1.37	0.31
	PW91	0.51	-0.15	0.99	-0.07
	PW91+surface corr.	0.75	0.09	1.39	0.33
	AM05	0.87	0.21	1.29	0.23

A further observation worth noticing in Fig. 4.12 is the similarity of the curvature in the temperature dependence found for LDA and GGA. While at $T=0\,\mathrm{K}$ the formation enthalpies, H_{0K}^{f}, differ between LDA and GGA, the calculated temperature dependence (curvature) are remarkably similar. This finding is important since it unveils that a nonlinear vacancy formation energy, as derived by LGT, is valid *irrespective* of the chosen exchange-correlation (xc) functional. Therefore, the temperature dependent GGA or LDA data can both be fitted to experimental high temperature data and will yield a universal formation enthalpy at $T=0\,\mathrm{K}$. Since experimental high temperature formation energies are known to a very high accuracy of about 20meV per defect (see Fig. 4.12), consequences for the performance of current xc functionals can be drawn.

Figure 4.12 clearly shows that the GGA-PBE based curves are in very good agreement with all the available experimental data in absolute value and curvature. The *ab initio* derived LDA curve on the other hand shows a systematical offset towards too high formation energies (albeit with a similar curvature). The agreement of GGA-PBE for the vacancy formation in copper has meanwhile been confirmed by combining LGT with HSE calculations at $T=0\,\mathrm{K}$ [126]. The in this thesis derived LGT is in evident contrast to the established interpretation of DFT results for vacancy formation which were in the past a) drawn from calculations without the inclusion of anharmonicity and b) compared to Arrhenius-extrapolated experimental data [152, 177, 179]. In these previous studies, it was found that LDA is better suited to calculate vacancy formation energies at $T=0\,\mathrm{K}$ since the corresponding formation enthalpies — which were however drawn from Arrhenius extrapolated data — fitted experimental high temperature data best. The general conclusion was that PBE
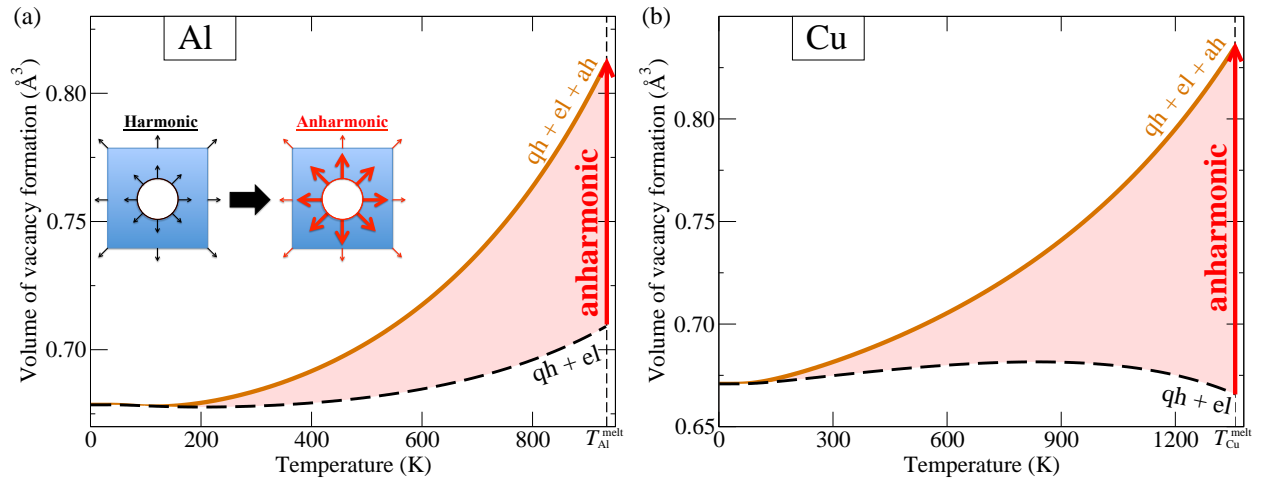
Figure 4.14: Volume of vacancy formation as defined in Eq. 3.26 for (a) Al and (b) Cu including quasiharmonic plus electronic contributions (dashed lines) and additional anharmonic contribution (full lines). The inset in the left figure is a schematic reflecting the substantial increase of the defect cell upon consideration of anharmonic effects.

and PW91 systematically underestimate experimental findings. This argumentation can now be understood due to Fig. 4.12 when comparing the Arrhenius line (orange) to the *ab initio* formation energies at $T=0\,\mathrm{K}$ which were available at that time. The Arrhenius extrapolation overestimates the actual temperature dependence (for LDA and GGA) and therefore agrees well with the higher formation energies found for Al and Cu by the LDA functional. A similar conclusion can be drawn when comparing in Tab. 4.4 the experimentally extrapolated *Arrhenius* $H_{0\mathrm{K}}^{f}$ values (PAS and DD) to the theoretical values in the lower part of the table.

The apparent success of LDA to describe vacancy formation better than GGA has been previously explained by the fact that LDA describes surfaces in metals better than GGA [177, 180]. It was anticipated that vacancies — which can be regarded as an inner surface in a bulk system — need to be calculated by novel xc-functionals [152, 181] which are able to partly correct the energetics of inner surfaces. The performance of corresponding functionals was however benchmarked against Arrhenius extrapolated experimental data. Consequently, concepts which use surface corrections to remedy for DFT errors need to be revised since the current study clearly shows that the agreement of LDA to Arrhenius extrapolated data is accidental as has been discussed above. Tab. 4.4 shows the vacancy formation energy at $T=0\,\mathrm{K}$ for three functionals which include surface corrections (lines: PBE+surface corr., PW91+surface corr., AM05). The corresponding data is additionally displayed in the inset of Fig. 4.12. All three surface corrected functionals yield significantly too large formation energies at $T=0\,\mathrm{K}$ in comparison to the revised LGT values and also in comparison to the uncorrected functionals. Considering in Tab. 4.4 the suggested value by Landoldt-Börnstein — which was extrapolated linearly — it becomes evident why surface corrected functionals had been favored previously and also highlights the importance to accurately extrapolate experimental data to $T=0\,\mathrm{K}$ [68]. This study has shown that the overall best performance is found for non-surface corrected functionals and in particular GGA-PBE as shown in Table 4.4 and Fig. 4.12.

In Sec. 3.2.3 the temperature dependent volume of defect formation has been considered in Eq. 3.26 when formulating the defect formation entropy. The majority of theoretical studies has investigated this quantity exclusively at $T=0\,\mathrm{K}$ [182–184]. Theories aiming to predict the temperature dependence of the vacancy volume turned out to be a daunting task [185, 186]. Corresponding
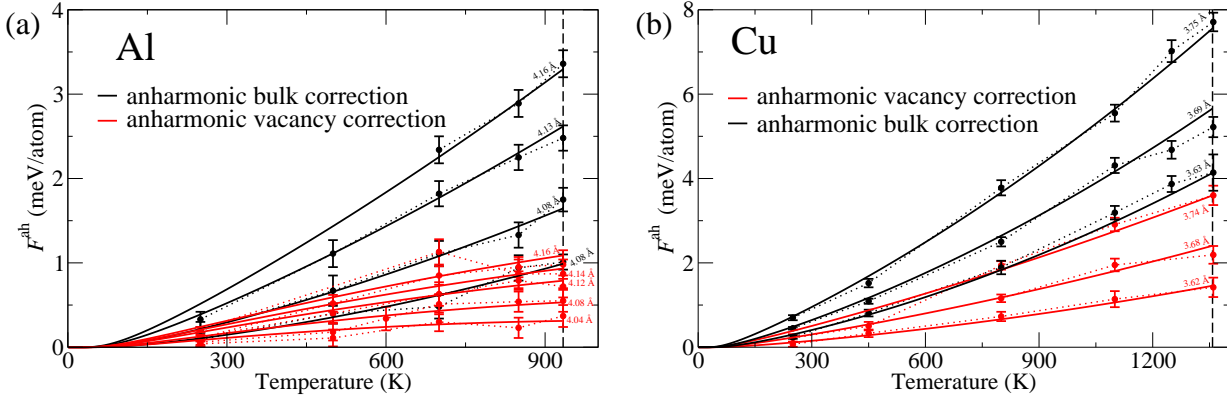
Figure 4.15: Explicit GGA anharmonic free energy contribution F^{ah} for bulk (black) and for the defect supercell (red) as a function of temperature for (a) Al and (b) Cu. The calculated lattice constants are shown in Å. The anharmonic free energies were scaled per atom. The calculated averages and corresponding statistical errors are represented by the filled dots and vertical solid lines and were obtained in a 108/107 atomic fcc conventional supercell. A slight convex temperature dependence can be observed for the vacancy while a concave dependence is seen for the bulk. The solid lines correspond to the performed fit of the free energy surface and the dotted lines are merely a guide for the eye. The anharmonic correction is significantly stronger in the bulk case as compared to the vacancy cell. This holds even if the 1/108 part is subtracted from the bulk free energy which is necessary for calculating defect properties due to Eq. 3.26. The shown free energy corrections result in an increased hardening effect of bulk frequencies in comparison to the defect cell. This can also be interpreted as an effective softening due to the defect.

investigations are rare, probably also since it had been argued that the vacancy volume is nearly constant as a function of temperature [172]. This finding was confirmed by empirical potential calculations using the quasiharmonic approximation [187].

It is generally known that the vacancy volume at $T{=}0\,\mathrm{K}$ is smaller than the volume of the bulk atom. The calculated ratio is found to be similar for all crystal structures and is approximately $v^f/v^b \approx 0.7$ [174] where v^b represents the volume of a single atom in a perfect bulk cell and v^f the (excess) volume created due to the presence of a single vacancy. Having access to the full *ab initio* calculated thermodynamics of vacancy formation, the resulting temperature dependence of the volume of the defect v^f can be evaluated by using Eq. 3.26 on page 51. The numerically obtained result for the temperature-dependent vacancy volume of formation is shown in Fig. 4.14 for Al and Cu. When considering only the quasiharmonic result, a negligible effect is found with respect to the $T{=}0\,\mathrm{K}$ volume, similar to previous estimates [187]. Including the here calculated fully *ab initio* anharmonic contributions to vacancy formation, the excess volume increases significant by 20% for Al and 25% for Cu.

The increasing defect volume is due to a stronger expansion of the defect supercell in comparison to the bulk supercell. In Fig. 4.5 on page 64 a hardening of the bulk lattice has been found for LDA and GGA upon inclusion of anharmonic effects which, however, is not a contradiction. Anharmonic contributions lead to a hardening effect in both, bulk and defect supercell. This is shown in Fig. 4.15 for Al and Cu. It can be observed that the positive anharmonic free energy contribution to the bulk free energy (black) is larger compared to the correction for the defect supercell (red) which is smaller. Therefore, the hardening due to anharmonic phonon-phonon interactions is greater in the bulk as compared to the defect supercell. The resulting net effect is therefore a *softening* with

respect to the bulk supercell due to the introduction of the defect and leads in essence to an increase of the vacancy volume.

The *ab initio* calculated expansion of the defect volume shown in Fig. 4.14 is a difference between the corresponding defect and bulk volume. Applying the corresponding expansion for b^{defect} in Eq. 3.37 with bulk V_0 and γ values, approximate entropies of vacancy formation can be calculated.[4] The experimental Grüneisen parameters γ are considered, 2.16 for Al [26, 85, 86] and 2.0 for Cu [188, 189]. Resulting entropies of vacancy formation due to Eq. 3.35 at their corresponding melting temperature are 2.48 k_{B} and 2.94 k_{B} for Al and Cu respectively and therefore the correct order of magnitude in comparison to Fig. 4.13. In the LGT formulation the expansion of the defect volume is a critical quantity which directly influences the Gibbs energy as well as the entropy of defect formation. For defects where an atom is substituted by another atom the created defect volume — and the anharmonicity towards the defect — is smaller and the corresponding anharmonic effects could therefore be expected to be less crucial. Corresponding tests are necessary due to the findings of the significant anharmonic contributions for the vacancy.

---

[4]The calculated relative expansion ($b^{\mathrm{rel}} = \frac{V(T)}{V_0} - 1$) of the vacancy volume is 0.2 for Al and 0.25 for Cu (see Fig. 4.14). The corresponding *ab initio* derived bulk volumes v^b at $T{=}0\,\mathrm{K}$ are 16.02Å^3 for Al and 12.03Å^3 for Cu resulting in absolute b coefficients of 0.0034 Å^3/K for Al and 0.0022 Å^3/K for Cu.

Chapter 5

Summary and Outlook

The present thesis has addressed a major challenge of *ab initio* assisted materials design: The impact of the full spectrum of atomic vibrations — in particular the challenging phonon-phonon interactions — on the thermodynamic properties of a wide range of materials up to the melting temperature. Beyond the performed numerical assessments, a physically intuitive picture has been developed for the interpretation of anharmonic contributions. For bulk systems it was shown that the *correlated* motion of atoms breaks the symmetry of the harmonic potential which results in anharmonicity (see Fig. 3.1 on page 34). The concept of phonon-phonon interactions in fcc elements emerges mainly as a consequence of the anharmonic interactions between pairs of atoms. Defects were found to already break the *local* symmetry of the atomic positions which introduces strong anharmonic effects (see Fig. 3.8 on page 49). These effects were found to be responsible for the deviations from the textbook definition of the Arrhenius law.

The key findings of this thesis are summarized as follows:

1) *The Local Anharmonic (LA) approximation extends the quasiharmonic approach to capture anharmonic effects to meV accuracy for similar computational cost.*
   The discovery of a broken symmetry when considering correlated atomic motion was used to develop the Local Anharmonic approximation in Sec. 3.1.2 which relates the major part of anharmonic contributions to the natural picture of Morse-like pair interactions. It was shown that the new approach can be derived from a small set of $T=0\,\mathrm{K}$ calculations and goes far beyond the established quasiharmonic approximation for very similar computational cost. For the investigated wide range of fcc elements the nearest neighbor LA Hamiltonian was found to yield meV accuracy up to the melting temperature.

2) *Using the LA approximation to calculate numerically exact free energies results in a speed up of about two orders of magnitude in comparison to a harmonic reference for thermodynamic integration.*
   Based on the above mentioned approximate LA free energies, numerically exact free energies can be obtained by using the LA reference for thermodynamic integration to the full DFT potential energy surface. Harmonic potentials on the other hand describe a different phase space (see Fig. 3.1 on page 34) and can only be used with significantly lower efficiency as reference potentials for thermodynamic integration (see Fig. 3.6 on page 42). Corresponding benchmarks in Sec. 3.1.3 show that anharmonic references, and in particular the LA approximation, speed up thermodynamic integration significantly. The LA method opens therewith

the possibility to routinely study the full set of vibrational contributions completely from first principles and without the need to resort to approximative methods.

3) *Anharmonic contributions to thermodynamic properties are of the same order of magnitude as electronic and quasiharmonic contributions and should therefore not be neglected in quantitative assessments.*

   While for bulk aluminum anharmonic effects were previously found to be important [2], it was shown in this thesis that the corresponding contributions are actually even more dominant for most of the investigated bulk elements (see Secs. 4.1 and 4.3). Since fcc elements are usually expected to be only weakly anharmonic in comparison to more open systems as bcc, this result was surprising. Including anharmonic contributions to bulk thermodynamics not only reduces the discrepancy between theory and experiment (especially for the strongly anharmonic systems as Ag, Pt, Au and Si) but also the difference between LDA and GGA which was shown to be a reliable error measure (confidence interval) for *ab initio* evaluations. The reliability of the confidence interval is only consistently observed for all elements upon inclusion of anharmonic contributions. For the investigated bulk systems, anharmonic contributions to the heat capacity are up to 1.4 k_B for GGA and up to 0.6 k_B for LDA. It was shown in Fig. 4.6 on page 65 that anharmonic contributions are of the same order of magnitude as quasiharmonic or electronic contributions. Neglecting any of these contributions seems therefore arbitrary in thermodynamic assessments and would result in quantitative changes to the final results for many of the here considered systems. This is best observed in Fig. 4.4 on page 62 and in Secs. 4.2 and 4.3. The numerically exact evaluation of bulk anharmonic contributions using thermodynamic integration was key for assessing the accuracy of the LA approximation.

4) *The anharmonic contribution for a certain exchange and correlation functional is to first order dictated by the sampled volume range.*

   It was found in Sec. 4.1.1 that the anharmonic contribution is predominantly controlled by the sampled volume range. Therefore, anharmonic contributions are seen to be very similar for LDA and GGA at the same volume and the corresponding difference — at the same volume — is consequently small. It was shown in Sec. 4.2 that also differences between standard functionals (e.g. GGA) and advanced functionals (e.g. RPA) are small and can be treated by a perturbative approach as e.g. UP-TILD [10]. For the three most anharmonic fcc elements, corresponding $T=0\,\mathrm{K}$ RPA assessments show a unique agreement with experiment over the whole temperature range and the performed calculations promise a valuable approach for future first principles assessments of thermodynamic properties. The anharmonic contributions in gold are particularly significant (see Fig. 4.4 on page 62) and decisive to stabilize the heat capacity at elevated temperatures (see Sec. 4.2).

5) *Fully ab initio assessments of the heat capacity of the binary system Mg$_2$Si differ from predictions by the Neumann-Kopp rule.*

   For the binary system Mg$_2$Si, a fully temperature dependent *ab initio* assessment was performed. A significant anharmonic contribution has been found in particular for the unary constituent element Si. The Neumann-Kopp rule, which aims to predict multinary heat capacities from its unary constituents, shows only a qualitatively correct trend but fails in the quantitative prediction in comparison to the full *ab initio* assessment including all vibrational and electronic contributions. These limitations are necessary to consider in practical situations where the Neumann-Kopp rule is applied as e.g. in CALPHAD [6] assessments.

6) *The linear Arrhenius ansatz, $G^f = H^f - TS^f$, which is used to determine defect formation energies, has to be replaced by a Local Grüneisen Theory.*

   Anharmonic contributions turn out to be responsible for a strongly nonlinear vacancy formation energy. A qualitative explanation for this effect was given by the Local Grüneisen Theory. It was found in Sec. 3.2 that the atoms closest to the vacancy experience a very soft local potential towards the vacancy. It was also shown that the difference between an anharmonic system — e.g. an atom close to a defect — and a harmonic system — e.g. a atom in a bulk cell — results in a formation energy which is a nonlinear function of the temperature. Starting from these basic assumptions, the LGT not only predicts temperature dependent formation energies but also a formation entropy which increases linearly with temperature. The performed numerical calculations in Sec. 4.4.3 support this picture showing consistently a very linear mono-vacancy formation entropy and corresponding temperature dependent formation energies. With the finding of a temperature dependent vacancy formation energy in Al and Cu, it is now possible to consolidate all experimental measurements (PAS and DD) at high temperatures with theoretical *ab initio* assessments of vacancy formation energies over the whole temperature range.

7) *In contrast to some experimental interpretations of vacancy concentration measurements in Al and Cu, divacancies are found only in negligible concentrations. They can be therefore excluded as a source for the experimentally observed non-Arrhenius behavior.*

   The numerical calculations in Sec. 4.4.2 did conclusively show that divacancy concentrations are negligible in Al and Cu. This finding allowed to settle a long controversy in which divacancies were supposed to be present in notable concentrations in Al and Cu and to be responsible for the temperature dependence in the vacancy formation energies of Al and Cu (see Fig. 4.10 on page 75, discussion in Sec. 4.4.2 and Table 4.2).

8) *Experimental vacancy formation energies as collected in the Landolt-Bornstein series can be in error by ∼20% due to a linear extrapolation from high temperature data and need to be corrected. Previously introduced concepts such as surface corrections or the AM05 functional need to be revisited.*

   Vacancy concentrations and formation energies are typically extrapolated from high temperatures using the linear Arrhenius law. The here performed numerical assessments found, in contrast, a strongly temperature dependent vacancy formation energy. As has been discussed in Sec. 4.4.4, this has important consequences: a) It can lead to a severe overestimation of vacancy formation energies. Hence, a reevaluation of established point defect data as e.g. collected in the Landolt-Bornstein series becomes critical. b) Approximations which make use of previously linear extrapolated data have to be revisited. This includes concepts such as surface corrections [152, 177] and the AM05 functional [181] which introduces energy corrections which have been justified by benchmarking against Arrhenius extrapolated $T=0\,\mathrm{K}$ vacancy formation enthalpy data [68]. Recently performed highly accurate $T=0\,\mathrm{K}$ calculations on vacancy formation by QMC [164] and HSE [126] on the other hand — which beforehand showed discrepancies in comparison to Arrhenius extrapolated data — can now be consistently interpreted by LGT extrapolated formation energies.

The developed methods, results and insights gained in this study are expected to provide a firm basis for an accurate description of atomic vibration in solids — both, for bulk and defect systems. It was shown that realistic calculations of materials properties at high temperatures require free energies with an accuracy of a few meV/atom for bulk and a sub meV/atom for defect systems.

New and improved methods which further increase the accessible accuracy, broaden the application range for reasonable computational cost will likely become key for future materials design. It is plausible to assume that thermodynamic integration will stay indispensable also for the assessment of future methods since it provides an access to the numerically exact potential energy surface and is thus the ultimate benchmark. Its efficiency however will always be dictated by the performance of the reference system. The next critical points which have to be addressed in the direction for routine, efficient and accurate first principles descriptions of the atomic motion are:

- The introduced LA methods includes up to now only first-neighbor interactions. It was shown that second-neighbor interactions are strong for the elements with the most significant deviations from the exact free energies surface. An extension to second and possibly further neighbors seems natural and should be investigated. Those tests are also important to assess the accuracy of a simple pair potential model in general. The extension to anharmonic many-body interactions might prove a further possible route.

- Only fcc systems were investigated with the LA method. To broaden its applicability range it is critical to perform similar investigations in bcc, for alloy systems and also for defects. In case the currently found LA level of accuracy is found for a wide range of material properties, LA Hamiltonians could serve as new EAM like potentials for the study of material properties in large systems.

- First encouraging results have been found by investigating spectrally resolved anharmonic properties as the phonon line width using an LA potential for Al (see final paragraph of Sec. 3.1.2). This route seems promising also in comparison to many-body perturbative approaches which have proved computationally very demanding due to the unfavorabe scaling of many-body interactions (see Sec. 2.4.1). A great benefit is seen by comparing theoretical concepts to highly accurate experimental phonon lifetime data which can only profit both fields.

- The accuracy of every *ab initio* descriptions at elevated temperatures is inherently connected to the performance of the considered xc functional at $T=0\,\mathrm{K}$. A balance needs to be found between the computational demands at $T=0\,\mathrm{K}$ and finite temperatures. Using novel xc functionals such as RPA to parametrize a LA Hamiltonian at $T=0\,\mathrm{K}$ could serve as a unique way to access the corresponding high temperature phase space accurately for minimal computational cost since expensive molecular dynamics can be avoided.

Progress in these topics will advance the field of solid state theory, likely improve our understanding of solids and therewith unfold new and exciting routes in computational materials design.

Appendix A

Supplement

A.1 Rewriting the quasiharmonic total energy

The original equation for the harmonic energy is readily defined by

$$E^{\text{harm}} = \frac{1}{2} \sum_{ij}^{3N} u_i \Phi_{ij} u_j, \tag{A.1}$$

where N is the number of atoms, Φ_{ij} is the force constant matrix and $u_i = R_i - R_i^{\text{eq}}$ and $R_i(R_i^{\text{eq}})$ is the (equilibrium) atomic position. We now split Eq. (2.62) in the trace plus the traceless remainder:

$$E^{\text{harm}} = \frac{1}{2} \left(\sum_{i}^{3N} u_i \Phi_{ii} u_i \; + \; \sum_{i,j\neq i}^{3N} u_i \Phi_{ij} u_j \right). \tag{A.2}$$

Since the sum of forces has always to be zero (Newton's third law) when displacing an atom in direction i, the restoring forces on the displaced atom — which is always found in the diagonal of the force constant matrix and therefore $i = j$ — have to be equal to the sum of forces on all other atoms. This corresponds to using for the trace the property

$$\Phi_{ii} = -\sum_{j\neq i}^{3N} \Phi_{ij}, \tag{A.3}$$

we obtain

$$E^{\text{harm}} = \frac{1}{2} \left(-\sum_{i,j\neq i}^{3N} u_i \Phi_{ij} u_i \; + \; \sum_{i,j\neq i}^{3N} u_i \Phi_{ij} u_j \right). \tag{A.4}$$

Now we split each sum into an upper triangular and a lower triangular sum as

$$E^{\text{harm}} = \frac{1}{2} \left(-\sum_{i,j>i}^{3N} u_i \Phi_{ij} u_i \; - \; \sum_{i,j<i}^{3N} u_i \Phi_{ij} u_i \; + \; \sum_{i,j>i}^{3N} u_i \Phi_{ij} u_j \; + \; \sum_{i,j<i}^{3N} u_i \Phi_{ij} u_j \right), \tag{A.5}$$

and combine the first and third, and second and fourth sum as

$$E^{\mathrm{harm}} = \frac{1}{2} \left(\sum_{i,j>i}^{3N} u_i \Phi_{ij}(u_j - u_i) + \sum_{i,j<i}^{3N} u_i \Phi_{ij}(u_j - u_i) \right). \tag{A.6}$$

Changing dummy indices in the second sum we have

$$E^{\mathrm{harm}} = \frac{1}{2} \left(\sum_{i,j>i}^{3N} u_i \Phi_{ij}(u_j - u_i) + \sum_{i,j>i}^{3N} u_j \Phi_{ji}(u_i - u_j) \right), \tag{A.7}$$

which we can rewrite using the symmetry property of the force constant matrix $\Phi_{ij} = \Phi_{ji}$ (a partial differentiation is commutative) as

$$E^{\mathrm{harm}} = \frac{1}{2} \left(\sum_{i,j>i}^{3N} u_i \Phi_{ij}(u_j - u_i) + \sum_{i,j>i}^{3N} u_j \Phi_{ij}(u_i - u_j) \right), \tag{A.8}$$

allowing to join the sums as

$$
\begin{aligned}
E^{\mathrm{harm}} &= \frac{1}{2} \left(\sum_{i,j>i}^{3N} u_i \Phi_{ij}(u_j - u_i) - \sum_{i,j>i}^{3N} u_j \Phi_{ij}(u_j - u_i) \right) \\
&= -\frac{1}{2} \left(\sum_{i,j>i}^{3N} (u_j - u_i) \Phi_{ij}(u_j - u_i) \right) \\
&= -\frac{1}{2} \left(\sum_{i,j>i}^{3N} \Phi_{ij}(u_j - u_i)^2 \right) = -\frac{1}{2} \left(\sum_{i,j>i}^{3N} \Phi_{ij}(d_{ji} - d_{ji}^{\mathrm{eq}})^2 \right),
\end{aligned} \tag{A.9}
$$

with $d_{ji} = R_j - R_i$ and $d_{ji}^{\mathrm{eq}} = R_j^{\mathrm{eq}} - R_i^{\mathrm{eq}}$. Here

$$
\begin{aligned}
u_j - u_i &= R_j - R_j^{\mathrm{eq}} - R_i + R_i^{\mathrm{eq}} \\
&= R_j - R_i - (R_j^{\mathrm{eq}} - R_i^{\mathrm{eq}}) \\
&= d_{ij} - d_{ij}^{\mathrm{eq}}
\end{aligned} \tag{A.10}
$$

It can be therefore summarized

$$\boxed{E^{\mathrm{harm}} = \frac{1}{2} \sum_{ij}^{3N} u_i \Phi_{ij} u_j = -\frac{1}{2} \left(\sum_{i,j>i}^{3N} \Phi_{ij}(d_{ji} - d_{ji}^{\mathrm{eq}})^2 \right)} \tag{A.11}$$

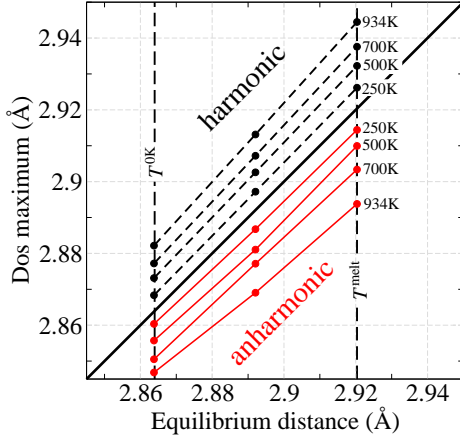## A.2   Local Anharmonic approximation

Figure A.1: Maximum of first neighbor distribution function (dos) of the quasiharmonic (dashed line) and DFT (full line) MD for Al at different temperatures. The center of mass for both distributions — in contrast to the dos maximum — is always at the equilibrium distance. For a harmonic potential, an increase is observed for the nearest neighbor dos maximum due to transversal motion of the atomic positions. For the anharmonic potential the DOS maximum is observed to shift to smaller distances since the distribution is non-symmetric and the center of mass is at the exact equilibrium position (for both distributions).

A.3   Details of calculations on bulk systems
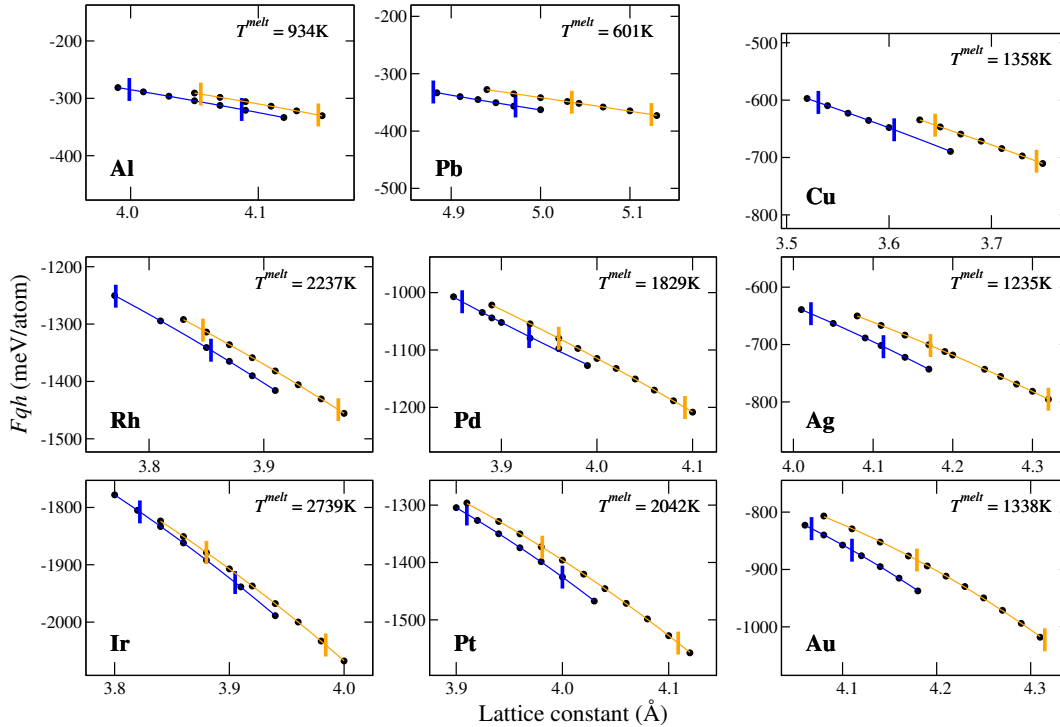
Figure A.2: Quasiharmonic Helmholtz free energy at the melting point as a function of lattice constant for GGA (orange) and LDA (blue). Dots mark the explicitly calculated volumes. The corresponding fits are taken from the full free energy surface and it is found that a th. Vertical lines mark the $T=0$ K and respective T^{melt} volume for the considered functional.
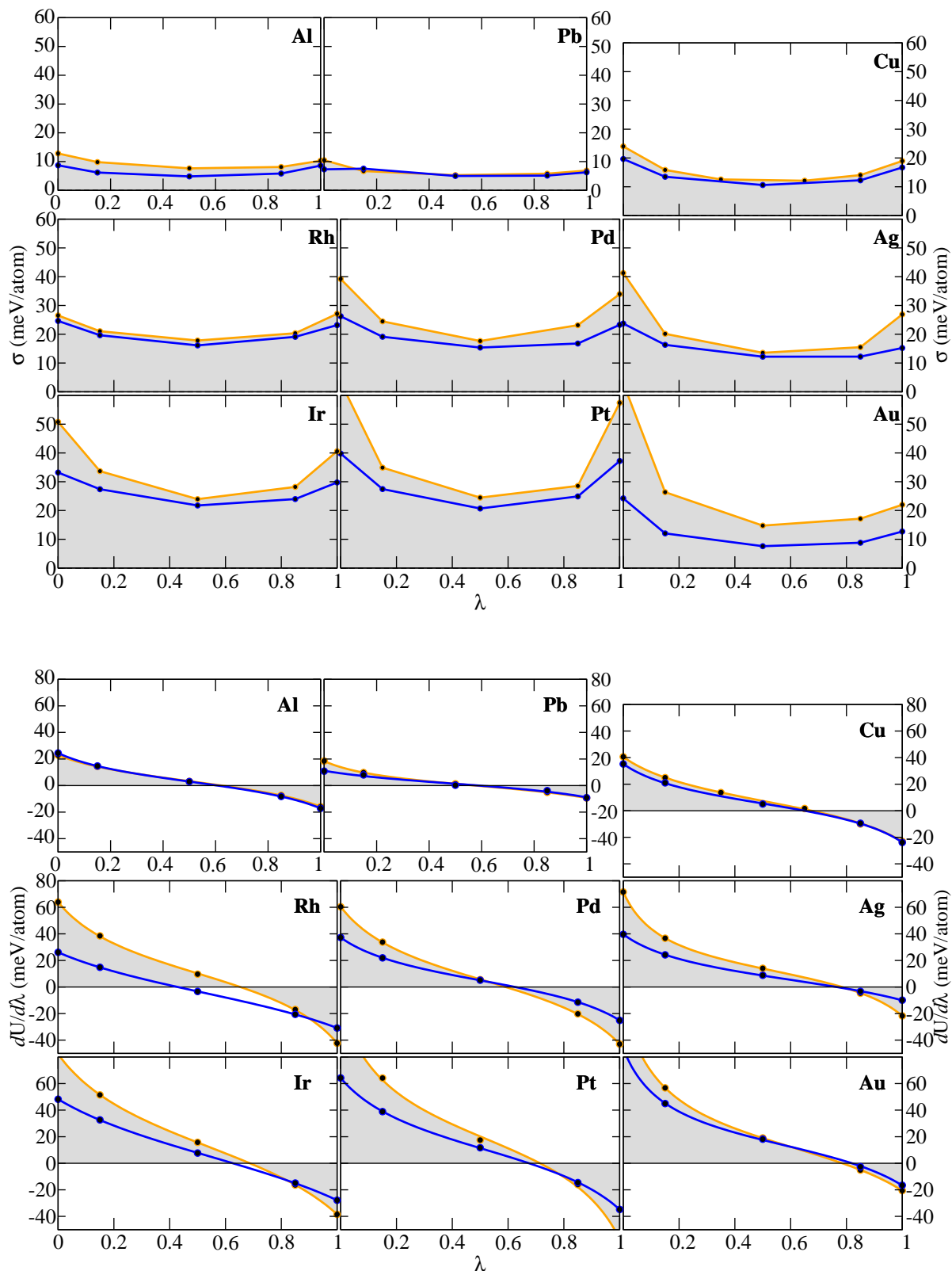
Figure A.3: (a) Standard deviation σ of the quasiharmonic *ab initio* computed reference for unary fcc metals (Al, Ag, Au, Cu, Ir, Ni, Pb, Pd, Pt, Rh) as function of coupling constant λ. The standard deviation is shown at the respective melting temperature and volume for GGA (orange) and LDA (blue). (b) $dU/d\lambda$ corresponding to MD runs in (a).

Bibliography

[1] D. Alfè, G. Price, and M. J. Gillan, Phys. Rev. B **64**, 045123 (2001), ISSN 0163-1829, URL http://link.aps.org/doi/10.1103/PhysRevB.64.045123.

[2] B. Grabowski, L. Ismer, T. Hickel, and J. Neugebauer, Phys. Rev. B **79**, 134106 (2009), ISSN 1098-0121, URL http://link.aps.org/doi/10.1103/PhysRevB.79.134106.

[3] C. Engin, L. Sandoval, and H. M. Urbassek, Model. Simul. Mater. Sci. Eng. **16**, 035005 (2008), ISSN 0965-0393, URL http://stacks.iop.org/0965-0393/16/i=3/a=035005?key=crossref.acc64bb1aa8099b38cfd6d9b96b2a779.

[4] J. E. Turney, E. S. Landry, a. J. H. McGaughey, and C. H. Amon, Phys. Rev. B **79**, 064301 (2009), ISSN 1098-0121, URL http://link.aps.org/doi/10.1103/PhysRevB.79.064301.

[5] M. C. Payne, M. P. Teter, D. C. Allan, T. a. Arias, and J. D. Joannopoulos, Rev. Mod. Phys. **64**, 1045 (1992), ISSN 00346861, URL http://journals.aps.org/rmp/abstract/10.1103/RevModPhys.64.1045.

[6] A. Dinsdale, Calphad **15**, 317 (1991), ISSN 03645916, URL http://www.sciencedirect.com/science/article/pii/036459169190030N.

[7] M. S. Daw and M. I. Baskes, Phys. Rev. B **29**, 6443 (1984), ISSN 01631829, URL http://journals.aps.org/prb/abstract/10.1103/PhysRevB.29.6443.

[8] M. S. Daw, S. M. Foiles, and M. I. Baskes, Mater. Sci. Reports **9**, 251 (1993), ISSN 09202307, URL http://www.sciencedirect.com/science/article/pii/092023079390001U.

[9] L. Vočadlo and D. Alfè, Phys. Rev. B **65**, 214105 (2002), ISSN 0163-1829, URL http://link.aps.org/doi/10.1103/PhysRevB.65.214105.

[10] B. Grabowski, Ph.D. thesis, Paderborn (2009), URL http://nbn-resolving.de/urn:nbn:de:hbz:466-20091216018.

[11] B. Grabowski, T. Hickel, and J. Neugebauer, Phys. Rev. B **76**, 024309 (2007), ISSN 1098-0121, URL http://link.aps.org/doi/10.1103/PhysRevB.76.024309.

[12] D. Frenkel and B. Smit, *Understanding Molecular Simulation: From Algorithms to Applications*, Academic Press (Academic Press, 2002), ISBN 9780122673511, URL http://books.google.de/books?id=XmyO2oRUg0cC.

[13] M. Born and R. Oppenheimer, Ann. Phys. **20**, 457 (1927), ISSN 00033804, URL http://onlinelibrary.wiley.com/doi/10.1002/andp.19273892002/abstract.

[14] D. Marx and J. Hutter, *Ab initio molecular dynamics: Theory and implementation*, vol. 1 (John von Neumann Institute for Computing, 2000), ISBN 3000056181, URL http://134.94.100.198/nic-series/Volume3/marx.ps.

[15] K. Capelle, Brazilian J. Phys. **36**, 69 (2006), ISSN 0103-9733, 0211443, URL http://www.scielo.br/scielo.php?script=sci_arttext&pid=S0103-97332006000700035.

[16] P. Hohenberg and W. Kohn, Phys. Rev. **136**, 1912 (1964), ISSN 01631829, URL http://journals.aps.org/pr/abstract/10.1103/PhysRev.136.B864.

[17] W. Kohn and L. J. Sham, Phys. Rev. **140**, A1133 (1965), ISSN 0031899X, URL http://link.aps.org/doi/10.1103/PhysRev.140.A1133.

[18] D. M. Ceperley and B. J. Alder, Phys. Rev. Lett. **45**, 566 (1980), ISSN 0031-9007, URL http://link.aps.org/doi/10.1103/PhysRevLett.45.566.

[19] J. P. Perdew and A. Zunger, Phys. Rev. B **23**, 5048 (1981), ISSN 0163-1829, URL http://link.aps.org/doi/10.1103/PhysRevB.23.5048.

[20] J. P. Perdew, K. Burke, and M. Ernzerhof, Phys. Rev. Lett. **77**, 3865 (1996), ISSN 0031-9007, URL http://link.aps.org/doi/10.1103/PhysRevLett.77.3865.

[21] A. Einstein, Ann. Phys. **22**, 180 (1906), URL http://onlinelibrary.wiley.com/doi/10.1002/andp.19063270110/abstract.

[22] D. C. Wallace, *Thermodynamics of Crystals*, Dover books on physics (Dover Publications, New York, 1998), ISBN 9780486402123, URL http://books.google.se/books?id=qLzOmwSgMIsC.

[23] P. Debye, Ann. Phys. **344**, 789 (1912), ISSN 00033804, URL http://onlinelibrary.wiley.com/doi/10.1002/andp.19123441404/abstract.

[24] K. Esfarjani, *Phonons and lattice dynamics*, URL http://rci.rutgers.edu/~ke116/Teaching_files/phonons.pdf.

[25] M. de Podesta, *Understanding the Properties of Matter* (CRC Press, 2002), ISBN 0415257883, URL https://books.google.com/books?hl=en&lr=&id=ya-4enCDoWQC&pgis=1.

[26] E. Grüneisen, Ann. Phys. **344**, 257 (1912), ISSN 00033804, URL http://doi.wiley.com/10.1002/andp.19123441202.

[27] K. Parlinski, Z. Li, and Y. Kawazoe, Phys. Rev. Lett. **78**, 4063 (1997), URL http://link.aps.org/doi/10.1103/PhysRevLett.78.4063.

[28] K. Kunc and R. M. Martin, Phys. Rev. Lett. **48**, 406 (1982), URL http://journals.aps.org/prl/abstract/10.1103/PhysRevLett.48.406.

[29] D. Alfe, G. De Wijs, G. Kresse, and M. J. Gillan, **77**, 871 (2000), ISSN 00207608, URL http://discovery.ucl.ac.uk/79564/.

[30] S. Baroni, S. De Gironcoli, A. Dal Corso, and P. Giannozzi, Rev. Mod. Phys. **73**, 515 (2001), ISSN 00346861, 0012092v1, URL http://journals.aps.org/rmp/pdf/10.1103/RevModPhys.73.515.

[31] P. Giannozzi, S. de Gironcoli, P. Pavone, and S. Baroni, Phys. Rev. B **43**, 7231 (1991), ISSN 0163-1829, URL http://prb.aps.org/abstract/PRB/v43/i9/p7231_1.

[32] D. Alfè, Comput. Phys. Commun. **180**, 2622 (2009), ISSN 00104655, URL http://linkinghub.elsevier.com/retrieve/pii/S0010465509001064.

[33] A. Glensk, B. Grabowski, T. Hickel, and J. Neugebauer, Phys. Rev. Lett. **114**, 1 (2015), ISSN 0031-9007, URL http://link.aps.org/doi/10.1103/PhysRevLett.114.195901.

[34] P. Souvatzis, O. Eriksson, M. Katsnelson, and S. Rudin, Phys. Rev. Lett. **100**, 095901 (2008), ISSN 0031-9007, URL http://link.aps.org/doi/10.1103/PhysRevLett.100.095901.

[35] P. Souvatzis, O. Eriksson, M. Katsnelson, and S. Rudin, Comput. Mater. Sci. **44**, 888 (2009), ISSN 09270256, URL http://linkinghub.elsevier.com/retrieve/pii/S0927025608003121.

[36] O. Hellman, P. Steneteg, I. A. Abrikosov, and S. I. Simak, Phys. Rev. B **87**, 104111 (2013), ISSN 1098-0121, URL http://link.aps.org/doi/10.1103/PhysRevB.87.104111.

[37] R. A. Cowley, Reports Prog. Phys. **31**, 123 (1968), ISSN 00344885, URL http://stacks.iop.org/0034-4885/31/i=1/a=303?key=crossref.d5a492bfe55cfa133e149255d03d79c9.

[38] K. Esfarjani and H. T. Stokes, Phys. Rev. B - Condens. Matter Mater. Phys. **77**, 1 (2008), ISSN 10980121, URL http://journals.aps.org/prb/abstract/10.1103/PhysRevB.77.144112.

[39] F. Zhou, W. Nielson, Y. Xia, and V. Ozoliňš, Phys. Rev. Lett. **113**, 185501 (2014), ISSN 0031-9007, URL http://link.aps.org/doi/10.1103/PhysRevLett.113.185501.

[40] Y. Chen, X. Ai, and C. A. Marianetti, Phys. Rev. Lett. **113**, 105501 (2014), URL http://journals.aps.org/prl/abstract/10.1103/PhysRevLett.113.105501.

[41] X. Tang and B. Fultz, Phys. Rev. B **84**, 054303 (2011), ISSN 1098-0121, URL http://link.aps.org/doi/10.1103/PhysRevB.84.054303.

[42] J. Sanchez, F. Ducastelle, and D. Gratias, Phys. A Stat. Mech. its Appl. **128**, 334 (1984), ISSN 03784371, URL http://www.sciencedirect.com/science/article/pii/0378437184900967.

[43] J. C. Thomas and A. VanderVen, Phys. Rev. B **88**, 214111 (2013), ISSN 1098-0121, URL http://link.aps.org/doi/10.1103/PhysRevB.88.214111.

[44] X. Ai, Y. Chen, and C. A. Marianetti, Phys. Rev. B **90**, 014308 (2014), ISSN 1098-0121, URL http://link.aps.org/doi/10.1103/PhysRevB.90.014308.

[45] G. Gilat, *Vibrational Properties of Solids* (Elsevier Science, 1976), ISBN 9780323150088, URL https://books.google.de/books?id=q_hQ_XR4u78C&printsec=frontcover&source=gbs_ge_summary_r&cad=0#v=onepage&q&f=false.

[46] G. J. Ackland, J. Phys. Condens. Matter **14**, 2975 (2002), ISSN 0953-8984, URL http://iopscience.iop.org/0953-8984/14/11/311.

[47] B. Grabowski, P. Söderlind, T. Hickel, and J. Neugebauer, Phys. Rev. B **84**, 214107 (2011), ISSN 1098-0121, URL http://link.aps.org/doi/10.1103/PhysRevB.84.214107.

[48] J. Dugdale and D. MacDonald, Phys. Rev. **1034** (1954), URL http://prola.aps.org/abstract/PR/v96/i1/p57_1.

[49] O. Delaire, J. Ma, K. Marty, A. F. May, M. A. McGuire, M.-h. Du, D. J. Singh, A. Podlesnyak, G. Ehlers, M. D. Lumsden, et al., Nat. Mater. **10**, 614 (2011), ISSN 1476-1122, URL http://www.nature.com/nmat/journal/v10/n8/full/nmat3035.html?WT.ec_id=NMAT-201108.

[50] R. Najafabadi and D. J. Srolovitz, Phys. Rev. B **52**, 9229 (1995), ISSN 0163-1829, URL http://link.aps.org/doi/10.1103/PhysRevB.52.9229.

[51] V. Ozoliņš, Phys. Rev. Lett. **102**, 065702 (2009), ISSN 0031-9007, URL http://link.aps.org/doi/10.1103/PhysRevLett.102.065702.

[52] A. P. Bartók, M. C. Payne, R. Kondor, and G. Csányi, Phys. Rev. Lett. **104**, 136403 (2010), ISSN 0031-9007, URL http://link.aps.org/doi/10.1103/PhysRevLett.104.136403.

[53] C. Cazorla, D. Alfè, and M. J. Gillan, Phys. Rev. B **85**, 1 (2012), ISSN 10980121, 1105.0644, URL link.aps.org/doi/10.1103/PhysRevB.85.064113.

[54] N. W. Ashcroft and N. D. Mermin, *Solid State Physics* (Holt, Rinehart and Winston, 1976), hrw intern ed., ISBN 9780030839931, URL http://books.google.de/books?id=1C9HAQAAIAAJ.

[55] X. Zhou, J. Zimmerman, B. Wong, and J. Hoyt, J. Mater. Res. **23**, 704 (2008), ISSN 0884-2914, URL journals.cambridge.org/article_S0884291400028016.

[56] A. Björck, Linear Algebra Appl. **197-198**, 297 (1994), ISSN 00243795, URL http://www.sciencedirect.com/science/article/pii/0024379594904936.

[57] K. Pearson, *Notes on regression and inheritance in the case of two parents* (Taylor & Francis, 1895), URL http://books.google.de/books?id=60aL0zlT-90C.

[58] S. Plimpton, J. Comp. Phys. **117**, 1 (1995), ISSN 0021-9991, URL http://www.sciencedirect.com/science/article/B6WHY-45NJN1B-3N/2/58aa2a309d2ebbbe60e0f417d398b0ef.

[59] X. Tang, C. W. Li, and B. Fultz, Phys. Rev. B **82**, 184301 (2010), ISSN 1098-0121, URL http://link.aps.org/doi/10.1103/PhysRevB.82.184301.

[60] R. Stedman and G. Nilsson, Phys. Rev. **145**, 492 (1966), ISSN 0031899X, URL http://journals.aps.org/pr/abstract/10.1103/PhysRev.145.492.

[61] Y. Kraftmakher, Phys. Rep. **299**, 79 (1998), ISSN 03701573, URL http://www.sciencedirect.com/science/article/pii/S0370157397000823.

[62] M. Mantina, Y. Wang, R. Arroyave, L. Chen, Z. Liu, and C. Wolverton, Phys. Rev. Lett. **100**, 215901 (2008), ISSN 0031-9007, URL http://link.aps.org/doi/10.1103/PhysRevLett.100.215901.

[63] D. Andersson and S. Simak, Phys. Rev. B **70**, 115108 (2004), ISSN 1098-0121, URL http://link.aps.org/doi/10.1103/PhysRevB.70.115108.

[64] A. Khellaf, A. Seeger, and R. M. Emrick, Mater. Trans. **43**, 186 (2002), URL http://www.jim.or.jp/journal/e/pdf3/43/02/186.pdf.

[65] M. de Koning and A. Antonelli, Phys. Rev. B **55**, 735 (1997), ISSN 0163-1829, URL http://link.aps.org/doi/10.1103/PhysRevB.55.735.

[66] R. Simmons and R. W. Balluffi, Phys. Rev. **125**, 862 (1962), ISSN 0031-899X, URL http://link.aps.org/doi/10.1103/PhysRev.125.862.

[67] R. Hatcher, R. Zeller, and P. Dederichs, Phys. Rev. B **19**, 5083 (1979), ISSN 0163-1829, URL http://link.aps.org/doi/10.1103/PhysRevB.19.5083.

[68] A. Glensk, B. Grabowski, T. Hickel, and J. Neugebauer, Phys. Rev. X **4**, 011018 (2014), ISSN 2160-3308, URL http://link.aps.org/doi/10.1103/PhysRevX.4.011018.

[69] L. M. Levinson and F. R. N. Nabarro, Acta Metall. **15**, 785 (1967), ISSN 00016160, URL http://www.sciencedirect.com/science/article/pii/0001616067903598.

[70] P. Wilkes, *Solid State Theory in Metallurgy* (University Press, 1973), ISBN 9780521096997, URL http://books.google.de/books?id=Ru43AAAAIAAJ.

[71] J. Mundy, Phys. Rev. B **3**, 2431 (1971), URL http://journals.aps.org/prb/abstract/10.1103/PhysRevB.3.2431.

[72] J. N. Mundy, T. E. Miller, and R. J. Porte, Phys. Rev. B **3**, 2445 (1971), ISSN 01631829, URL http://journals.aps.org/prb/abstract/10.1103/PhysRevB.3.2445.

[73] S. J. Rothman, N. L. Peterson, and J. T. Robinson, Phys. Status Solidi **39**, 635 (1970), ISSN 03701972, URL http://doi.wiley.com/10.1002/pssb.19700390231.

[74] J. Pelleg, Philos. Mag. **29**, 383 (1974), ISSN 0031-8086, URL http://www.tandfonline.com/doi/abs/10.1080/14786437408213279.

[75] J. Murdock and C. McHargue, Acta Metall. **16**, 493 (1968), ISSN 00016160, URL http://www.sciencedirect.com/science/article/pii/0001616068901235.

[76] G. V. Kidson, Can. J. Phys. **41**, 1563 (1963), ISSN 0008-4204, URL http://www.nrcresearchpress.com/doi/abs/10.1139/p63-159#.VVi2k5Oqqko.

[77] J. Murdock, T. Lundy, and E. Stansbury, Acta Metall. **12**, 1033 (1964), ISSN 00016160, URL http://www.sciencedirect.com/science/article/pii/0001616064900756.

[78] G. B. Gibbs, D. Graham, and D. H. Tomlin, Philos. Mag. **8**, 1269 (1963), ISSN 0031-8086, URL http://www.tandfonline.com/doi/abs/10.1080/14786436308207292.

[79] J. Askill and G. B. Gibbs, Phys. status solidi **11**, 557 (1965), ISSN 03701972, URL http://doi.wiley.com/10.1002/pssb.19650110207.

[80] J. Horváth, F. Dyment, and H. Mehrer, J. Nucl. Mater. **126**, 206 (1984), ISSN 00223115, URL http://www.sciencedirect.com/science/article/pii/0022311584900308.

[81] T. Hehenkamp, J. Phys. Chem. Solids **55**, 907 (1994), ISSN 00223697, URL http://linkinghub.elsevier.com/retrieve/pii/0022369794901104.

[82] G. Neumann, V. Tölle, and C. Tuijn, Phys. B Condens. Matter **271**, 21 (1999), ISSN 09214526, URL http://www.sciencedirect.com/science/article/pii/S0921452699002094.

[83] H. M. Gilder and D. Lazarus, Phys. Rev. B **11**, 4916 (1975), ISSN 0556-2805, URL http://link.aps.org/doi/10.1103/PhysRevB.11.4916.

[84] a. Karasevskii and V. Lubashenko, Phys. Rev. B **71**, 012107 (2005), ISSN 1098-0121, URL http://link.aps.org/doi/10.1103/PhysRevB.71.012107.

[85] P. Harris, U.S. Army Picatinny Arsenal p. 36 (1972), URL http://www.dtic.mil/dtic/tr/fulltext/u2/751130.pdf.

[86] S. Prakash and S. Joshi, Physica **47**, 452 (1970), ISSN 00318914, URL http://www.sciencedirect.com/science/article/pii/0031891470902764.

[87] D. H. Huang, X. R. Liu, L. Su, C. G. Shao, R. Jia, and S. M. Hong, J. Phys. D. Appl. Phys. **40**, 5327 (2007), ISSN 0022-3727, URL http://stacks.iop.org/0022-3727/40/i=17/a=047?key=crossref.4f9b127e370ab26f268effec2273c1dd.

[88] M. Pozzo, C. Davies, D. Gubbins, and D. Alfè, Nature **485**, 355 (2012), ISSN 1476-4687, URL http://www.ncbi.nlm.nih.gov/pubmed/22495307.

[89] G. Grimvall, B. Magyari-Köpe, V. Ozoliņš, and K. A. Persson, Rev. Mod. Phys. **84**, 945 (2012), ISSN 0034-6861, URL http://link.aps.org/doi/10.1103/RevModPhys.84.945.

[90] A. Dinsdale, Calphad **15**, 317 (1991), ISSN 03645916, URL http://linkinghub.elsevier.com/retrieve/pii/036459169190030N.

[91] M. Schick, B. Hallstedt, A. Glensk, B. Grabowski, T. Hickel, M. Hampl, J. Gröbner, J. Neugebauer, and R. Schmid-Fetzer, Calphad **37**, 77 (2012), ISSN 03645916, URL http://linkinghub.elsevier.com/retrieve/pii/S0364591612000181.

[92] J. Rogal, S. V. Divinski, M. W. Finnis, A. Glensk, J. Neugebauer, J. H. Perepezko, S. Schuwalow, M. H. F. Sluiter, and B. Sundman, Phys. Status Solidi **251**, 97 (2014), ISSN 03701972, URL http://doi.wiley.com/10.1002/pssb.201350155.

[93] G. K. Horton, Am. J. Phys. **36**, 93 (1968), ISSN 00029505, URL http://link.aip.org/link/?AJP/36/93/1&Agg=doi.

[94] H. J. Schirlitzki, Zeitschrift für Phys. **246**, 363 (1971), ISSN 14346001, URL http://link.springer.com/article/10.1007/BF01395737.

[95] T. Pochapsky, Acta Metall. **1**, 747 (1953), ISSN 00016160, URL http://www.sciencedirect.com/science/article/pii/0001616053900340.

[96] C. Brooks and R. Bingham, J. Phys. Chem. Solids **29**, 1553 (1968), URL http://www.sciencedirect.com/science/article/pii/0022369768900978.

[97] D. a. Ditmars, C. a. Plint, and R. C. Shukla, Int. J. Thermophys. **6**, 499 (1985), ISSN 0195928X, URL http://link.springer.com/article/10.1007/BF00508893.

[98] R. A. McDonald, J. Chem. Eng. Data **12**, 115 (1967), ISSN 0021-9568, URL http://pubs.acs.org/cgi-bin/doilookup/?10.1021/je60032a037.

[99] a. J. Leadbetter, J. Phys. C Solid State Phys. **1**, 1481 (1968), ISSN 00223719, URL http://iopscience.iop.org/0022-3719/1/6/304.

[100] U. Schmidt, O. Vollmer, and R. Kohlhaas, Z. Naturforsch. **25A**, 1258 (1970), URL http://www.znaturforsch.com/conts.htm.

[101] P. D. Desai, Int. J. Thermophys. **8**, 621 (1987), ISSN 0195928X, URL http://link.springer.com/article/10.1007/BF00503647.

[102] Y. Takahashi, T. Azumi, and Y. Sekine, Thermochim. Acta **139**, 133 (1989), ISSN 00406031, URL http://www.sciencedirect.com/science/article/pii/0040603189870169.

[103] W. Kramer and J. Nölting, Acta Metall. **20**, 1353 (1972), ISSN 00016160, URL http://linkinghub.elsevier.com/retrieve/pii/0001616072900703.

[104] J. Arblaster, Calphad **39**, 47 (2012), ISSN 03645916, URL http://dx.doi.org/10.1016/j.calphad.2012.08.004.

[105] Y. S. Touloukian, R. K. Kirby, R. E. Taylor, and P. D. Desai, *Thermal expansion: Metallic elements and alloys.* (Springer, New York, 1975), URL http://ntrs.nasa.gov/search.jsp?R=19760059083.

[106] J. Booker, R. Paine, and J. Stonehouse, WADD Tech. Rep. TR 60-889 pp. 1–133 (1961), URL http://www.dtic.mil/cgi-bin/GetTRDoc?Location=U2&doc=GetTRDoc.pdf&AD=AD0265625.

[107] C. Lucks and W. Deem, WADC TR 55-496; AD 97185; pp. 1–65 (1956), URL http://contrails.iit.edu/resources/BiblioGraphySearch3.asp?lineNumber=133.

[108] D. L. Martin, Can. J. Phys. **38**, 17 (1960), ISSN 0008-4204, URL http://www.nrcresearchpress.com/doi/pdf/10.1139/p60-003.

[109] Lyusternik V. E., Fiz. Met. i Met. **7** (1959), URL http://www.osti.gov/scitech/biblio/4210516.

[110] Butler and Inn, Tech. Rep., Naval Radiological Defense Lab., San Francisco (1959), URL http://www.osti.gov/scitech/biblio/4330807.

[111] R. Pawel and E. Stansbury, Solid State Commun. **2**, viii (1964), ISSN 00381098, URL http://www.sciencedirect.com/science/article/pii/0022369765901368.

[112] I.B. Fieldhouse, J.C. Hedge, J. Lang, A. Takata, and T. Waterman, WADC TR 55-495 Part 1 pp. 55–495 (1956), URL http://contrails.iit.edu/resources/BiblioGraphySearch3.asp?lineNumber=133.

[113] F. M. Jaeger and E. Rosenbohm, Prok. K. Akad. Wet. **36**, 291 (1933), URL http://www.dwc.knaw.nl/DL/publications/PU00016482.pdf.

[114] E. D. Eastman, A. M. Williams, and T. F. Young, J. Am. Chem. Soc. **46**, 1184 (1924), ISSN 0002-7863, URL http://pubs.acs.org/doi/abs/10.1021/ja01670a011?journalCode=jacsathttp://dx.doi.org/10.1021/ja01670a011.

[115] S. Umino, Sci. Rep. Tohoku Imp. Univ., Ser. 1 **15**, 597 (1926).

[116] H. Moser, Phys. Zeitschrift **37**, 737 (1936), URL http://dispatch.opac.d-nb.de/DB=1.1/CMD?ACT=SRCHA&IKT=8506&TRM=200089-1.

[117] W. Giauque and P. Meads, J. Am. Chem. Soc. **63**, 1897 (1941), ISSN 0002-7863, URL http://pubs.acs.org/doi/abs/10.1021/ja01852a027.

[118] A. H. Seville, Phys. Status Solidi **21**, 649 (1974), ISSN 00318965, URL http://doi.wiley.com/10.1002/pssa.2210210230.

[119] A. Macleod, J. Chem. Thermodyn. **4**, 391 (1972), ISSN 00219614, URL http://www.sciencedirect.com/science/article/pii/0021961472900225.

[120] F. M. Jaeger and E. Rosenbohm, Physica **6**, 1123 (1939), ISSN 00318914, URL http://www.sciencedirect.com/science/article/pii/S0031891439901114.

[121] W. B. Kendall, R. L. Orr, and R. Hultgren, J. Chem. Eng. Data **7**, 516 (1962), URL http://dx.doi.org/10.1021/je60015a022.

[122] G. Cordoba and C. Brooks, Phys. Status Solidi **581** (1971), ISSN 00318965, URL http://onlinelibrary.wiley.com/doi/10.1002/pssa.2210060227/abstract.

[123] R. Kohlhaas and O. Vollmer, Zeitschrift für Met. **59**, 273 (1968), URL http://catalog.hathitrust.org/Record/000533688.

[124] B. Grabowski, S. Wippermann, A. Glensk, T. Hickel, and J. Neugebauer, Phys. Rev. B **91** (2015), ISSN 1098-0121, URL http://link.aps.org/doi/10.1103/PhysRevB.91.201103.

[125] A. Glensk, B. Grabowski, T. Hickel, and J. Neugebauer, *New insights into anharmonicity, Ringberg workshop, Poster presentation* (2012).

[126] W. Xing, P. Liu, X. Cheng, H. Niu, H. Ma, D. Li, Y. Li, and X.-Q. Chen, Phys. Rev. B **90**, 144105 (2014), ISSN 1098-0121, URL http://link.aps.org/doi/10.1103/PhysRevB.90.144105.

[127] J. Harl and G. Kresse, Phys. Rev. Lett. **103**, 056401 (2009), ISSN 0031-9007, URL http://link.aps.org/doi/10.1103/PhysRevLett.103.056401.

[128] D. Lu, Y. Li, D. Rocca, and G. Galli, Phys. Rev. Lett. **102**, 1 (2009), ISSN 00319007, URL http://journals.aps.org/prl/pdf/10.1103/PhysRevLett.102.206411.

[129] L. Schimka, R. Gaudoin, J. Klimeš, M. Marsman, and G. Kresse, Phys. Rev. B - Condens. Matter Mater. Phys. **87**, 1 (2013), ISSN 10980121, URL http://journals.aps.org/prb/abstract/10.1103/PhysRevB.87.214102.

[130] I. Kogut and M. C. Record, Thin Solid Films **522**, 149 (2012), ISSN 00406090, URL http://dx.doi.org/10.1016/j.tsf.2012.08.037.

[131] H. Ihou-Mouko, C. Mercier, J. Tobola, G. Pont, and H. Scherrer, J. Alloys Compd. **509**, 6503 (2011), ISSN 09258388, URL http://dx.doi.org/10.1016/j.jallcom.2011.03.081.

[132] D. Bessas, R. E. Simon, K. Friese, M. Koza, and R. P. Hermann, J. Phys. Condens. Matter **26**, 485401 (2014), ISSN 0953-8984, URL http://stacks.iop.org/0953-8984/26/i=48/a=485401?key=crossref.f5dda283de9a36fbc0d519485120f8ad.

[133] H. Feufel, T. Gödecke, H. L. Lukas, and F. Sommer, J. Alloys Compd. **247**, 31 (1997), ISSN 09258388, URL http://linkinghub.elsevier.com/retrieve/pii/S0925838896026552.

[134] L. V. Gurvich and I. Veyts, *Thermodynamic Properties Of Individual Substances: Elements And compounds*, Thermodynamic Properties of Individual Substances (Taylor & Francis, 1990), ISBN 9780891165330, URL http://books.google.de/books?id=b83PO5B88HMC.

[135] P. Kantor, O. Kisel, and E. Fomichev, Ukr. Fiz. Zhur. **5**, 358 (1960), URL https://books.google.de/books/about/Specific_heat_metallic_elements_and_allo.html?id=LgIpAQAAMAAJ&redir_esc=y.

[136] N. Serebrennikov and P. Gel'd, Dokl. Akad. Nauk SSSR **87**, 1021 (1952), URL https://books.google.de/books/about/Specific_heat_metallic_elements_and_allo.html?id=LgIpAQAAMAAJ&redir_esc=y.

[137] R. Hultgren, P. Desai, D. Hawkins, M. Gleiser, K. Kelly, and D. Wagman, *Selected Values of the Thermodynamic Properties of the Elements* (ASM, Metals Park, OH, 1973), URL http://oai.dtic.mil/oai/oai?verb=getRecord&metadataPrefix=html&identifier=ADD095430.

[138] K. Yamaguchi and K. Itagaki, J. Therm. Anal. Calorim. **69**, 1059 (2002), URL http://www.akademiai.com/index/G26357320765U3R2.pdf.

[139] P. Smith, London, Edinburgh, Dublin Philos. Mag. J. Sci. **46**, 744 (1955), ISSN 1941-5982, URL http://www.tandfonline.com/doi/abs/10.1080/14786440708520601.

[140] W. Mannchen and V.W. Bornkessel, Zeitschrift für Met. **51**, 482 (1960), URL http://catalog.hathitrust.org/Record/000533688.

[141] R. S. Craig, C. A. Krier, L. W. Coffer, E. A. Bates, and W. E. Wallace, J. Am. Chem. Soc. **76**, 238 (1954), ISSN 0002-7863, URL http://pubs.acs.org/doi/abs/10.1021/ja01630a061.

[142] D. R. Stull and R. A. McDonald, J. Am. Chem. Soc. **77**, 5293 (1955), ISSN 0002-7863, URL http://pubs.acs.org/doi/abs/10.1021/ja01625a027.

[143] B. C. Gerstein, J. Chem. Phys. **47**, 2109 (1967), ISSN 00219606, URL http://link.aip.org/link/JCPSA6/v47/i6/p2109/s1http://link.aip.org/link/?JCP/47/2109/1&Agg=doi.

[144] W. Mannchen and G. Jacobi, Z. Naturforsch. **20b**, 178 (1965), URL http://www.znaturforsch.com/ab/v20b/c20b.htm.

[145] J. Leitner, P. Voka, D. Sedmidubský, and P. Svoboda, Thermochim. Acta **497**, 7 (2010), ISSN 00406031, URL http://www.sciencedirect.com/science/article/pii/S0040603109003189.

[146] S. Foiles, Phys. Rev. B **49**, 14930 (1994), ISSN 0163-1829, URL http://link.aps.org/doi/10.1103/PhysRevB.49.14930.

[147] M. J. Gillan, J. Phys. Condens. Matter **1**, 689 (1989), ISSN 0953-8984, URL http://iopscience.iop.org/0953-8984/1/4/005.

[148] H. Polatoglou, M. Methfessel, and M. Scheffler, Phys. Rev. B **48**, 1877 (1993), ISSN 0163-1829, URL http://link.aps.org/doi/10.1103/PhysRevB.48.1877.

[149] M. Puska, S. Pöykkö, M. Pesola, and R. Nieminen, Phys. Rev. B **58**, 1318 (1998), ISSN 0163-1829, URL http://journals.aps.org/prb/abstract/10.1103/PhysRevB.58.1318.

[150] T. Hoshino, R. Zeller, and P. Dederichs, Phys. Rev. B **53**, 8971 (1996), ISSN 0163-1829, URL http://www.ncbi.nlm.nih.gov/pubmed/9982398.

[151] A. Satta, F. Willaime, and S. de Gironcoli, Phys. Rev. B **60**, 7001 (1999), ISSN 0163-1829, URL http://journals.aps.org/prb/abstract/10.1103/PhysRevB.60.7001.

[152] K. Carling, G. Wahnström, T. R. Mattsson, A. E. Mattsson, N. Sandberg, and G. Grimvall, Phys. Rev. Lett. **85**, 3862 (2000), ISSN 0031-9007, URL http://link.aps.org/doi/10.1103/PhysRevLett.85.3862.

[153] G. Lucas and R. Schäublin, Nucl. Instruments Methods Phys. Res. Sect. B Beam Interact. with Mater. Atoms **267**, 3009 (2009), ISSN 0168583X, URL http://linkinghub.elsevier.com/retrieve/pii/S0168583X09007071.

[154] K. Nordlund and R. Averback, *Handbook ofMaterials Modeling* (Springer, Berlin, 2005), URL https://books.google.com.

[155] R. Simmons and R. W. Balluffi, Phys. Rev. **117**, 52 (1960), ISSN 0031-899X, URL http://link.aps.org/doi/10.1103/PhysRev.117.52.

[156] J. E. Kluin and T. Hehenkamp, Phys. Rev. B **44**, 11597 (1991), ISSN 0163-1829, URL http://prb.aps.org/abstract/PRB/v44/i21/p11597_1.

[157] H. E. Schaefer, Phys. Status Solidi **102**, 47 (1987), ISSN 00318965, URL http://onlinelibrary.wiley.com/doi/10.1002/pssa.2211020104/abstract.

[158] B. T. A. McKee, W. Triftshäuser, and A. T. Stewart, Phys. Rev. Lett. **28**, 358 (1972), ISSN 0031-9007, URL http://link.aps.org/doi/10.1103/PhysRevLett.28.358.

[159] W. Triftshäuser and J. D. McGervey, Appl. Phys. **6**, 177 (1975), ISSN 0340-3793, URL http://link.springer.com/10.1007/BF00883748.

[160] M. Fluss, L. C. Smedskjaer, M. Chason, D. G. Legnini, and R. Siegel, Phys. Rev. B **17**, 3444 (1978), ISSN 0163-1829, URL http://link.aps.org/doi/10.1103/PhysRevB.17.3444.

[161] R. Feder and A. S. Nowick, Philos. Mag. **15**, 805 (1967), ISSN 0031-8086, URL http://www.tandfonline.com/doi/full/10.1080/14786436708220928.

[162] G. Bianchi, D. Mallejac, C. Janot, and G. Champier, Comptes Rendus l'Académie des Sci. **263**, 1404 (1966), URL http://gallica.bnf.fr/ark:/12148/bpt6k62368375/f418.image.r=RousselPatrice1964.langES.

[163] B. Guérard, H. Peisl, and R. Zitzmann, Appl. Phys. **3**, 37 (1974), ISSN 0340-3793, URL http://link.springer.com/10.1007/BF00892332.

[164] R. Q. Hood, P. R. C. Kent, and F. a. Reboredo, Phys. Rev. B **85**, 134109 (2012), ISSN 1098-0121, URL http://link.aps.org/doi/10.1103/PhysRevB.85.134109.

[165] R. Simmons and R. W. Balluffi, Phys. Rev. **119**, 600 (1960), ISSN 0031-899X, URL http://link.aps.org/doi/10.1103/PhysRev.119.600.

[166] R. Simmons and R. W. Balluffi, Phys. Rev. **129**, 1533 (1963), ISSN 0031-899X, URL http://link.aps.org/doi/10.1103/PhysRev.129.1533.

[167] D. Beaman, R. W. Balluffi, and R. Simmons, Phys. Rev. **137**, A917 (1965), ISSN 0031-899X, URL http://link.aps.org/doi/10.1103/PhysRev.137.A917.

[168] R. W. Siegel, Annu. Rev. Mater. Sci. **10**, 393 (1980), ISSN 0084-6600, URL http://www.annualreviews.org/doi/abs/10.1146/annurev.ms.10.080180.002141.

[169] Y. Kraftmakher, *Lecture Notes on Equilibrium Point defects and Thermophysical properties of metals* (World Scientific, London, 2000), ISBN 9810241402, URL http://www.worldscientific.com/doi/pdf/10.1142/9789812384843_bmatter.

[170] N. Sandberg and G. Grimvall, Phys. Rev. B **63**, 184109 (2001), ISSN 0163-1829, URL http://link.aps.org/doi/10.1103/PhysRevB.63.184109.

[171] J. E. Kluin, Philos. Mag. A **65**, 1263 (1992), ISSN 0141-8610, URL http://www.tandfonline.com/doi/abs/10.1080/01418619208205604.

[172] L. A. Girifalco, *Statistical physics of materials* (Wiley, New York, 1973), ISBN 0471302309, URL https://books.google.de/books?id=u5N-AAAAIAAJ&q=L.+A.+Girifalco,+Statistical+physics+of+materials&dq=L.+A.+Girifalco,+Statistical+physics+of+materials&hl=en&sa=X&ei=wMVYVZG1McuGywPJO4HYDA&ved=0CCwQ6AEwAg.

[173] R. Scholz and W. Schüle, Phys. Lett. A **64**, 340 (1977), URL http://www.sciencedirect.com/science/article/pii/037596017790384X.

[174] P. Korzhavyi, I. Abrikosov, B. Johansson, A. Ruban, and H. Skriver, Phys. Rev. B **59**, 11693 (1999), ISSN 0163-1829, URL http://journals.aps.org/prb/abstract/10.1103/PhysRevB.59.11693.

[175] K. M. Carling, G. Wahnström, T. R. Mattsson, N. Sandberg, and G. Grimvall, Phys. Rev. B **67**, 054101 (2003), ISSN 0163-1829, URL http://link.aps.org/doi/10.1103/PhysRevB.67.054101.

[176] K. Nordlund and R. S. Averback, Phys. Rev. Lett. **80**, 4201 (1998), ISSN 0031-9007, URL http://link.aps.org/doi/10.1103/PhysRevLett.80.4201.

[177] R. Nazarov, T. Hickel, and J. Neugebauer, Phys. Rev. B **85**, 144118 (2012), ISSN 1098-0121, URL http://link.aps.org/doi/10.1103/PhysRevB.85.144118.

[178] P. Ehrhart, P. Jung, H. Schultz, and H. Ullmaier, *Atomic Defects in Metals*, vol. 25 of *Landolt-Börnstein - Group III Condensed Matter* (Springer-Verlag, Berlin/Heidelberg, 1991), ISBN 3-540-51435-X, URL http://link.springer.com/10.1007/b37800.

[179] T. R. Mattsson and A. E. Mattsson, Phys. Rev. B **66**, 214110 (2002), ISSN 0163-1829, URL http://link.aps.org/doi/10.1103/PhysRevB.66.214110.

[180] S. Kurth, J. P. Perdew, and P. Blaha, Int. J. Quantum Chem. **75**, 889 (1999), ISSN 0020-7608, URL http://doi.wiley.com/10.1002/(SICI)1097-461X(1999)75:4/5<889::AID-QUA54>3.0.CO;2-8.

[181] R. Armiento and A. E. Mattsson, Phys. Rev. B **72**, 085108 (2005), ISSN 1098-0121, URL http://link.aps.org/doi/10.1103/PhysRevB.72.085108.

[182] Z. D. Popovic, J. P. Carbotte, and G. R. Piercy, J. Phys. F Met. Phys. **4**, 351 (2001), ISSN 0305-4608, URL http://iopscience.iop.org/0305-4608/4/3/008.

[183] M. W. Finnis and M. Sachdev, J. Phys. F Met. Phys. **6**, 965 (1976), ISSN 0305-4608, URL http://iopscience.iop.org/0305-4608/6/6/010.

[184] W. Bollmann, Cryst. Res. Technol. **27**, 673 (1992), ISSN 02321300, URL http://onlinelibrary.wiley.com/doi/10.1002/crat.2170270517/abstract.

[185] P. Varotsos, W. Ludwig, and K. Alexopoulos, Phys. Rev. B **18**, 2683 (1978), ISSN 01631829, URL http://journals.aps.org/prb/abstract/10.1103/PhysRevB.18.2683.

[186] M. Omini, Nuovo Cim. D **2**, 1430 (1983), ISSN 03926737, URL http://link.springer.com/article/10.1007/BF02460223.

[187] L. Zhao, R. Najafabadi, and D. J. Srolovitz, Model. Simul. Mater. Sci. Eng. **1**, 539 (1999), ISSN 0965-0393, URL http://iopscience.iop.org/0965-0393/1/4/015/.

[188] R. P. Gupta, P. K. Sharma, and S. Pal, Phys. status solidi **18**, 119 (1966), ISSN 03701972, URL http://doi.wiley.com/10.1002/pssb.19660180113.

[189] R. H. Carr, R. D. McCammon, and G. K. White, Proc. R. Soc. A Math. Phys. Eng. Sci. **280**, 72 (1964), ISSN 1364-5021, URL http://rspa.royalsocietypublishing.org/content/280/1380/72.

List of Publications

1. A. Glensk, B. Grabowski, T. Hickel, and J. Neugebauer, "Understanding Anharmonicity in fcc Materials: From its Origin to ab initio Strategies beyond the Quasiharmonic Approximation", *Phys. Rev. Letters* **114**, 195901 (2015).

2. A. Glensk, B. Grabowski, T. Hickel, and J. Neugebauer, "Breakdown of the Arrhenius Law in Describing Vacancy Formation Energies: The Importance of Local Anharmonicity Revealed by Ab initio Thermodynamics", *Phys. Rev. X* **4**, 011018 (2014).

3. B. Grabowski, S. Wippermann, A. Glensk, T. Hickel, and J. Neugebauer, "Random phase approximation up to the melting point: Impact of anharmonicity and nonlocal many-body effects on the thermodynamics of Au", *Phys. Rev. B — Rapid Communications* **91**, 201103 (2015).

4. A. Duff, T. Davey, D. Korbmacher, A. Glensk, B. Grabowski, J. Neugebauer, M. W. Finnis, "Improved method of calculating ab initio high-temperature thermodynamic properties with application to ZrC", *Phys. Rev. B* **91**, 214311, (2015)

5. J. Rogal, S. Divinski, M. W. Finnis, A. Glensk, J. Neugebauer, J. H. Perepezko, S. Schuwalow, M. Sluiter, B. Sundman, "Perspectives on point defect thermodynamics", *Physica Status Solidi (B)* **251**, 1 (2014)

6. M. Schick, B. Hallstedt, A. Glensk, B. Grabowski, T. Hickel, M. Hampl, J. Gröbner, J. Neugebauer, R. Schmid-Fetzer, "Combined ab initio, experimental, and CALPHAD approach for an improved thermodynamic evaluation of the MgSi system", *Calphad* **37** (2012)